A PIEZOELECTRICALLY ACTUATED CRYOGENIC MICROVALVE WITH INTEGRATED SENSORS

by

Jong Moon Park

A dissertation submitted in partial fulfillment
of the requirements for the degree of
Doctor of Philosophy
(Electrical Engineering)
in The University of Michigan
2009

Doctoral Committee:

Professor Yogesh B. Gianchandani, Chair
Professor Khalil Najafi
Professor Kensall D. Wise
Associate Professor Luis P. Bernal

© Jong Moon Park
All rights reserved
2009

To my parents

ACKNOWLEDGEMENTS

I would like to give my sincere gratitude to my advisor, Professor Yogesh Gianchandani, for giving me the opportunity to work on the exciting project and also for his teaching, guidance, and support. I also thank my committee members, Prof. Wise, Prof. Najafi, and Prof. Bernal for their interest and valuable insights in various aspects of my work.

I also would like to express my thanks to Prof. Klein and Prof. Nellis and their students, Ryan Taylor, Tyler Brosten, Kristian Rasmussen at University of Wisconsin at Madison for their contribution in numerical modeling related to this work.

I am thankful to many former Ph.D. students in my group, Dr. Senol Mutlu, Dr. Kabir Udeshi, Dr. Kenichi Takahata, Dr. Bhaskar Mitra and Dr. Amar Basu, who have helped me to get a good start on my research. I especially thank my colleague, Allan Evans for his efforts in carrying out the project together. I also thank all my friends and colleagues in my group and SSEL for their companionship, support, and encouragement: Weibin, Tao, Mark, Christine, Scott Green, Scott Wright, Naveen, Karthik, Jae Yoong, Tzeno, Andy, Razi, Sang-Hyun, Seow Yuen, Ruba, Jay, SangWon, Hanseup, Sangwoo, Junseok, Bercu, Gayatri, Kyusuk, and many other.

I would like to acknowledge Lurie Nanofabrication Facility (LNF) staff members for keeping the cleanroom safe and enjoyable place to work.

Finally, I thank my parents, sister and my girlfriend, Jenny, for their endless love and support.

This work was supported primarily by NASA under award number NNA05CP85G.

TABLE OF CONTENTS

DEDICATION ii
ACKNOWLEDGEMENTS iii
LIST OF FIGURES vii
LIST OF TABLES xii
ABSTRACT xiii
CHAPTER 1 INTRODUCTION 1
1.1 Distributed Cooling System 3
1.2 Operating Requirements for the Valve 6
1.3 Overview of Microvalves 7
1.3.1 Electromagnetic actuation 8
1.3.2 Electrostatic actuation 9
1.3.3 Piezoelectric actuation 12
1.3.4 Thermal actuation 14
CHAPTER 2 MICROVALVE FOR CRYOGENIC APPLICATIONS 18
2.1 Microvalve Design 18
2.1.1 Selection of valve actuation scheme 18
2.1.2 Device Concepts and Operation 21
2.1.3 PZT characterization 22
2.1.4 Perimeter augmentation 25
2.2 Modeling of the Microvalve 29
2.2.1 Flow through the grooves 30
2.2.2 Flow through the land 31
2.2.3 The microvalve flow model 32
2.3 Device Fabrication 36
2.3.1 SOI Wafer Fabrication 37
2.3.2 Glass Wafer Fabrication 38

2.3.3 Device Assembly 40
2.4 Experimental Results 43
2.4.1 Room Temperature Flow Test 43
2.4.2 Cryogenic Temperature Flow Test 46
2.4.3 High Temperature Flow Test 48
2.4.4 Dynamic Characteristics 50
2.5 Discussion and Conclusions 53
CHAPTER 3 MICROVALVE WITH INTEGRATED SENSORS 55
3.1 Microvalve and Sensor Design 57
3.2 Device Fabrication 59
3.3 Experimental Results 65
3.4 Discussion 69
3.4.1 Flow Measurements 69
3.4.2 Pressure Sensor Measurements 70
3.4.3 RTD Measurements 72
3.4.4 Stress Effects 72
3.5 Conclusions 75
CHAPTER 4 VALVE APPLICATIONS 77
4.1 Liquid Flow Modulation 77
4.1.1 System Overview 78
4.1.2. Microvalve Liquid Flow Tests 79
4.2 Joule-Thomson Cooling System Test 82
4.2.1 Joule-Thomson Effect 82
4.2.2 Microvalve Test 83
4.2.3 MEMS Heat Exchanger 86
4.2.4 Heat exchanger self cooling test 88
4.2.5 Self Cooling Test with Heat Exchanger and Valve 89
CHAPTER 5 CONCLUSION AND FUTURE WORK 91
5.1 Summary of the Work 91
5.2 Recommendations for Future Work 93
REFERENCES 96

LIST OF FIGURES

Figure 1.1: Illustration of the Single Aperture Far-Infrared Observatory (SAFIR) [2] 2

Figure 1.2: Temperature dependence of SAFIR sensitivity. Lower vertical values represent better sensitivity. Low temperature is very important to achieve desired sensitivity. (Figure is adapted from [3].) 2

Figure 1.3: Illustration of a distributed cooling system concept. An array of cooling elements, each consisting of a valve, heat exchanger and a sensor, is placed across the structure to be cooled. 4

Figure 1.4: Proposed application of an actively controlled valve. Microvalves can (a) modulate the flow of coolant in distributed heat exchangers, or (b) be used as expansion valves in Joule-Thomson cryocoolers. 5

Figure 1.5: Two main configurations using piezoelectric actuation: (a) Stacked PZT and (b) thin film PZT. 13

Figure 1.6: Flow rate vs. power consumption for currently reported microvalves using electrostatic, piezoelectric, electromagnetic, bimetallic, shape memory alloy, and thermopneumatic actuations. The target for our valve is to provide flow rates that exceed 1 L/min but still maintain less than 1 mW of power. 17

Figure 2.1: Microvalve concepts: The valve consists of a ceramic-PZT-Si-glass structure. A PZT stack actuator moves the silicon plate to open or close the valve. 22

Figure 2.2: (a) Schematic of the test apparatus for PZT characterization and (b) picture of the assembled test facility... 23

Figure 2.3: Measured effective PZT stack actuation constant as a function of temperature. 24

Figure 2.4: Measured PZT stack coefficient of thermal expansion as a function of temperature. 25

Figure 2.5: Microvalve concepts: The valve cross-section of the ceramic-PZT-Si-glass structure is shown on the far left. Micro groove patterns to increase flow area are depicted in the middle. The recessed glass along with the side view of the Si piece is illustrated on the right.. 28

Figure 2.6: Flow pattern of the valve: Fluid flows from the inlet manifold to the high-pressure grooves, across the land region, the low-pressure grooves, then to the outlet.. 29

Figure 2.7: Top and side view of the land and groove region with assigned symbols.30

Figure 2.8: Groove friction factor as a function of the Reynolds number based on the groove hydraulic diameter. 31

Figure 2.9: Mass balance terms for the control volumes of the numerical solution. .. 33

Figure 2.10: Simulation results showing the effect of perimeter augmentation............ 34

Figure 2.11: Valve flow model prediction: Room temperature nitrogen flow rate at various inlet pressures.. 35

Figure 2.12: Si-glass micromachining process: The buried oxide layer in the SOI wafer acts as an etch stop for DRIE. A three-step DRIE process is illustrated for the SOI wafer. A glass wafer undergoes a wet etch process and a electrochemical discharge machining process for inlet and outlet hole creation. Finally, the Al metal layer is deposited and patterned in preparation for anodic bonding to prevent bonding of the valve seat to the glass substrate. 36

Figure 2.13: SEM photographs of grooves on a valve plate fabricated by DRIE. (a): Valve plate. Part of a flexure is also seen on the left side, (b) and (c): A valve plate is diced to expose the cross-sectional view. 38

Figure 2.14: Schematics of the ECDM setup for machining glass wafers.................... 39

Figure 2.15: SEM photograph of a hole in a Pyrex glass wafer formed by ECDM process: (a) Top view and (b) the cross-sectional view........................... 40

Figure 2.16: Pre-stressed microvalve assembly procedure: (a) First, a PZT stack is attached to the Macor ceramic structure using epoxy. (b) Then a Si-glass die is bonded at the end of the PZT and Macor structure by an epoxy joint. During this procedure, the PZT stack is actuated until the epoxy is fully cured, which results in a normally-open valve (c). 41

Figure 2.17: Completely assembled valve structure. (a) Two valves (front and back) are shown. (b) Another view of the valve with the Macor header and a US penny... 42

Figure 2.18: Schematic of the room temperature flow measurement test apparatus..... 43

Figure 2.19: Flow rates as a function of voltage from experimental results and the analytic model. As the actuation voltage increases, the valve is closed, which results in a decrease in flow rate. 44

Figure 2.20: Schematic of the test setup for the high-pressure room-temperature gas flow measurement. 45

Figure 2.21: Flow rates as a function of actuation voltage measured at room temperature with an inlet pressure of 345 kPaG and an inlet to outlet pressure differential of 34 kPa. Experimental data are shown with the numerical modeling results. Flow rate measurements present the hysteretic behavior of the PZT actuator. 46

Figure 2.22: Schematic of the test setup for cryogenic flow measurement 47

Figure 2.23: (a) Measured flow rates as a function of voltage at liquid nitrogen temperature (80 K) compared with (b) the analytic model. 47

Figure 2.24: Normalized flow rate vs. actuation voltage obtained at cryogenic temperature. 48

Figure 2.25: Measured flow rates as a function of voltage at 110˚C and 26˚C with inlet pressure of 25 kPa. 49

Figure 2.26: Transient response of the valve measured using a laser Doppler vibrometer with a sampling rate of 1.28 MHz. The response time for 0 to 100 V actuation is measured to be 700 μs. Some oscillations are evident due to the mechanical properties of PZT. 51

Figure 2.27: The bandwidth of the valve at room temperature is determined by 100 V square waves applied from 100 Hz to 4.5 kHz in 100 Hz increments. The displacements are measured and normalized to the DC valve. The dots represent data points with error bars. The best fit curve is also plotted. The 3 dB bandwidth occurs at around 820 Hz. 52

Figure 3.1: Microvalve concepts: (a) A valve plate suspended by a Si membrane with integrated sensors viewed from the bottom. The RTD sensor is located on the backside of the wafer and is not visible. (b) A cut away view of an assembled ceramic-PZT-Si-glass valve structure. 58

Figure 3.2: Si-glass micromachining process: sensors are formed on the device layer of the SOI wafer by various surface micromachining techniques. Then DRIE is performed to form membrane and groove patterns. A glass wafer undergoes two wet etch steps for a recess and through-hole formation. Next, the two wafers are anodically bonded and diced. 59

Figure 3.3: (a) Photograph of the top of the SOI wafer showing the metal contact layer with (b) an expanded view of the platinum RTD. (c) Wide and (d) expanded views of the circular serpentine groove patterns for perimeter augmentation from the bottom of the SOI wafer. This side bonds to the glass wafer. 61

Figure 3.4: The assembly process can be slightly modified to result in either normally-closed or normally-open valves. Energizing the PZT actuator during assembly results in a normally-open configuration (top), while no PZT actuation during assembly yields a normally-closed valve (bottom)........ 63

Figure 3.5: An assembled valve looking from the glass side with a US penny. The pressure sensor cavity is connected to the inlet through a passage. The RTD is positioned on the backside of the silicon die............................... 64

Figure 3.6: Flow rates as a function of actuation voltage measured at room temperature. Flow measurements of (a) normally-open valve, and (b) normally-closed valve measured at a differential inlet pressure of 52 kPa. 66

Figure 3.7: Flow characteristic of a normally-open valve at different temperatures. The measurement was made at 34 kPa differential pressure with 160 kPa absolute inlet pressure. As the temperature decreases, actuation of the PZT has a lesser effect on flow modulation, thus resulting in a higher flow rate at a given actuation voltage. This is mainly due to a degraded piezoelectric performance at lower temperatures. Hysteresis of the PZT actuation is represented as error bars here. 67

Figure 3.8: Output voltage from the piezoresistive pressure sensor at various differential pressures and temperature. The linearity of the pressure sensor was still good at low temperatures; however, the offset voltage and sensitivity of the sensor changes with varying temperatures................... 68

Figure 3.9: Measured RTD resistance versus temperature change with best fit lines (a) on bulk silicon, and (b) in a packaged device. The RTD shows bilinear behavior, with a sensitivity of 0.29 %/K above 140k and 0.37 %/K below it. 69

Figure 3.10: The effect of temperature on the piezoresistive pressure sensor. (a) The measured sensitivity of the pressure sensor decreases with increasing temperature with 356 ppm/kPa at room temperature. The sensitivity is plotted in both ppm/kPa and ppm/torr. The behavior is dominated by the temperature dependency of the piezoresistance factor. (b) Measured offset voltage also changes with temperature due to thermally induced stress on the membrane.. 70

Figure 3.11: Comparison of the coefficient of thermal expansion of Pt, Pyrex glass, and silicon... 74

Figure 4.1: Proposed system schematic of the microvalve controlled portable drug delivery system. 79

Figure 4.2: Flow rate through un-actuated valve (0 V) across various pressures. At low pressure the flow rate changes almost linearly with pressure (Allan Evans [99]). 80

Figure 4.3: Flow rate changes as a function of actuation voltage shown at two different inlet pressure values (Allan Evans [99]). 81

Figure 4.4: (a) Temperature-entropy diagram and (b) basic components of a JT cooler equipped with a recuperative heat exchanger. 83

Figure 4.5: Plot of flow rate as a function of actuation voltage while inlet and outlet pressures are held constant. 84

Figure 4.6: The data in Figure 4.5 is re-plotted with expected flow rates through a jewel orifice. The differential pressure is maintained at 229 kPa. 85

Figure 4.7: Flow rates of a microvalve at various differential pressures compared with measured flow rates using 0.015" and 0.010" orifices. 86

Figure 4.8: Schematic of a perforated plate recuperative micro heat exchanger (Weibin Zhu [102]). 87

Figure 4.9: Schematic of the self-cooling test setup of the forty-three die heat exchanger. The test is conducted using ethane as a working fluid. Jewel orifices can be used in place of the microvalve. The pressure differential between the inlet and outlet of the heat exchanger and temperature difference between the inlet of the heat exchanger and outlet of the valve are measured. 88

Figure 4.10: Temperature difference between the heat exchanger inlet streams as a function of pressure difference applied across the forty-three die heat exchanger assembly. The optimal orifice size is 0.015" (Weibin Zhu [103]). 89

Figure 4.11: Temperature difference as a function of pressure difference while the valve is actuated at -30 V and 100 V [103]. 90

LIST OF TABLES

Table 2.1: Piezoelectric coefficients and other relevant properties for a selected list of piezoelectric materials [70]. 19

Table 2.2: Variables used in the simulation. 34

ABSTRACT

A PIEZOELECTRICALLY ACTUATED CRYOGENIC MICROVALVE WITH INTEGRATED SENSORS

by

Jong Moon Park

Chair: Yogesh B. Gianchandani

Future space missions require cooling of large optical structures and cryogenic storage systems. A distributed network of cooling elements can provide location specific temperature control. In particular, multiple cooling elements, each including actively controlled valves, are to be positioned across the structure. This thesis presents piezoelectrically actuated microvalves for modulating refrigerant flow in a cryogenic cooling system.

The first-generation valve consists of a micromachined die fabricated from a silicon-on-insulator wafer and a glass wafer, a commercially available piezoelectric stack actuator, and Macor ceramic encapsulation, having overall dimensions of 1×1×1 cm^3. The silicon valve seat is suspended by a crab-leg flexure formation and attached to the piezoelectric stack actuator, which moves in an out-of-plane motion against the glass substrate. Piezoelectric actuation has many advantages, such as, high force, low power operation, and fast response time, but only provides modest displacement, which poses a

challenge in providing sufficient coolant flow. Thus, a perimeter augmentation scheme for the valve seat has been implemented to increase flow area and consequently provide high flow modulation. The valve can modulate the flow from 980 mL/min with the valve fully open (0 V) to 0 mL/min with 60 V actuation voltage at a pressure difference of 55 kPa at room temperature. The operation of the valve has been validated at temperatures over 80-380 K, and at pressures up to 130 kPa. At an 80 K temperature, flow can be modulated from 344 mL/min to 24 mL/min with a pressure difference of 104 kPa. The valve has a response time of less than 1 msec and has an operation bandwidth up to 820 Hz. It is used in the Joule-Thomson self-cooling test with a micromachined recuperative heat exchanger, and a temperature decrease of as much as 42 K is presented.

For the second-generation design, a similar architecture is implemented with integrated sensors for inlet pressure and temperature. The overall size has been increased to $1.5\times1.5\times1$ cm^3 but implementation of a membrane type suspension substantially decreased the dead volume inside the valve. The assembly process allows the implantation of normally-open, partially-open, and normally-closed valves. At room temperature, a normally-open valve achieved gas flow modulation from 200 mL/min to 0 mL/min with 0 V to 40 V actuation. For a normally-closed valve, gas flow could be modulated from 0 mL/min to 115 mL/min. Sensors are strategically positioned at the upstream end of the valve so that the information can be used for closed-loop control. Sensitivities of 356 ppm/kPa for the piezoresistive pressure sensor and 0.29 %/K for the platinum resistance temperature detector (RTD) are reported. These valves are compatible with liquids, thus the liquid modulation, using the valve for drug delivery application, is briefly discussed.

CHAPTER 1

INTRODUCTION

Future NASA (National Aeronautics and Space Administration) missions require cooling of large optical structures and cryogenic storage systems with a high degree of temperature stability and a small temperature gradient. For example, the SAFIR (Single Aperture Far Infrared Observatory, Figure 1.1) is a 10-meter telescope for observation in the far-infrared spectral region and has potential for an improvement of 3 to 5 orders of magnitude in sensitivity compared to its predecessors, e.g., the Stratospheric Observatory for Infrared Astronomy (SOFIA) and the Herschel Space Observatory [1]. The significance of infrared astronomy is that it can provide information on the formation of the first stars and galaxies in the universe's distant past, as the light emitted from these galaxies is shifted into the infrared part of the spectrum (20 μm to 1 mm) by the time it reaches the telescopes, due to the Doppler effect. A warmer telescope produces its own infrared radiation, which generates noise in the detectors. To yield its optimal sensitivity for spectroscopy, the temperature of the telescope must be less than 5 K, so that the sensitivity is limited only by astrophysical background noise [3]. Figure 1.2 shows the temperature dependence of SAFIR sensitivity. Lower vertical values indicate higher sensitivity. There is no significant gain by cooling the telescope lower than 4 K, due to astrophysical background noise. However, there are two orders of magnitude

improvement in sensitivity by bringing the temperature down from 32 K to 4 K. The thermal design of SAFIR employs various cooling stages to bring the telescope temperature below 4 K. Both the spatial and temporal uniformity of the telescope temperature are important in obtaining the highest sensitivity from the instrument [4].

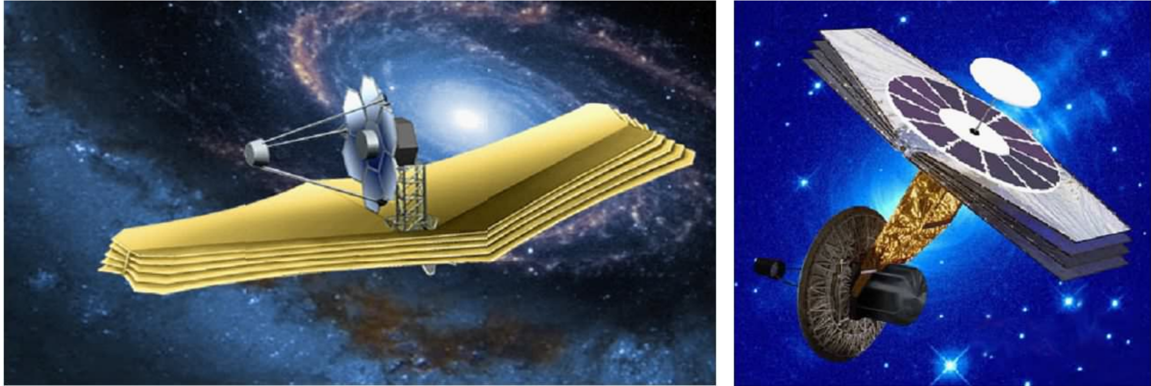

Figure 1.1: Illustration of the Single Aperture Far-Infrared Observatory (SAFIR) [2]

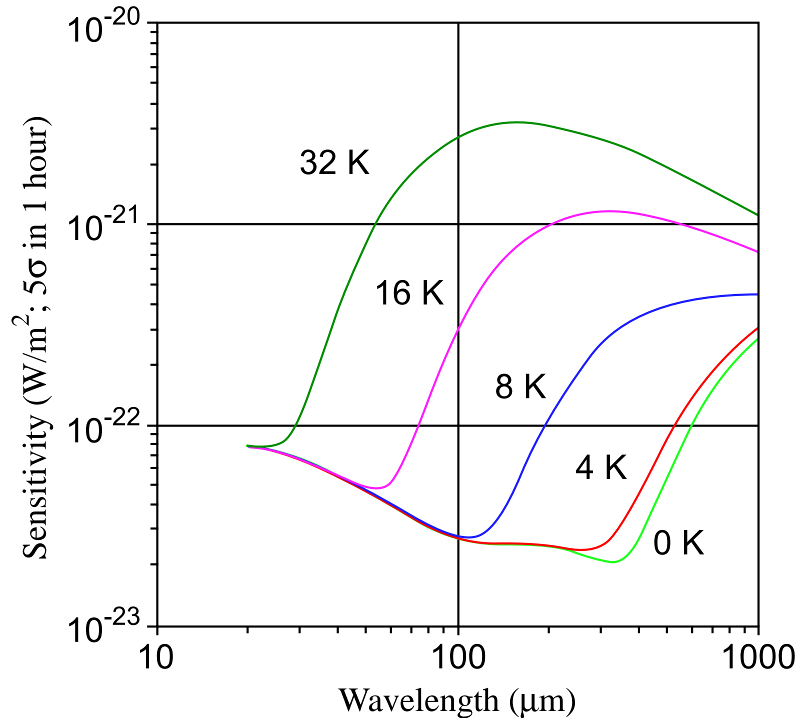

Figure 1.2: Temperature dependence of SAFIR sensitivity. Lower vertical values represent better sensitivity. Low temperature is very important to achieve desired sensitivity. (Figure is adapted from [3].)

Cryogenic storage systems will also require active cooling for fulfilling future long-term space missions. One of the main concerns for a manned trip to Mars is storage of the cryogenic propellants needed for the mission. The projected mission duration is as long as 1700 days, making effective cryogenic fluid management an integral part of the mission [5]. These storage facilities will be much larger than anything that has been previously launched into space. Due to the size of the propellant storage tanks, they are often subjected to large incidental parasitic heat gains on the tank. The current state of the art for cryo-propellant storage involves a loss rate of 3 %/month using passive technology such as multilayer insulation and vapor cooled shielding [6]. By using cryocoolers to actively cool the internally generated heat loads in the cryo-tank, long-term storage of cryogenic propellants for space missions can be realized [7]. This will eliminate larger tanks and extra propellant, reducing the weight and the launch cost.

1.1 Distributed Cooling System

It is quite challenging to provide the strict thermal stability to these large structures with a single cryocooler. Currently, the cooling is often provided by adiabatic demagnetization refrigerators [8], Joule-Thomson coolers [9], pulse tube refrigerators [10], Stirling coolers [11], or staging multiple coolers. All these systems possess various benefits such as low mass, high efficiency, minimal vibration, or low electromagnetic interferences. However, these technologies are best suited for point cooling, and delivering the cooling load to large structures in remote distances is yet to be solved. An attractive solution is an implementation of a distributed network of cooling elements to provide appropriate cooling for the systems. More specifically, multiple cooling

elements, each of which consists of actively controlled valves integrated with heat exchangers and temperature sensors, are positioned across the structure to be cooled as schematically shown in Figure 1.3. The actively controlled valves are capable of regulating the flow in response to local temperature.

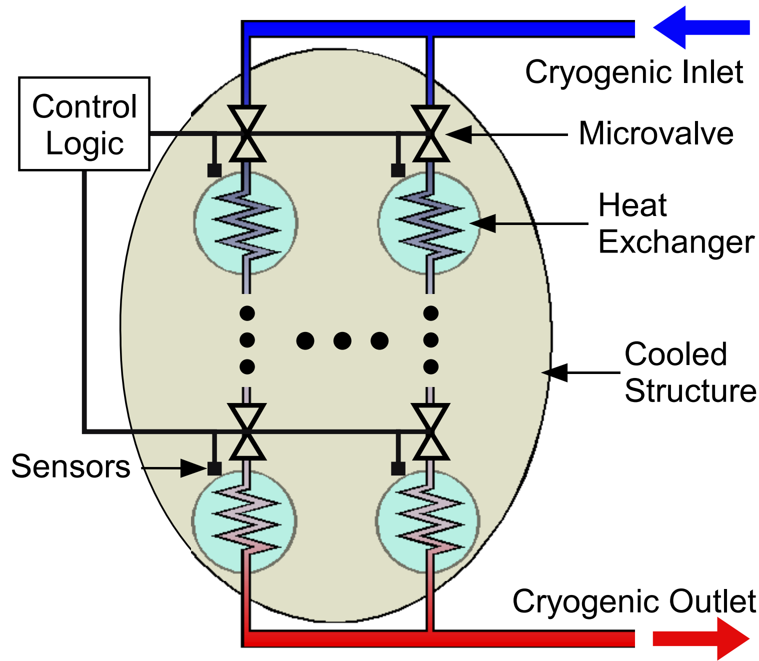

Figure 1.3: Illustration of a distributed cooling system concept. An array of cooling elements, each consisting of a valve, heat exchanger and a sensor, is placed across the structure to be cooled.

With each cooling element working independently in response to local sensors, temperature can be controlled efficiently. Figure 1.4 illustrates two ways by which each cooling element can be realized: (a) a flow of cryogenic fluid at the load temperature through exchangers positioned across the structure to be cooled, or (b) a flow of cryogenic fluid at a higher temperature and pressure through a recuperative heat exchanger, taking advantage of Joule-Thomson refrigeration. Either way, having valves that work reliably at cryogenic temperatures, with large flow modulation capability, is essential. This thesis proposes design, fabrication, and testing of piezoelectric valves

fabricated from Si, glass, and ceramic, to provide the desired thermal stability for space applications.

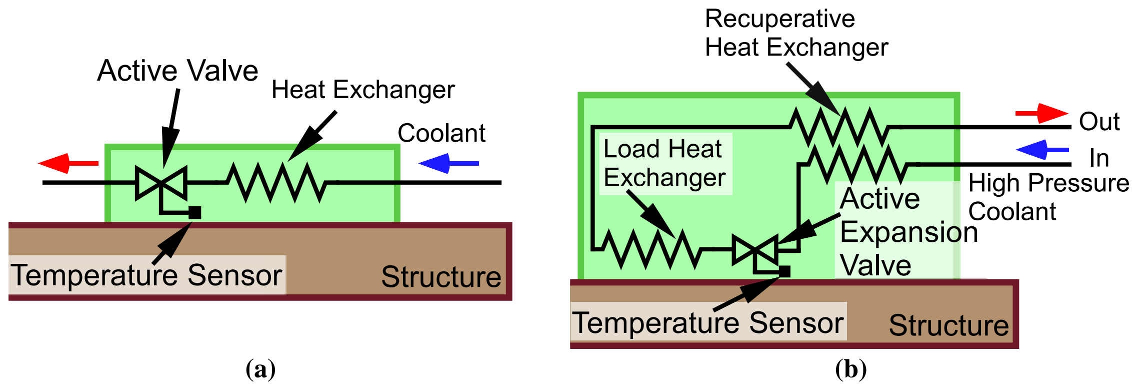

(a) (b)

Figure 1.4: Proposed application of an actively controlled valve. Microvalves can (a) modulate the flow of coolant in distributed heat exchangers, or (b) be used as expansion valves in Joule-Thomson cryocoolers.

In the following subsections of this chapter, the operating requirements for the valve are discussed. Next, a survey on current technologies of micromachined valves is conducted. Chapter 2 describes the development of a microvalve for the proposed applications. This includes a study on the piezoelectric actuator at low temperatures, modeling and design of the microvalve, and flow testing results. In Chapter 3, a microvalve with integrated pressure and temperature sensors for added functionality is presented. The developed valves are used in a cooling system in conjunction with a heat exchanger to control the flow of coolant, and are employed in a drug delivery system to control the delivery rate of a liquid drug. The experiments and results are described in Chapter 4, while the conclusion and future work are presented in Chapter 5.

1.2 Operating Requirements for the Valve

Each cooling element in a distributed cooling system relies on an actively controlled valve. These valves must meet stringent technical requirements. A small form factor is preferable to provide distributed cooling over a large area without significantly affecting the total size and mass of the system. MEMS technology can provide accuracy on small scales with the added benefit of batch production capability. Due to the intended operation in a space environment as a part of the cryogenic cooling system, the active microvalve must have a wide range of operating temperatures, remaining functional at cryogenic temperatures. In addition, the valve must provide a high degree of flow modulation. At the open state, as much as 1000 sccm or more refrigerant should flow through the valve to provide adequate cooling, while the flow is essentially shut off when the valve is closed. However, contrary to a normal valve design, in this design a certain amount of leakage may be acceptable. In other words, providing excess cooling is tolerable. In a similar manner, a normally open valve is desirable because the open condition is a safe failure mode, so that flow of the refrigerant is not blocked. The valve must withstand a large pressure difference to accomplish the free expansion in a Joule-Thomson cooling cycle. Minimal power consumption of the valve is also important to carry out a long-term space mission.

1.3 Overview of Microvalves

The field of microelectromechanical systems has been growing fast in many realms. Furthermore, microvalves are one of the widely used MEMS applications, and aid in meeting challenging requirements of reducing overall size, dead volume, and system cost while improving performance and reliability. In recent decades, a large number of microvalves have been developed for fluid control in a variety of microfluidic applications, such as biomedical drug delivery [12], fuel cell systems [13], micro total analysis systems [14], and space applications [15].

Most microvalves fall into one of two categories: passive microvalves and active microvalves. A passive microvalve is often a check valve that allows fluid flow in a forward direction while preventing the flow in the reverse direction [16-18]. These passive valves are often used in micro-pump applications [19] and route fluid flow in the desired direction, but lack the ability to precisely control flow rate. Active microvalves are composed of a flow channel, a membrane or flexure, and an actuator; there are no actuator components in passive microvalves. This section focuses on literature pertaining to actively controlled microvalves for gas flow control, which is the objective of this research.

For convenience, the valves are categorized by their actuation principles. Various actuation methods have been explored for use in active microvalves: electromagnetic, electrostatic, piezoelectric, and thermal actuation. These will be discussed in more detail in the following subsections.

1.3.1 Electromagnetic actuation

Electromagnetic actuation utilizes the force generated between interaction of current-carrying conductors and a magnetic field. The magnetic field is often applied by a permanent magnet or an external coil. According to the Lorentz force law, the electromagnetic force acting on a test charge is represented as:

$$\vec{F} = q\vec{v} \times \vec{B} \tag{1.1}$$

where q is the electrical charge of the particle, v is the velocity of the particle, and B is the magnetic field. The main advantage of magnetic actuation is the ability to create a relatively large force and thus large deflections with low driving voltages. However, this force does not scale favorably in the micro-domain. For a current-carrying wire in a magnetic field, the magnitude of the force can be rewritten as:

$$F = I \times B \times L = J \times A \times B \times L \tag{1.2}$$

where I is the current, L is the wire length, J is the current density, and A is the cross-sectional area of the wire. Assuming the current density is constant, for characteristic dimension D, the electromagnetic force $F \propto \left[D^3\right]$, which limits its scalability in the micro-domain. However, in millimeter range, electromagnetic actuation can achieve a force of more than 100 times, compared to achievable force employing electrostatic actuation [20].

One of the first active micromachined valves was reported by Terry et al. in 1979, to be used in an integrated gas chromatography system [21]. The valve consists of an etched silicon orifice, a nickel diaphragm, and a solenoid actuator and plunger assembly. When the solenoid is energized, the plunger is pulled, allowing the diaphragm to relax and gas to flow. Other examples of earlier works in magnetically actuated microvalves

are described in references [20,22-25]. These valves utilize external magnetic fields provided by external coils or permanent magnets to actuate a flow blocker made of magnetic material. More recent work involves fully integrated electromagnetic actuation without the aid of any other external components [26-28]. A ball-type microvalve using an iron ball driven by an external solenoid has been reported by Fu et al. [29]. Bae et al. developed a pressure-regulating microvalve as an implant against glaucoma [30]. Gate valves, which are characterized by an in-plane gate motion, with respect to the orifice plane, are also developed with electromagnetic actuation [31]. The rotary gate, fabricated from Permalloy on top of silicon, is rotated by an external electromagnetic actuator, obtaining an open flow rate capacity of up to 500 sccm at 41 kPaG. The magnetic actuation typically generates forces in the range of 1-100 mN with a supply of 100-600 mA of DC current. A flow rate as large as 8.8 l/min has been successfully modulated with this actuation scheme with a valve stroke of 0.1 mm [22]; however, high power consumption (≈ up to 6 W [29]) is a main drawback of magnetically driven valves. Magnetic actuations demonstrate moderate response time ranging from 3 ms [22] to 10 ms [26,27,29,31].

1.3.2 Electrostatic actuation

Electrostatic actuation has been heavily used in Microsystems due to their ease of design and fabrication. The electrostatic force generated between two conductors depends on the separation distance (d) and the applied voltage (V):

$$F = \frac{\partial E}{\partial d} = -\frac{1}{2}\frac{\varepsilon A}{d^2}V^2 \tag{1.3}$$

where ε is the electric permittivity, and A is the overlap area of the two parallel plates. Assuming the actuation voltage stays constant, the electrostatic force $F \propto \left[D^0\right]$. This indicates the force is independent of the characteristic length, D, and would become a dominant force in micro-domain. However, unless the separation distance is very small, the force is generally small. In general, electrostatic actuation is adequate for the low force and energy density requirements and has been used successfully in many MEMS applications. Nonetheless, in some cases, this small displacement may hinder the microvalve performance by limiting flow rate, and to obtain significant forces, large form factors maybe required. Ohnstein et al. have demonstrated an electrostatically actuated microvalve with a cantilever closure plate [32]. The closure plate is made of silicon nitride and embedded with a metal electrode utilizing surface micromachining. The valve provides up to a 150 sccm flow rate with a 30 V drive. An electrostatically actuated microvalve with an S-shaped film has been demonstrated by Shikida et al. [33,34]. The conductive film between a pair of planar electrodes is elastically bent in an S-shape and the S-bend moves back and forth, as the voltage is applied. This particular type of valve demonstrates a large vertical displacement because electrostatic force works effectively at the edge of the S-bend. A flow rate of several sccm can be obtained under a pressure difference of 100 Pa, with actuation voltage of 150 V. A pressure-balanced microvalve has been developed by Huff et al. [35,36] to overcome the limited force generated by the electrostatic method and control fluids at much higher pressure. The valve was tested up to 550 kPa differential pressure across the valve with applied voltage of 210 V. A polymer microvalve with a flexible membrane is presented by Goll et al. [37]. A voltage of 60-150 V was needed to modulate the membrane, and flow rates of 12

mL/min at a differential pressure of 110 kPa has been measured. Wijngaart et al. combined the pressure balancing concept and flexible membrane to demonstrate a large stroke electrostatic microvalve for high pressure control [38]. Their simulation showed that it is possible to control 500 kPa air pressure, while ensuring a 15 μm gas flow gap at 366 V actuation. The large actuation voltage is typical of electrostatic actuation. A Ta-Si-N membrane was used to achieve fast switching valves by Dubois et al. [39,40]. Such valves were developed to be used at differential pressures greater than 200 kPa, and pulse width modulation actuation was used to control the flow rate up to 30 mL/min with actuation voltage of 30 V. In this case, the actuation voltage is substantially lower than the previous case, because the gas flow gap is only 1.5 μm. A bulk-micromachined integrable electrostatic microvalve with a curved-compliant structure was developed for a tactile display system [41,42]. A unique curved-compliant structure was used to lower the voltage required for actuation and the valve needed a relatively low closing voltage of 72.9 V-rms for 19.3 kPa pressure and 86 mL/min flow rate. A group from MIT demonstrated an electrostatic microvalve for gas fuel delivery of their microengine [43]. The valve was fabricated using direct bonding of three wafers and deep reactive ion etch techniques. A 136 V actuation was required to open the valve against a 0.9 MPa pressure difference and a flow rate of 45 sccm was measured when opened. An electrostatic microvalve usually demonstrates an on/off behavior due to its pull-in characteristics. For precise flow control, an array of valves, working in binary mode, is necessary. Robertson et al. integrated an array of electrostatic microvalves with a micromachined 3 μm thick silicon beam to build a gas modulator [44,45]. The flow modulator was specifically designed for low flow rate and was able to control sub-sccm gas flows in the range of

3.8×10^{-3} sccm to 0.7 sccm. Collier et al. also developed a flow control system using 61-microvalve arrays [46]. However, this time a pulse width modulation (PWM) technique was used to take advantage of the characteristically fast response times of electrostatic valves. In particular, a switching time of less than 50 μs has been reported [47]. Generally, a high voltage is necessary to drive the electrostatic actuation, however, when high force is not required, the actuation method provides the advantages of low power consumption and very fast response.

1.3.3 Piezoelectric actuation

Certain crystals have the ability to produce a mechanical deformation by a change in the electrical polarization of the crystal. This is called piezoelectricity. This effect has been widely used in microvalve and micropump fabrication, because it can generate large force (several MPa). The piezoelectric actuation has an added advantage in power consumption because it draws current only during the transition period. Two main uses of a piezoelectric actuator in microvalve applications are reported in the literature: one is taking advantage of the displacement parallel to the polarization (d_{33}), while the other is utilizing the strain orthogonal to the polarization orientation (d_{31}). Laminated PZT stack actuators are examples of the former application, while PZT films in uni-morph and bi-morph configurations are examples of the latter. Figure 1.5 illustrates these two uses of the piezoelectric actuator. The key advantage to using a bi-morph actuator is that larger out-of-plane displacement can be obtained, up to hundreds or thousands of microns, with relatively lower actuation voltage than the stack type PZT. However, as the displacement increases, achievable force is compromised.

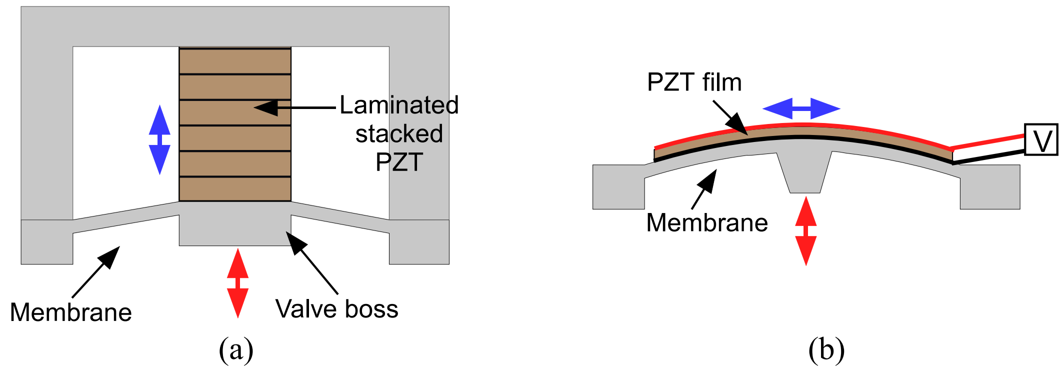

Figure 1.5: Two main configurations using piezoelectric actuation: (a) Stacked PZT and (b) thin film PZT.

One of the earliest works on fabrication of piezoelectric microvalves was presented by Esashi et al. [48-50]. The valve is constructed from silicon mesa suspended with a flexible silicon diaphragm pressing against a glass plate by a stack piezo actuator with dimensions of $3 \times 1.4 \times 9$ mm^3. The valve is capable of modulating a gas flow from 0.1 to 85 mL/min with 73.5 kPa inlet pressure in less than 2 ms response time. A major disadvantage of piezoelectric actuation is its small stroke, even with large voltages. This drawback can be overcome by hydraulic amplification of the piezoelectric actuator [51,52]. A compact high-frequency, high-differential-pressure microvalve developed by Roberts et al. utilizes the hydraulic amplification mechanism to achieve 40-fold amplification of the limited stroke provided by the piezoelectric material. The valve has a nine-layer structure composed of glass, silicon, and silicon on insulator (SOI) layers assembled by wafer-level fusion bonding and anodic bonding, as well as die-level anodic bonding and eutectic bonding. Valve strokes as large as 20 µm were realized and a flow rate of 12.6 mL/min was obtained at 1 kHz. Another microvalve with a 25-fold hydraulic amplification was reported using silicone as a transmission media and a piezo ceramic disc actuator configured as shown in Figure 1.5b [53,54]. The valve stroke of 50 µm and gas flow rate of up to 600 sccm at 200 kPa are achieved. NASA's Jet Propulsion

Laboratory has developed piezoelectric microvalves for space applications [15,55-57]. A series of concentric rings is defined around the orifice to create a leak-tight seal. An extremely low leak rate of 5×10^{-3} mL/min at an inlet pressure of 5.5 MPa was demonstrated. At an inlet pressure of 2 MPa, flow rates of 52 mL/min were measured. A valve made of a surface macromachined piezodisk actuator was described by Watanabe et al. [58]. The valve is constructed of a thin beam with a round valve cap at the center and a valve seat of piezoelectric thin film. For this valve, the actuation occurs in an in-plane direction; when voltage is applied, the disk shaped piezoelectric film shrinks in a horizontal direction, the inner edge moves away from the center and opens up the gas flow path. Each valve, smaller than 1×1 mm^2, can handle up to 2.4 mL/min of flow. Piezoelectric actuation generates a high force, allowing the valve to operate in high pressure environments, providing low power consumption, and fast response (1−2 ms), but the marginal displacement can be a limiting factor.

1.3.4 Thermal actuation

Bimetallic, thermopneumatic, and shape memory alloy actuations use thermal properties of materials to generate displacements. These actuation schemes generally produce a considerable amount of force while simultaneously achieving large strokes. In bimetallically actuated valves, thin-film heater elements are placed on a diaphragm. When they are heated, a difference in the thermal expansion coefficient bends the diaphragm. Bimetallic actuators are often easy to fabricate but draw relatively large amounts of power and are sensitive to ambient temperatures. Jerman showed Al/Si bimetallic driven diaphragms in a valve structure and demonstrated a flow up to 100 mL/min of flow rate at 400 mW of power [59]. Barth et al. developed a Ni-Si bimetallic

microvalve, which successfully opened against 1300 kPa of pressure and achieved a 600 mL/min flow rate with power consumption of 1 W in 200 ms [60]. Messner et al. demonstrated a bimetallically actuated 3-way microvalve, which successfully achieved flow rates up to 800 mL/min at 600 kPa with about 1 W power consumption [61].

Shape memory effect is due to a crystalline transformation between a high-temperature phase and a low-temperature phase. It is an attractive actuation mechanism because it allows simple and compact structures to output high forces, which are capable of use in high-pressure applications. Further advantages of shape memory alloys (SMAs) are a low voltage operation, high reliability, no additional moving parts, and high chemical resistance. Kohl et al. demonstrated gas microvalves using Ti-Ni SMA thin films [62-65]. Maximum gas flow of 1.6 l/min and work output of 35 μNm are achieved with a driving power of 210 mW at a pressure difference of 120 kPa. The response time for closing the valves varies between 0.5 and 1.2 s, and for opening, between 1 and 2 s, depending on the applied pressure difference.

Thermopneumatic microvalves are operated by volumetric thermal expansion or phase-change phenomena coupled to membrane deflection. The actuation method can provide relatively large deflection. However, this type of valve typically has a longer response time and the fabrication process is often complicated due to the necessity to fill the chamber with fluid and to provide a hermetic seal. Zdeblick et al. demonstrated the idea of heating an encapsulated liquid with a miniature resistive heater in order to move a diaphragm [66]. Takao et al. employed PDMS as a diaphragm material for a long stroke actuation in microvalve operation and high sealing performance [67]. At 50 kPa inlet pressure, a microheater power of 100 mW was required to cut-off the flow, and a flow

rate of 17 mL/min was achieved when fully open. The transient time necessary to open the valve was about 23 s and the transient time necessary to close the valve was 1.5 s. Rich et al. also developed a high-flow thermopneumatic microvalve, which is constructed from a three-wafer stack with a corrugated diaphragm [68]. Flow rates as high as 400 mL/min were achieved at 200 kPa differential pressure. 500 mW input power raised the cavity pressure by 260 kPa. Potkay et al. used the combination of a thermopneumatic drive with an electrostatic hold so that the valve only requires power during transition from open to closed and consumes no static power [69]. The thermopneumatic actuator closed the valve in 1 sec at 200 mW input power and the open flow was 3.3 mL/min at 17 kPa. In general, thermal actuation schemes can provide large force to withstand large pressure but as they require current for heating elements, these methods have relatively high power consumption, and generally have slow response time.

Among many requirements for the valve to be used in a distributed cooling system, ability to provide adequate flow rate with low power consumption is a main challenge. Figure 1.6 below, illustrates flow rate versus power characteristics on reported micromachined valves for gas flow control. Power consumption levels for electrostatic actuation are regarded very low, and specific values are often not shown in the literature. Thus, it is assumed to be less than 1 mW in the figure. Only one citation reported the power consumption for piezoelectric actuation, mainly because the consumption is usually low enough not to cause any concern [56]. The trend shows that electrostatic and piezoelectric actuation mechanism consumes much less power than other actuation methods. However, the reported electrostatic and piezoelectric microvalves fail to

provide an adequate flow rate for our application, while other actuation methods consume too much power.

The goal of this research is to develop a microvalve that meets the requirement of cryogenic cooling applications for space missions. In other words, the goal is to construct a microvalve, which provides high flow rates (in the order of hundreds of mL/min), but still maintains low power consumption, preferably less than 1 mW. In addition to meeting flow rate and power consumption requirements, the valve also needs to work reliably in a low temperature and high pressure environment.

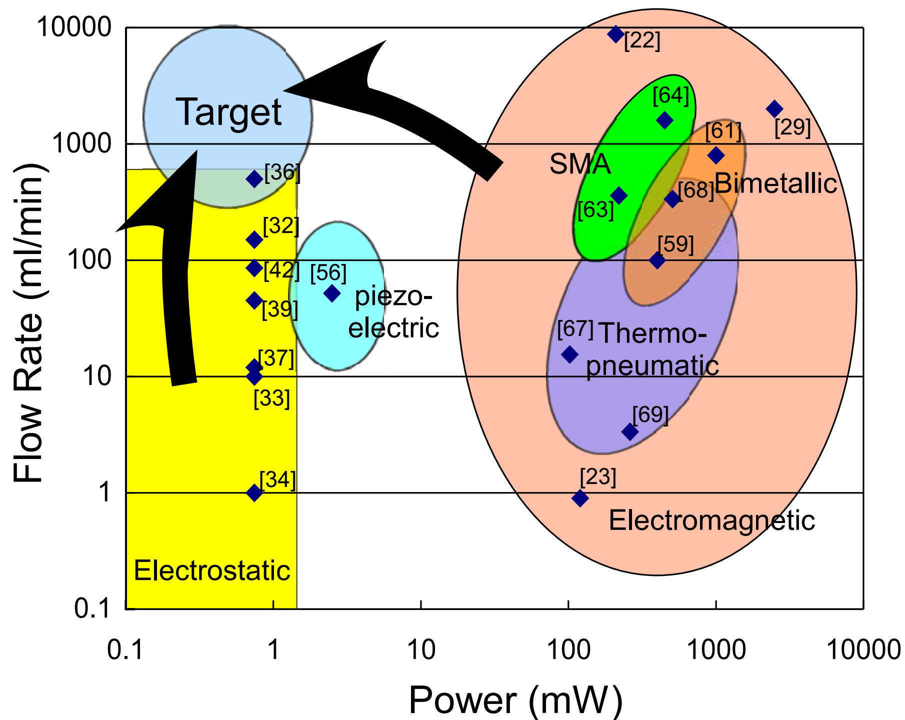

Figure 1.6: Flow rate vs. power consumption for currently reported microvalves using electrostatic, piezoelectric, electromagnetic, bimetallic, shape memory alloy, and thermopneumatic actuations. The target for our valve is to provide flow rates that exceed 1 L/min but still maintain less than 1 mW of power.

CHAPTER 2

MICROVALVE FOR CRYOGENIC APPLICATIONS

As briefly introduced in Chapter 1, each actuation scheme has its own advantages and disadvantages. This chapter will discuss the design target of the proposed microvalve, selection process in the actuation method, baseline characterization necessary in the course of research, how to overcome certain obstacles, and modeling. Finally, we demonstrate the fabricated valve and its behavior at room temperature and at cryogenic temperatures.

2.1 Microvalve Design

2.1.1 Selection of valve actuation scheme

An out-of-plane piezoelectric actuation scheme is chosen after evaluating various actuation schemes. Difficulty in fabrication of coils and/or incorporation of a permanent magnet to the valve, in addition to high power consumption associated with this scheme, eliminated the electromagnetic actuation method. Both electrostatic and piezoelectric actuations are advantageous, having very little power consumption in steady-state operation, but piezoelectric actuation can provide larger force. The large force capability is desirable as it should stand against high inlet pressure and make the valve more robust to friction and contamination. Additionally, electrostatic actuation provides only binary operation of each valve so high flow rates can only be achieved with an increased number

of microvalves. Thermopneumatic valves can generate large actuation forces, but along with other forms of thermal actuations like shape memory alloy and bimetal actuation, its power consumption is high, and performance may very widely with ambient temperature. In addition, nearby heater fabrication can introduce unwanted parasitic heat gain to the cooling system. An electromagnetically driven microvalve can be designed to provide large force and stroke but this method also requires relatively large power. Thus, piezoelectric actuation seemed to be the best candidate for our application.

Material	Piezoelectric Constant (10^{-12}m/V)	Relative Permittivity (ε)	Density (g/cm3)	Young's Modulus (GPa)
Quartz	d_{33} = 2.31	4.5	2.65	107
PVDF	d_{31} = 23 d_{33} = -33	12	1.78	3
LiNbO3	d_{31} = -4 d_{33} = 23	28	4.6	245
BaTiO3	d_{31} = 78 d_{33} = 190	1700	5.7	67
PZT	d_{31} = -171 d_{33} = 370	1700	7.7	53
ZnO	d_{31} = 5.2 d_{33} = 246	1400	5.7	123

Table 2.1: Piezoelectric coefficients and other relevant properties for a selected list of piezoelectric materials [70].

Table 2.1 shows a selected list of piezoelectric materials. Quartz is a naturally occurring piezoelectric material and there are other well-known piezoceramics such as $LiNbO_3$ (lithium niobate), $BaTiO_3$ (barium titanate), PZT, and ZnO (zinc oxide). In addition, PVDF (poly-vinyli-dene-fluoride) is a polymer demonstrating piezoelectric characteristics. The piezoelectric constant denotes strain developed per unit of electric field strength applied. Usually, 3 is designated for polarization axes, so d_{33} represents the strain in the same direction of electric field, while d_{31} represents the strain orthogonal to the electric field. Among these materials, PZT has gained particular interest among the MEMS community due to its high piezoelectric constant and its excellent dielectric and

ferroelectric properties. Thus, we chose PZT as the actuator material and readily available laminated PZT stacks from a commercial vendor (Physik Instrument, http://www.physikinstrumente.com), proved to be another advantage. Finally, the performance of PZT, although degraded, is still appreciable at cryogenic temperatures [71,72].

Many microvalves are developed utilizing out-of-plane configurations. In this configuration, a microvalve typically consists of three major components: inlet and outlet orifices for fluidic flow, a membrane or cantilever beam to open or close the orifice, and an actuator to provide actuation force. Out-of-plane, stacked PZT actuation has been used widely in valves [15,48,49,55]. As each valve is constructed for different applications, the performance goals are different. In a micropropulsion application, it was critical to keep the leak rate low even under high inlet pressure [15,55]. The goal was achieved by fabricating multiple narrow seat rings on a valve seat plate. Shoji et al. used a polymer membrane and a piezoactuator to create a microvalve with small dead volume [48].

In our application, a normally open valve is desirable because the open condition is a safe failure mode, so that flow of the refrigerant is not blocked. For the same reason, an extremely tight seal is not essential. Instead, having valves working reliably at cryogenic temperatures, able to withstand several atmospheres of inlet pressure, and able to provide large flow modulation (0-1000 mL/min) with low power consumption is required. Therefore, a stack type PZT actuator, capable of generating high force with low power consumption is chosen for the application. However, PZT has its own drawback. In general, piezoelectrics have a strain limit on the order of 0.1 – 0.2 %. Even a

laminated PZT actuator of a few millimeters long can produce only a few microns of displacement. Providing sufficient flow rate with such small displacement poses a great challenge and how this is resolvable will be discussed in more detail in the following sections.

2.1.2 Device Concepts and Operation

The general approach utilized to operate this valve is to push a bulk Si micromachined plate against a glass substrate containing inlet and outlet holes, with a piezoelectric actuator. The piezoelectric effect produces an electric field upon mechanical stress on a material, and conversely, an applied electric field induces a strain. Commercially available PZT (lead zirconate titanate) actuators (PL055 from Physik Instrumente) are used as transduction material; the electric field across the PZT expands the actuator and pushes the Si plate against a glass substrate to operate the valve. A single actuator has a footprint of 5×5 mm^2, 2 mm thick. Three of these are stacked to provide larger displacement. The piezoelectric actuation provides enough force to displace the Si against inlet pressure that can exceed 1 atm in some cases. Macor® (machinable glass ceramic) is chosen for the encapsulation material because of its low thermal expansion at low temperature. In addition, it is machinable, capable of holding tight tolerances, and exhibits no outgassing and zero porosity.

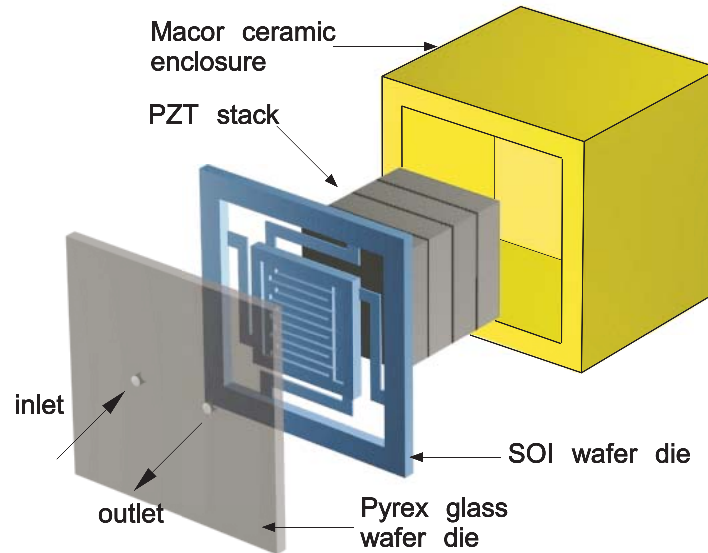

Figure 2.1: Microvalve concepts: The valve consists of a ceramic-PZT-Si-glass structure. A PZT stack actuator moves the silicon plate to open or close the valve.

2.1.3 PZT characterization

To design a valve that works reliably at cryogenic temperatures, knowing the actuator constant of the PZT stack at the temperatures is necessary. It has been reported that the piezoelectric coefficient of PZT is reduced at cryogenic temperatures because the process of domain wall movement in the PZT becomes more difficult as the temperature is lowered, essentially resulting in a stiffer material [73]. Some data have been published by NASA, relative to the properties of various PZT crystals in the 123 K to 523 K [74]. Furthermore, the various manufacturers of PZT stacks, such as Physik Instrumente, Morgan Electro Ceramics, and American Piezo, are able to provide only a very limited amount of information relative to the properties of their materials at very low temperatures. This information is critical to design of the microvalve, so a set of tests was performed to precisely measure the material properties of PZT at cryogenic temperatures.

A special test apparatus was built so that the experiment could be carried out in a vacuum chamber. An actively cooled radiation shield and additional multiple layer insulations were used to minimize the radiation heat leak. A Cryomech AL60 GM cryocooler was used to cool the sample down to 40 K, and then the test platform was allowed to warm up in a controlled manner utilizing an installed heater. During the warm-up, the PZT actuator displacement measurements were taken at various temperatures using two fiber-optic probes. The test apparatus is illustrated in Figure 2.2.

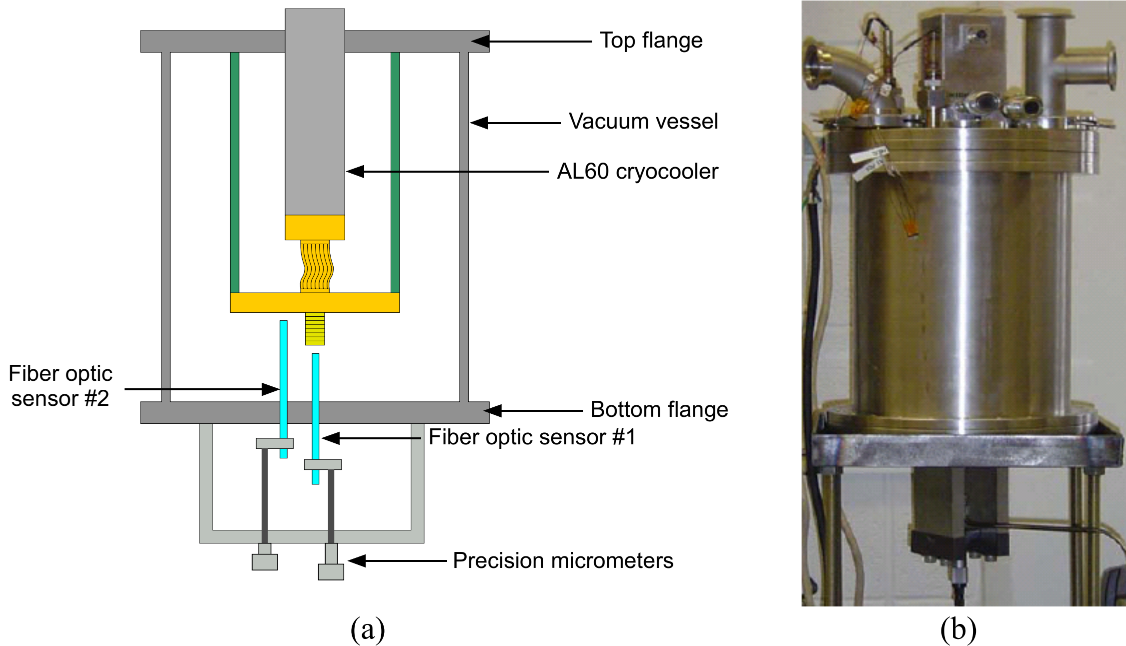

Figure 2.2: (a) Schematic of the test apparatus for PZT characterization and (b) picture of the assembled test facility.

For convenience, an actuator constant (K_c)for this particular PZT is defined as strain per unit voltage,

$$K_c = \frac{\Delta L / L}{V} \tag{2.1}$$

This actuator constant at various temperatures is presented in Figure 2.3. The data is separated into two categories related to the increasing and decreasing voltage portions of

the curve. The data was taken over an applied voltage range of 40-60 V with a nominal median value of 50 V. The actual piezoelectric coefficient (d_{33}) can be obtained from these values, by multiplying the thickness of each PZT layer (t) in the actuator as shown in Eq. 2.2.

$$d_{33} = \frac{\Delta L / L}{V / t} = K_c \cdot t \tag{2.2}$$

The vendor, Physik Instrumente, advertizes that each layer is approximately 50 μm thick. In that case, d_{33} of this PZT actuator at room temperature is,

$$d_{33,room} = K_{c,room} \cdot t = 10.3 \times 10^{-6} \cdot 50 \times 10^{-6} = 515 \times 10^{-12} \ m/V \tag{2.3}$$

Note that, in Figure 2.3, the constant gradually reduces as the temperature decreases; at 40 K, it is approximately one third of the room temperature value.

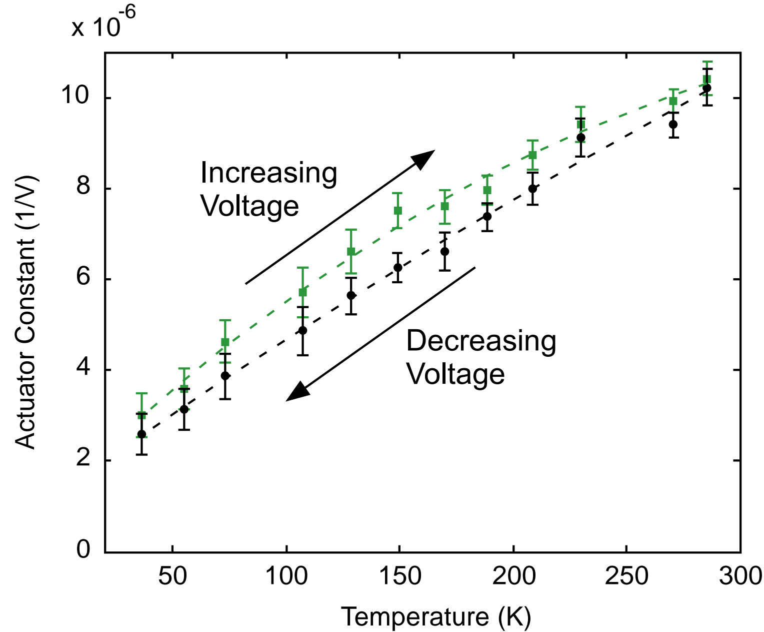

Figure 2.3: Measured effective PZT stack actuation constant as a function of temperature.

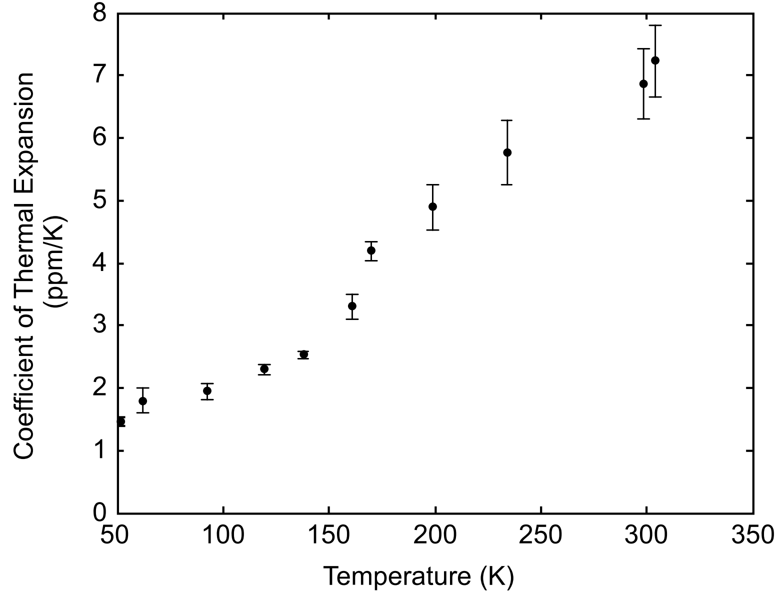

Figure 2.4: Measured PZT stack coefficient of thermal expansion as a function of temperature.

The thermal expansion coefficient (strain per unit temperature) of PZT is also measured and the results are presented in Figure 2.4. The measurements were taken with the leads of the stack shorted in order to prevent any self-energizing effects. Notice, the CTE declines rapidly when cooled below room temperature and this decline continues until approximately 120 K below the point at which the CTE is small and less sensitive to temperature.

2.1.4 Perimeter augmentation

The key drawback to PZT actuation is the small stroke that can be generated; this is particularly problematic when large flow modulation is desired. The following simple calculation provides an estimate of the flow required to provide adequate cooling. For example, assume a potential application requires a 1.0 W of cooling load ($\dot{q}$) be accepted by a flow of helium at a nominal pressure (P_{nom}) of 1.0 MPa and temperature (T_{nom}) of 25

K. The temperature rise (ΔT) specifies the mass flow rate required ($\dot{m}$) according to an energy balance:

$$\dot{q} = \dot{m} c_p \Delta T \tag{2.4}$$

where c_P is the nominal constant pressure specific heat capacity. For a 1.0 W load with a 0.1 K temperature rise, the required mass flow rate is 1.8 g/s. The pressure drop (ΔP), coupled with the mass flow rate, specifies the nominal valve area (A_{valve}). The actual valve area required will be dependent upon the geometric details of the valve; however, if the pressure drop is inertia dominated (i.e., there are no long, tortuous paths that result in viscous pressure loss), the pressure drop may be related to the flow rate according to:

$$\Delta P = C_D \frac{\dot{m}^2}{2 \rho A_{valve}^2} \tag{2.5}$$

where ρ is the nominal density and C_D is a nominal discharge coefficient, not too different from unity. The pressure drop should be made as small as possible to avoid excessively burdening the fluid circulation mechanism; Eq. (2.5) illustrates the required valve area will be inversely proportional to the square root of the pressure drop. For the 1.8 g/s flow, Eq. (2.5) indicates a valve area of 3.0×10^{-6} m^2 is required (assuming that C_D = 1.0) in order to keep the pressure drop at 10 kPa (1% of the nominal pressure). This is a large flow area when compared to the capability of the PZT applications described above. Chakraborty et al. [15] utilized a PZT actuator able to produce 10 μm at most. Assuming a valve seat diameter of 5 mm, the maximum possible flow area achievable is 1.5×10^{-6} m^2, which is more than an order of magnitude less than the requirement.

The main challenge to sufficiently high flow modulation comes from the small displacement of PZT actuation, leading to only modest flow modulation. Furthermore, as we characterized in 2.1.3, the piezoelectric coefficient of PZT is substantially degraded at

cryogenic temperatures, further reducing the displacement. To overcome this limited displacement, a perimeter augmentation is used. The flow area for an out-of-plane valve (A_{valve}) is given by the product of the valve stroke (δ) and the perimeter of the valve seat (p).

$$A_{valve} = \delta \cdot p \tag{2.6}$$

Thus, by increasing the perimeter of the valve seat, the flow area can be increased substantially, which results in large flow modulation. Serpentine grooves are fabricated on the valve plate (5×5 mm^2) as shown schematically in Figure 2.5, so that the perimeter measures about 127 mm. Each groove measures 50 µm wide and 120 µm deep. The valve plate is suspended by four flexures in crab leg formation; each measures 500 µm wide, 4200 µm long, and 50 µm thick. These flexures are flexible enough to move freely upon the actuation of PZT (spring constant ≈ 500 N/m) but are rigid enough to hold the plate in place. This characteristic was verified by finite element analysis of the structure. Assuming the anodic bonding between the silicon and glass was performed at 400 ºC, at room temperature, the maximum stress of 21 MPa was observed at the corners of the bonding rim but the stress on the flexure and silicon valve plate was negligible.

The bonded die, PZT actuator, and ceramic enclosures are joined using Stycast epoxy, providing exceptional stability in cryogenic conditions. The valve has a total foot print of 1×1 cm^2.

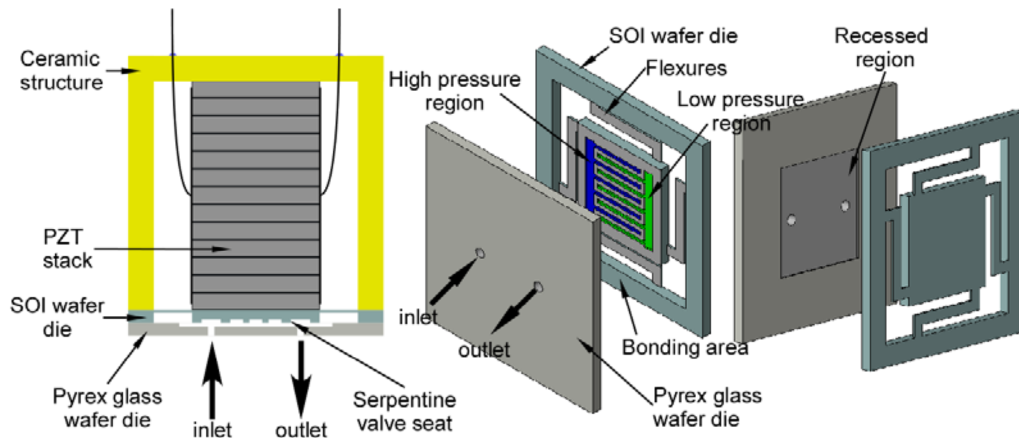

Figure 2.5: Microvalve concepts: The valve cross-section of the ceramic-PZT-Si-glass structure is shown on the far left. Micro groove patterns to increase flow area are depicted in the middle. The recessed glass along with the side view of the Si piece is illustrated on the right.

2.2 Modeling of the Microvalve

To optimally design the valve and characterize the prototype devices, development of predictive numerical models, which can be compared with experimental data, is essential. This section describes the flow model specific to the perimeter augmented microvalve, mainly developed by collaborators at the University of Wisconsin at Madison. One can consult Brosten's thesis for more detailed discussion on the modeling process [75].

To facilitate discussion of the flow model, the flow pattern of the valve is illustrated in Figure 2.6 and symbols are applied to the critical dimensions of the land and groove as in Figure 2.7.

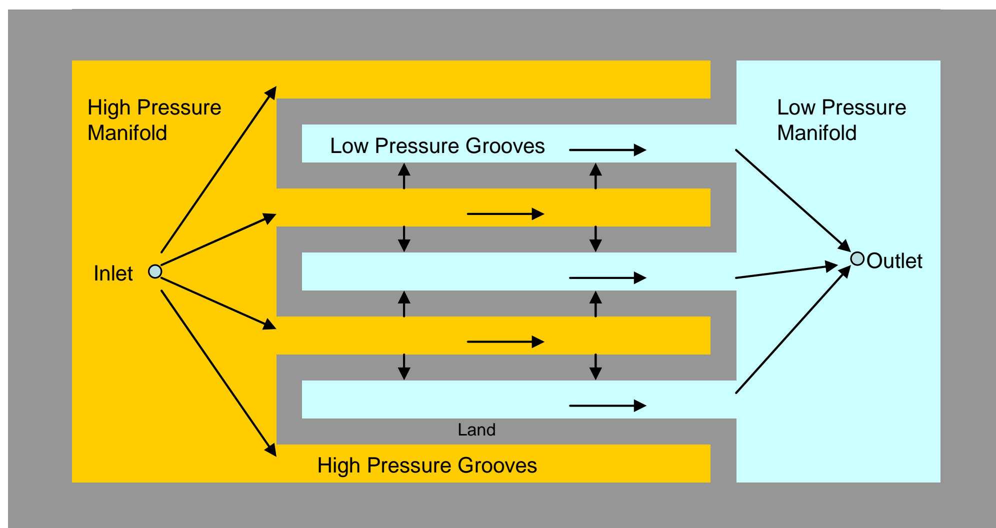

Figure 2.6: Flow pattern of the valve: Fluid flows from the inlet manifold to the high-pressure grooves, across the land region, the low-pressure grooves, then to the outlet.

The flow through the valve is divided into regions and each of the flow components of the valve are treated differently. The flow through the valve is assumed to be isothermal, laminar, and steady flow.

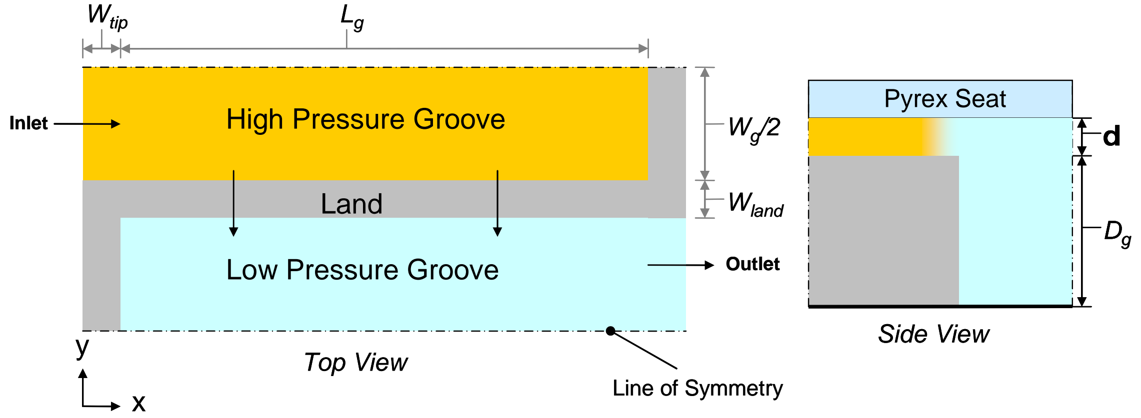

Figure 2.7: Top and side view of the land and groove region with assigned symbols.

2.2.1 Flow through the grooves

With the assumptions discussed above and the additional assumptions of incompressible, no slip, fully developed flow, the flow within the grooves may be represented by the constitutive equation:

$$-\frac{dP_g}{dx} = \underbrace{\frac{f}{D_h}\frac{\rho}{2}V_g^2}_{\text{Viscous term}} + \underbrace{\rho V_g \frac{dV_g}{dx}}_{\text{Inertial term}} \tag{2.7}$$

where P_g and V_g are the pressure and velocity of the fluid or gas within a groove, f is an empirically determined friction factor, D_h is the groove hydraulic diameter, and ρ is the density. The empirical friction factor was determined by successive adjustment of the boundary conditions for an idealized three-dimensional groove model, using FLUENT 6.2, and plotted in Figure 2.8. An inertial term is added to the typical viscous term in Eq. (2.7) to account for pressure changes resulting from the substantial effect of fluid deceleration (in the high-pressure groove) and acceleration (in the low-pressure groove) occurring due to the removal/addition of fluid into/from the land, respectively.

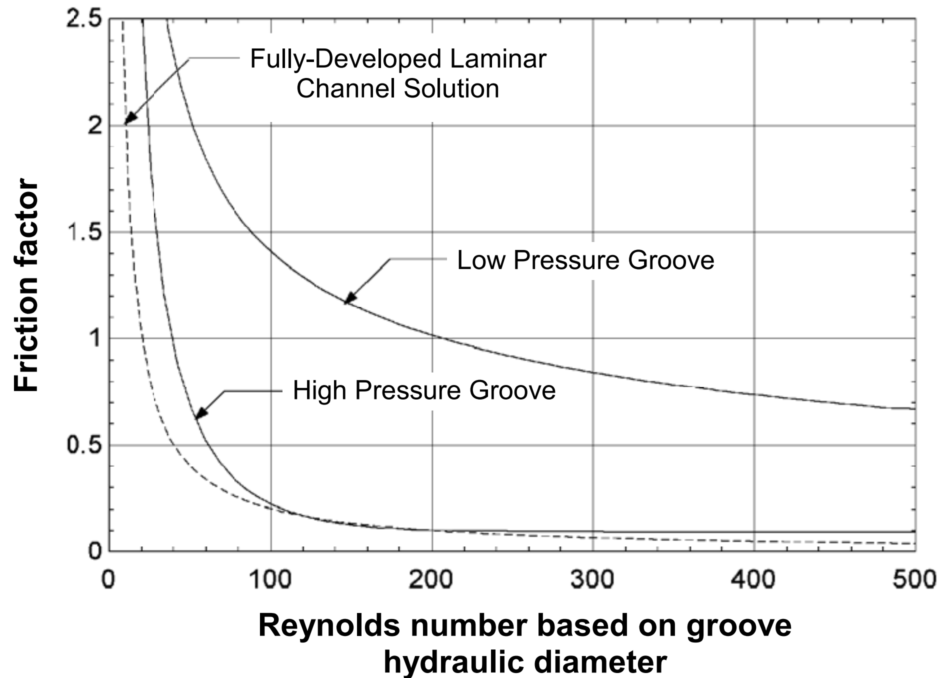

Figure 2.8: Groove friction factor as a function of the Reynolds number based on the groove hydraulic diameter.

Equation (2.4) coupled with the correlations illustrated in Figure 2.8 provide the basis for a 1-D, numerical model of the groove.

2.2.2 Flow through the land

The maximum value of the seat clearance, δ, is expected to be a few micrometers. This small length scale suggests that slip and compressibility effects will have a large effect on the flow characteristics within the land (although they could be appropriately neglected in the groove, which has a larger dimension by several orders of magnitude). Furthermore, for low molecular weight gases (e.g. helium) at high flow rates, a departure from viscous dominated flow is expected and compressibility effects across the land become significant. Therefore, a one-dimensional equation accounting for slip and compressibility effects was chosen to govern flow across the land [76].

$$\dot{m}' = \frac{\delta^3 P_o^2}{24 \mu L R T}\left[P_r^2 - 1 + 12\sigma Kn\left(P_r - 1\right)\right] \tag{2.8}$$

where $\dot{m}'$ is the mass flow rate per unit channel width, δ is the gap height, P_o is the outlet pressure, μ is viscosity of the fluid, L is the channel length, R is the ideal gas constant, T is the temperature, K_n is the Knudsen number based on δ, and P_r is the ratio of inlet pressure to the outlet pressure. Equation (2.8) provides the basis for a 1-D model of the flow across the land. That is, the flow per unit length of the land at any location x along the groove is assumed to be driven by the local groove-to-groove pressure difference. In fact, the pressure in the grooves is not constant and therefore there will be pressure gradients in the y- as well as the x-direction in the land. However, a detailed study of the impact of the two-dimensionality of the land flow behavior on the overall flow found that the two-dimensionality could be neglected with essentially no loss of accuracy because, for a well-designed valve, the flow over the land will be primarily one-dimensional.

2.2.3 The microvalve flow model

In the preceding sections, component level models were developed to represent the flow along the grooves, across the land, and the inertial loss occurring as the flow enters the land from the high-pressure groove. The component level model for flow through the land is based on the one-dimensional flow of a rarefied compressible gas through a channel. These physically-based component level models are interconnected through the steady state numerical solution of interconnected governing equations; these algebraic equations are based on satisfying continuity. The resulting system of equations is solved using the Engineering Equation Solver (EES) [77]. Differential control volumes within the grooves and the land are shown in Figure 2.9.

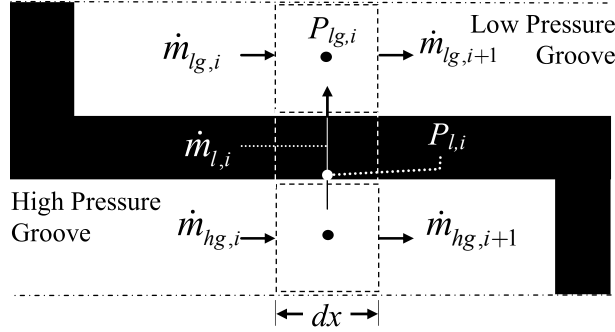

Figure 2.9: Mass balance terms for the control volumes of the numerical solution.

Continuity applied to the high-pressure groove control volume can be expressed as:

$$\dot{m}_{hg,i} = \dot{m}_{hg,i+1} + \dot{m}_{l,i} \tag{2.9}$$

The governing equation for the flow in the high-pressure groove expresses the pressure drop in terms of a viscous loss and an inertial term, as described in Eqn. (2.7). The governing equation is discretized according to:

$$\frac{P_{hg,i-1} - P_{hg,i}}{dx} = \frac{f_{hg,i}}{D_{h,hg}} \frac{\rho_{hg}}{2} V_{hg,i}{}^{2} + \rho_{hg} V_{hg,i} \frac{dV_{hg,i}}{dx} \tag{2.10}$$

where the velocity, $V_{hg,i}$, is related to the mass flow rate according to:

$$V_{hg,i} = \frac{2\,\dot{m}_{hg,i}}{\rho_{hg}\, A_{c,hg}} \tag{2.11}$$

For a complete discussion of the numerical solution scheme, including boundary conditions and the coupling to the manifolds, please refer to [75]. The solution of the system of equations provides the flow through the valve given its actuation state (i.e., the valve clearance) and operating conditions (i.e., the pressures at the inlet and exit, the inlet conditions, and the type of fluid).

To assist with the design of the microvalve, a set of simulations was carried out using the numerical model. First, in order to see the effect of perimeter augmentation, total flow rate is observed while varying the groove length, L_g. All other parameters are

kept the same as listed in Table 2.2. The plot is generated, while L_g is varied from 5 μm to 2800 μm.

Variable	Description	Value
d	Clearance between land and seat	3.687 μm
L_g	Length of the groove	2800.0 μm
W_{land}, W_{tip}	Width of the land and top	50.0 μm
D_g	Depth of the groove	100.0 μm
P_H	Inlet high-pressure	135.8 kPa
P_L	Outlet low-pressure	101.3 kPa
r	Density of air (25 °C and 1 atm)	1.587 kg/m^3
m	Viscosity of air (25 °C and 1 atm)	1.876 μg/m-s

Table 2.2: Variables used in the simulation.

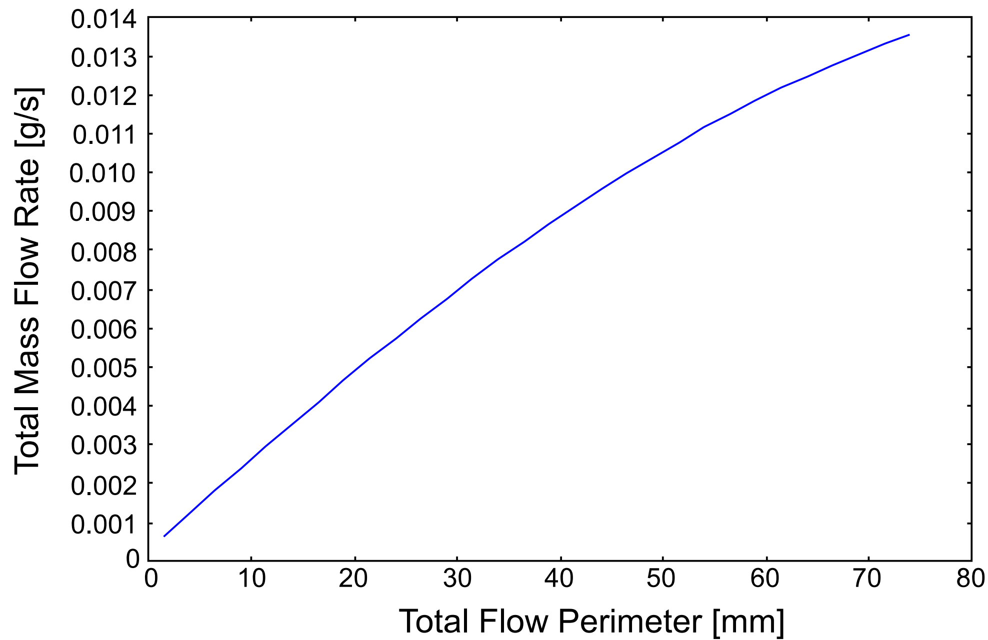

Figure 2.10: Simulation results showing the effect of perimeter augmentation.

For a valve seat without perimeter augmentation, the total flow perimeter would be less than 12 mm. The perimeter augmentation can increase the flow perimeter in excess of 100 mm. The end-result would be an almost 400 % increase in flow rate. The relationship is not quite proportional and exhibits decreasing gain at larger perimeters.

This is probably due to increased viscous losses in flow along the grooves and the inlet and outlet hole diameters becoming a limiting factor. Nevertheless, the benefit of perimeter augmentation can be clearly seen.

An example of the outcome of the model is shown in Figure 2.11 for nitrogen flow at room temperature. The plot is generated employing the parameters used for the testing, and the experimental measurements are compared with the flow model prediction in section 2.4.

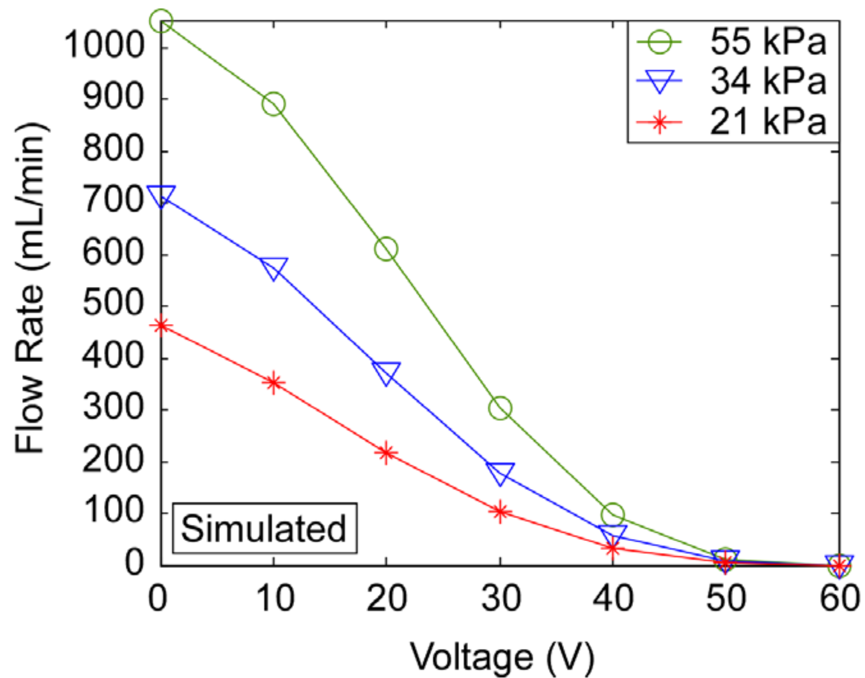

Figure 2.11: Valve flow model prediction: Room temperature nitrogen flow rate at various inlet pressures.

2.3 Device Fabrication

To ensure control of material properties, the final device is comprised of only bulk materials. Deposited thin films are not used for any structural layer, although they are employed in intermediate steps. The fabrication process uses two wafers: a silicon-on-insulator (SOI) wafer, which has device layer, buried oxide layer, and carrier wafer thicknesses of 50 μm, 0.5 μm, and 450 μm, respectively, and a 500 μm thick Pyrex glass wafer. The fabrication processes for SOI and glass wafers are illustrated in Figure 2.12.

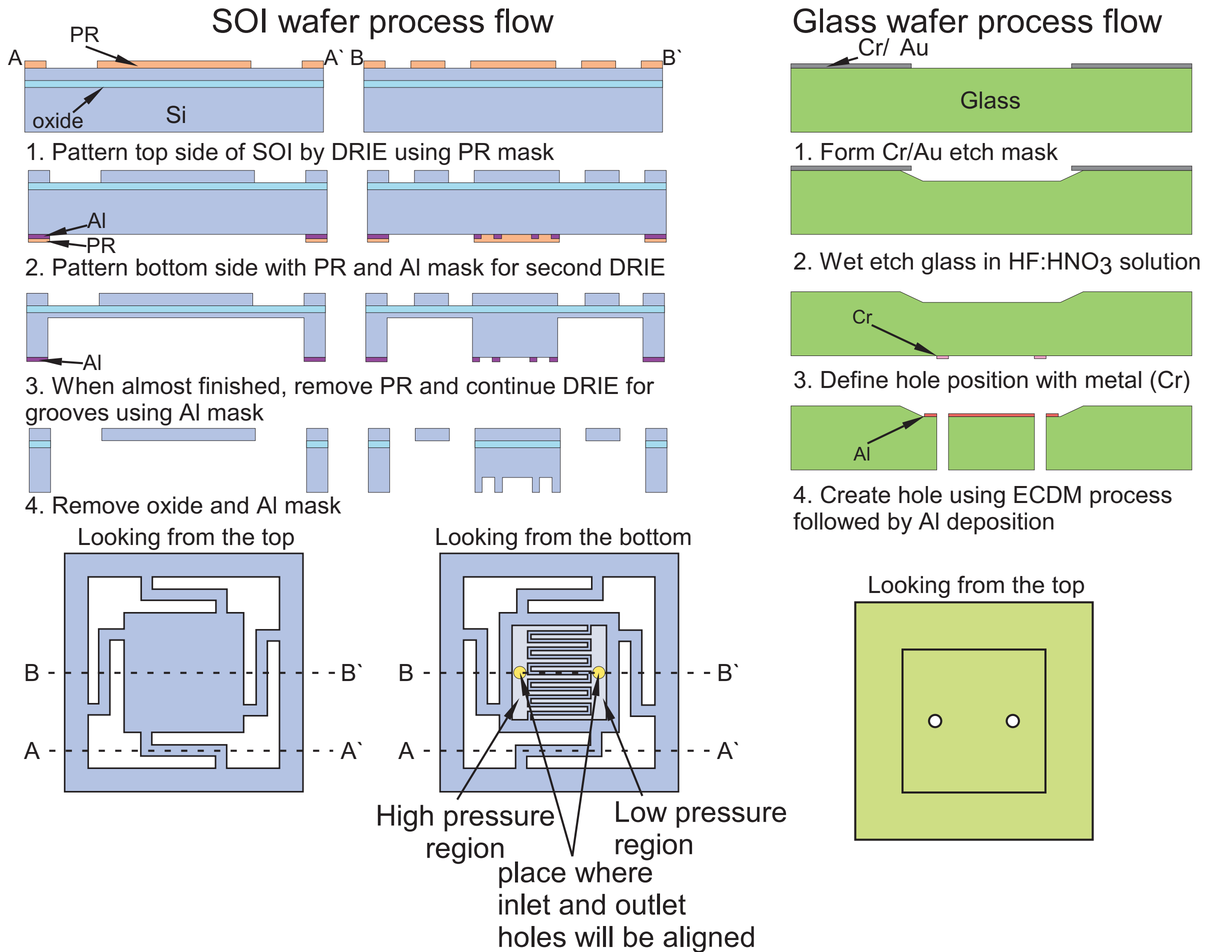

Figure 2.12: Si-glass micromachining process: The buried oxide layer in the SOI wafer acts as an etch stop for DRIE. A three-step DRIE process is illustrated for the SOI wafer. A glass wafer undergoes a wet etch process and a electrochemical discharge machining process for inlet and outlet hole creation. Finally, the Al metal layer is deposited and patterned in preparation for anodic bonding to prevent bonding of the valve seat to the glass substrate.

2.3.1 SOI Wafer Fabrication

Deep reactive ion etching (DRIE) of silicon was used to form flexures, the valve plate, and groove patterns in the plate. DRIE provides high etching speed, high aspect ratio capabilities, and good selectivity. However, the uniformity of DRIE is not reliable across a full wafer [78,79]. The use of the SOI wafer solves the problem. The buried oxide layer in the SOI wafers provides an etch stop for DRIE, while the top device layer provides a well-controlled flexure thickness, smooth surfaces, and bulk Si properties. The first DRIE step etches down to the buried oxide layer from the top and defines the flexure structures. Then the bottom side is patterned with Al and photoresist. The photoresist acts as an etch mask for the second DRIE step that is approximately 400 μm deep. Next, the photoresist is removed and Al is used as an etch mask for the final DRIE step, which engraves serpentine grooves for perimeter augmentation. The Al layer is then removed and the wafer is prepared for bonding. Scanning electron microscope (SEM) images of a valve plate, after these three-step DRIE, are shown in Figure 2.13. The entire valve seat is pictured in (a), while (b) and (c) show the cross-sectional view. Each groove width is 50 μm, and is etched approximately 120 μm deep.

(a)

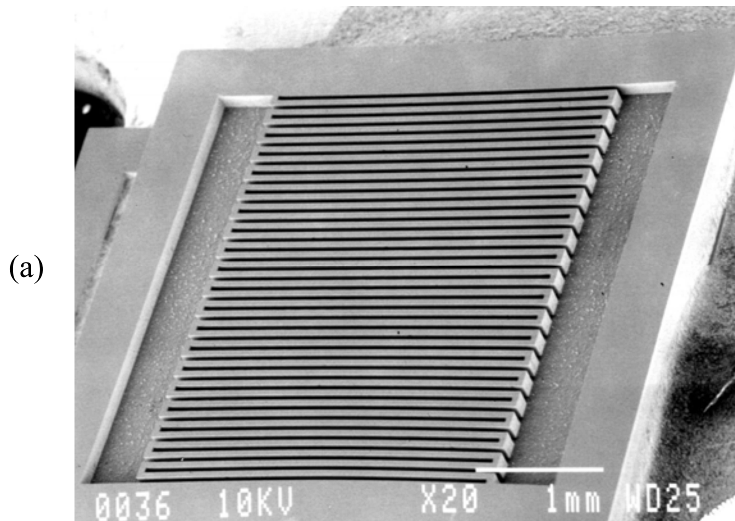

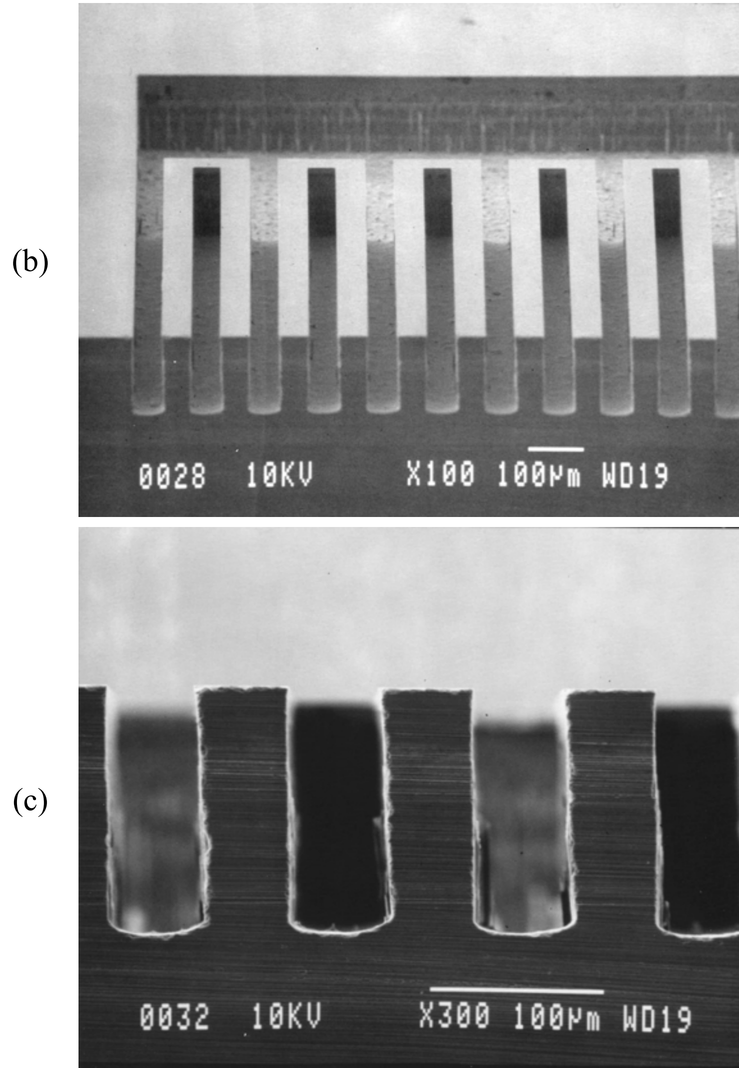

Figure 2.13: SEM photographs of grooves on a valve plate fabricated by DRIE. (a): Valve plate. Part of a flexure is also seen on the left side, (b) and (c): A valve plate is diced to expose the cross-sectional view.

2.3.2 Glass Wafer Fabrication

For the glass wafer, a recess of 2 μm is made to accommodate the PZT displacement (Figure 2.16). The recess is formed by wet etching the glass in a H_2O:HF:HNO_3=10:7:3 solution, using a Cr/Au/PR layer as an etch mask. After the recess formation, the etch mask is removed and a thin Cr layer (100 nm) is patterned to define the position of inlet and outlet holes that are formed using electrochemical discharge machining (ECDM) [80]. ECDM was chosen for through-hole formation

against wet etching the glass because wet etching results in significant undercut. ECDM of glass is a rapid, low-cost method, providing a near-vertical profile, suitable for hole formation. The procedure is performed in a 40% NaOH solution at room temperature, and the glass is machined using approximately 300 μm diameter tungsten cathode and 37 V bias. The ECDM setup is shown schematically in Figure 2.14. After the holes are formed, the residual Cr layer is removed. Some SEM pictures of the holes formed by ECDM are presented in Figure 2.15.

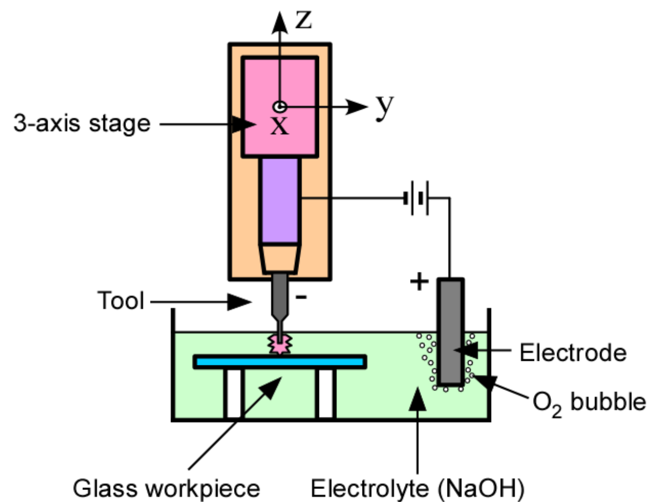

Figure 2.14: Schematics of the ECDM setup for machining glass wafers.

(a)

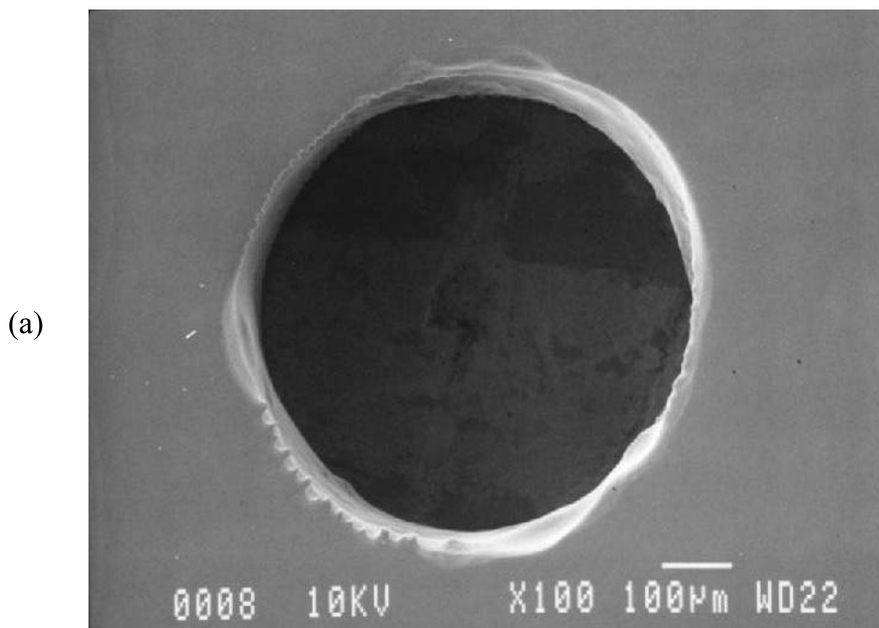

(b)

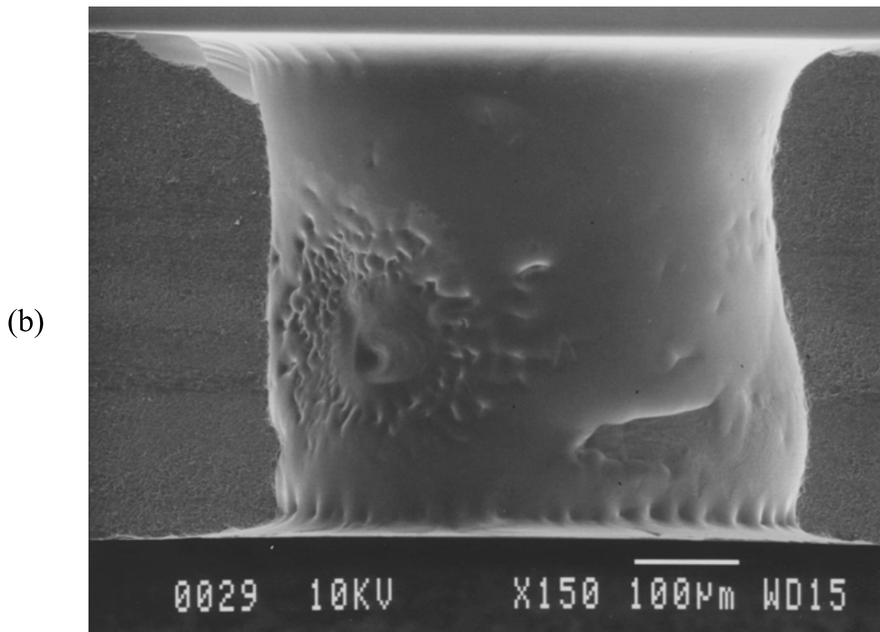

Figure 2.15: SEM photograph of a hole in a Pyrex glass wafer formed by ECDM process: (a) Top view and (b) the cross-sectional view.

Before performing the bonding of the Si and glass wafers, a thin layer of Al must be deposited into the glass recess to prevent inadvertent bonding of the valve plate to the glass substrate due to a shallow recess depth and very compliant flexures. Anodic bonding is performed at 400˚C and 800 V, after which the Al layer on the SOI wafer is dissolved. The bonded wafers are then diced and prepared for assembly with the ceramic structure and PZT.

2.3.3 Device Assembly

The final step is to attach the PZT stack and ceramic cap by epoxy. The piezoelectric actuation provides enough force to displace the Si against inlet pressures, which in some instances can reach several atmospheres. The first prototype valve tested at room temperature was assembled using regular Devcon 2-part epoxy. However, Devcon epoxy is rated down to only -40˚C, so for cryogenic testing, Stycast 2850 FT epoxy is used. The PZT does not need to be bonded to the Si and was not bonded for

cryogenic testing. This may also relieve any stress on flexures caused by large temperature variation. To create a normally-open valve, the PZT stack is energized at 100 V during the assembly process, so that it shortens after assembly as the voltage is reduced during operation (Figure 2.16). Notice in the figure that the epoxy not only acts as an adhesive layer but also compensates the height difference between the PZT actuator and the ceramic housing. The completed valve structure with a final dimension of 1×1×1 cm^3 is pictured in Figure 2.17.

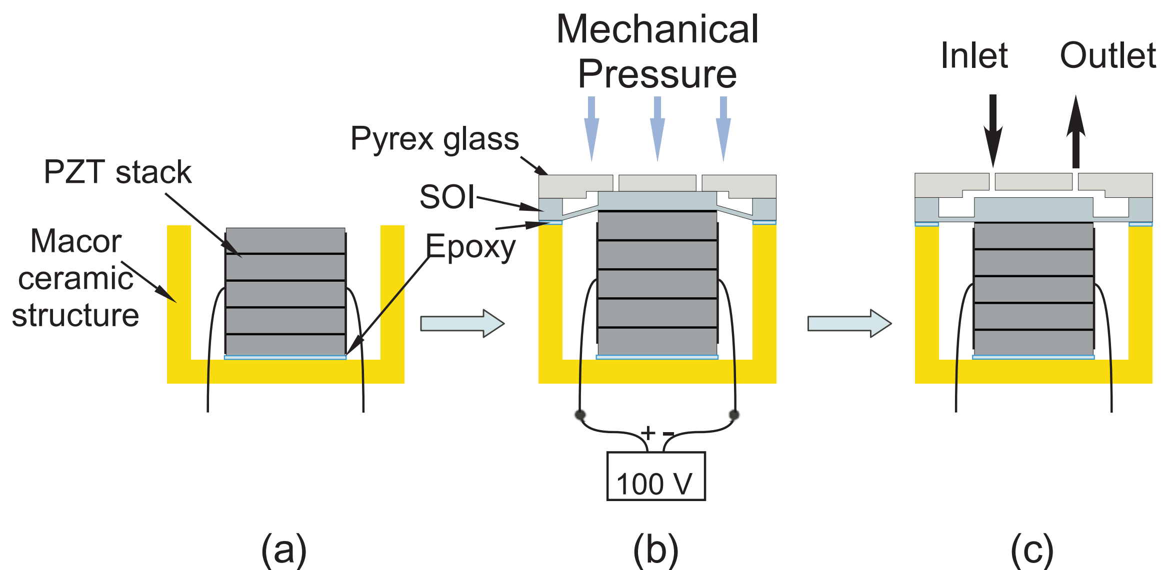

Figure 2.16: Pre-stressed microvalve assembly procedure: (a) First, a PZT stack is attached to the Macor ceramic structure using epoxy. (b) Then a Si-glass die is bonded at the end of the PZT and Macor structure by an epoxy joint. During this procedure, the PZT stack is actuated until the epoxy is fully cured, which results in a normally-open valve (c).

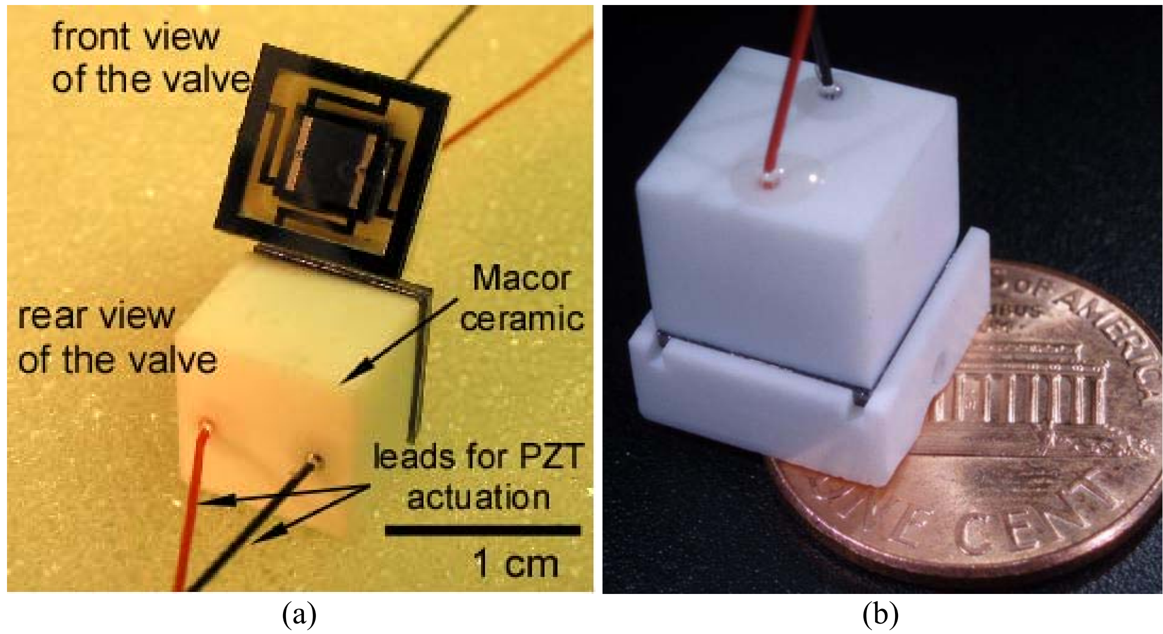

(a) (b)

Figure 2.17: Completely assembled valve structure. (a) Two valves (front and back) are shown. (b) Another view of the valve with the Macor header and a US penny.

2.4 Experimental Results

First, room temperature tests were conducted to verify the model and establish baseline performance characteristics of the valve at low and high pressures. Next, cryogenic experiments were undertaken to verify operation and determine temperature effects on the device. Lastly, high temperature testing was performed to yield more information on the temperature dependencies of the valve.

2.4.1 Room Temperature Flow Test

Initial tests were performed at room temperature with He gas flow. Figure 2.18 illustrates a schematic of the test. An in-line thermoplastic filter is placed upstream of the device to trap any particles or moisture. Pressure gauges are mounted so that inlet and outlet pressure can be monitored. Copper piping (6.35 mm diameter) is connected to 0.4 mm holes in glass through an aluminum header. A ball valve is added at the end so that the outlet pressure can be controlled if necessary.

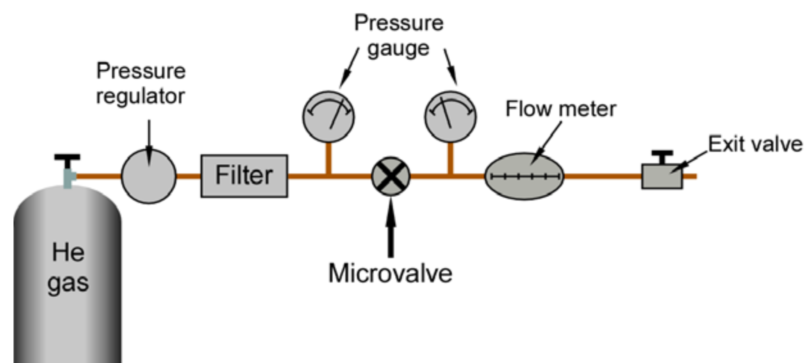

Figure 2.18: Schematic of the room temperature flow measurement test apparatus.

In the first set of tests, the inlet pressure was regulated (21-55 kPa, gage), and the outlet was maintained at atmosphere, while the flow rate was measured over 0-60 V actuation. As shown in Figure 2.19, as actuation voltage increases, the PZT expands, the

clearance between the silicon valve seat and the glass substrate decreases, and thus, the flow rate decreases. With the gauge pressure of 55 kPa at the inlet, flow rate could be modulated from 0 to 980 mL/min. At 60 V, the valve leakage was below the measurement limit (< 0.1 mL/min.).

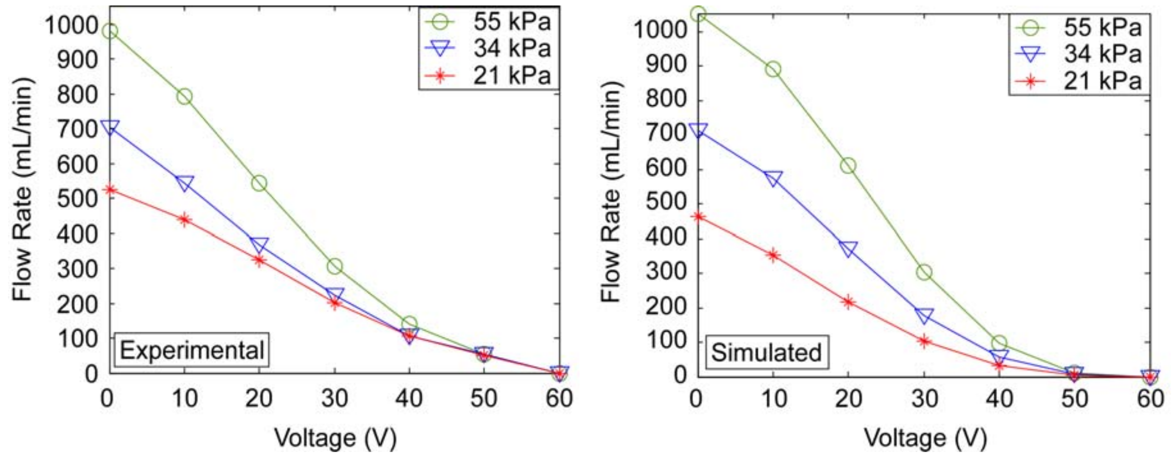

Figure 2.19: Flow rates as a function of voltage from experimental results and the analytic model. As the actuation voltage increases, the valve is closed, which results in a decrease in flow rate.

These test results were compared with predictions from the numerical flow model previously described in section 2.2. Figure 2.19(b) was obtained by assuming that the hole diameters for inlet and outlet are 350 μm and displacement of PZT at 60V is 4 μm. In addition, a linear relationship between PZT displacement and voltage was assumed. Thus, seat clearance from the glass substrate can be expressed as in Eq. (2.12).

$$Clearance\ (\mu m) = 4 - Voltage(\mathrm{V}) \cdot 0.067 \tag{2.12}$$

The flow rates from the model tend to fall slightly faster than the experimental results, but in general, they match reasonably well. The main discrepancy comes from uncertainties in seat clearance and inaccurate inlet and outlet hole sizes used in the model. Compressibility of He gas and hysteretic behavior of PZT also contribute to the difference between the model and experimental data.

In a separate experiment, the valve was tested at a higher inlet pressure of 345 kPa gauge pressure to verify its operation at high pressure, but the pressure difference between the inlet and outlet was kept at 34.5 kPa since that is the anticipated operating condition for the valve. The test setup for this set of experiments is schematically shown in Figure 2.20. A pressure vessel was used to obtain a high absolute pressure while maintaining a relatively low pressure differential across the valve at room temperature. Absolute pressure was measured at the inlet of the valve while the pressure difference across the valve and volumetric flow rates were measured. Multiple throttling valves were utilized downstream of the valve to allow precise regulation of the pressure difference at high absolute line pressure.

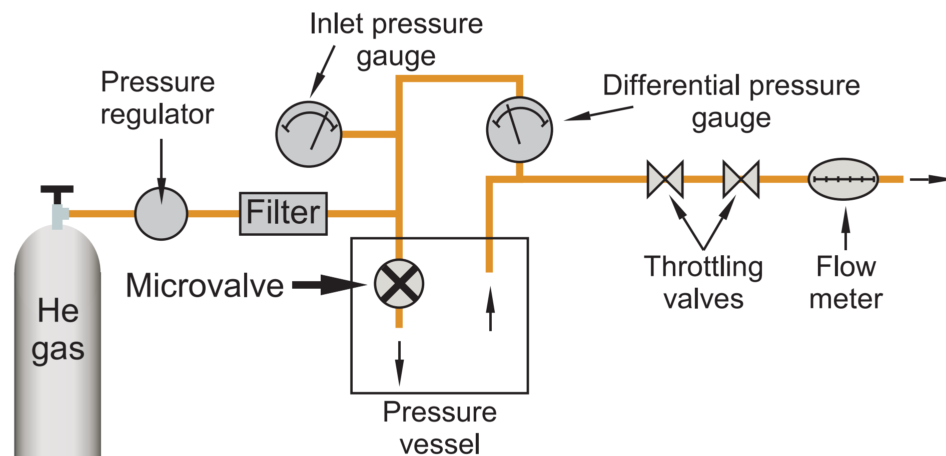

Figure 2.20: Schematic of the test setup for the high-pressure room-temperature gas flow measurement.

Tests were conducted by holding the inlet pressure and differential pressure constant while increasing the valve actuation voltage from 0 to 100 V, and then reducing the voltage back to 0 V in 10 V increments. The test result comparison with the model prediction is shown in Figure 2.21. The flow rate measurements reveal the hysteretic

behavior of the PZT actuator. The model and the experimental results show good agreement.

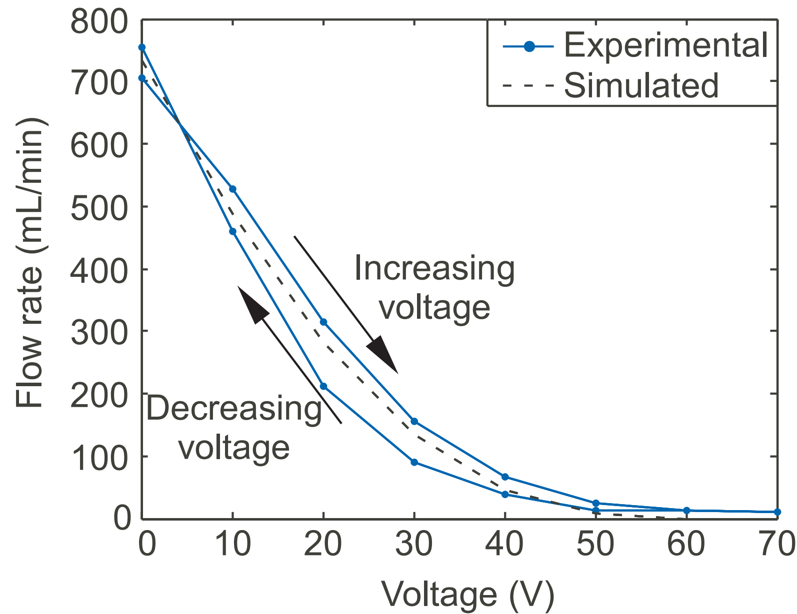

Figure 2.21: Flow rates as a function of actuation voltage measured at room temperature with an inlet pressure of 345 kPaG and an inlet to outlet pressure differential of 34 kPa. Experimental data are shown with the numerical modeling results. Flow rate measurements present the hysteretic behavior of the PZT actuator.

2.4.2 Cryogenic Temperature Flow Test

To verify the operation of the valve at cryogenic temperatures, experiments were performed near liquid nitrogen temperatures (80 K). (For this valve, Stycast epoxy and a Macor header were used, and the PZT was not bonded to the Si valve plate.) Heat exchangers were added to the test setup as shown in Figure 2.22. The He gas was cooled by passing it through a liquid nitrogen heat exchanger. Inlet and outlet pressure were monitored. In addition, thermocouples were used to probe the inlet and outlet gas temperature. The gas was then passed through another heat exchanger to bring it back to room temperature and exhausted to the atmosphere while the flow rate was measured.

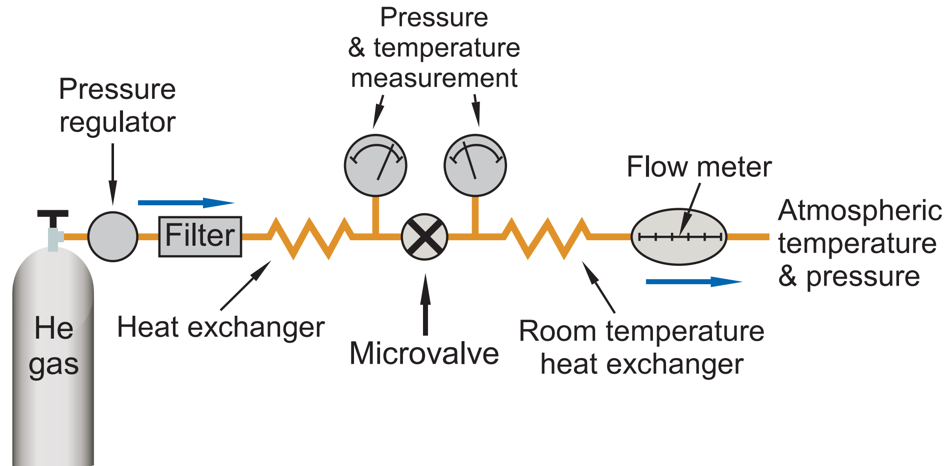

Figure 2.22: Schematic of the test setup for cryogenic flow measurement.

The valve performance is shown in Figure 2.23 for inlet gauge pressures of 35 kPa, 70 kPa, and 104 kPa with predicted flow rates using the model. Since the piezoelectric coefficient at 80 K is diminished from its room temperature value, the voltage required to completely stop flow is almost doubled to a value of about 120 V. Reasonable agreement between the experimental data and the model predictions is obtained by assuming an initial valve seat clearance of 1.03 μm. The reduced valve seat clearance is most likely due to an expansion mismatch between the PZT and Macor enclosure.

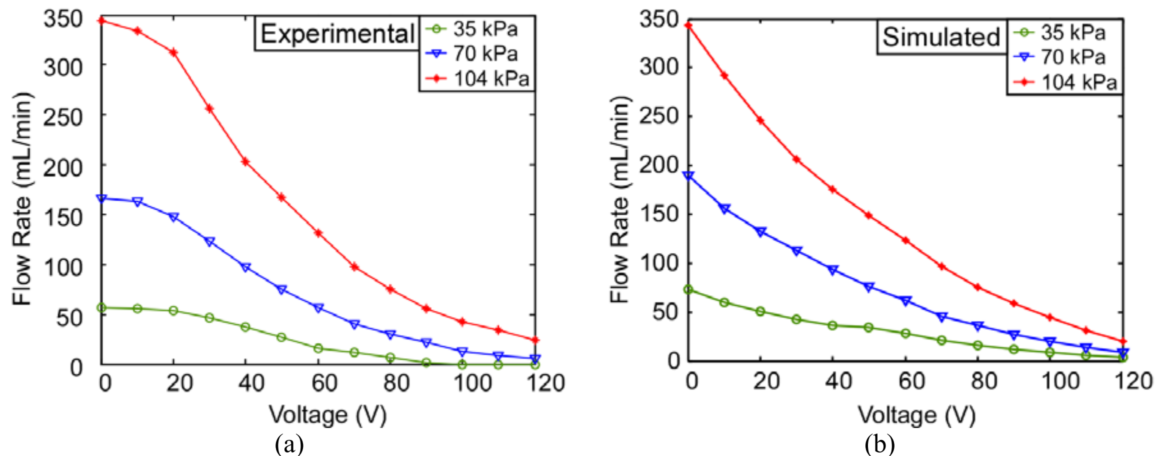

Figure 2.23: (a) Measured flow rates as a function of voltage at liquid nitrogen temperature (80 K) compared with (b) the analytic model.

The normalized flow rate (NFR) is presented in Figure 2.15. This is defined as:

$$NFR = \frac{flow\ rate\ at\ corresponding\ voltage}{flow\ rate\ at\ 0V} \tag{2.13}$$

In Figure 2.24, the three curves obtained at different inlet pressures appear very similar. This similarity illustrates consistent modulation of the valve over the range of inlet pressures tested.

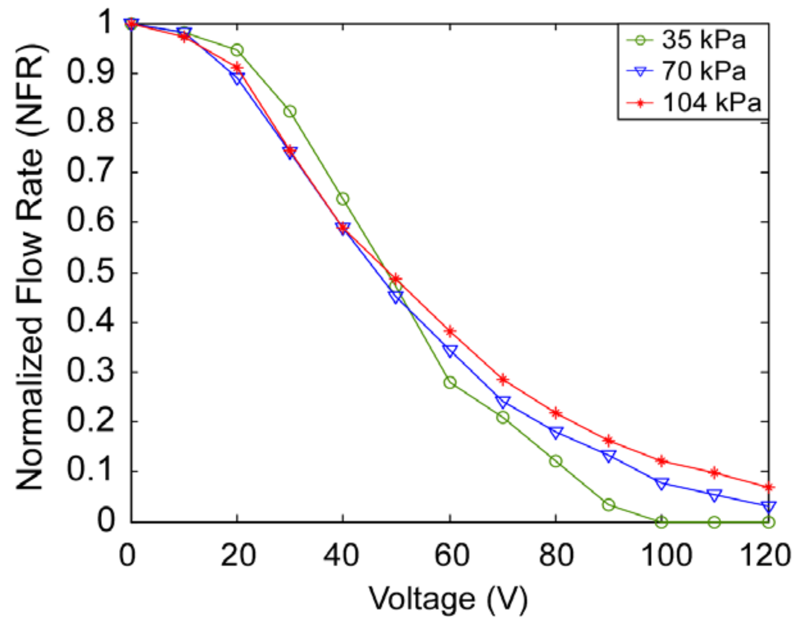

Figure 2.24: Normalized flow rate vs. actuation voltage obtained at cryogenic temperature.

2.4.3 High Temperature Flow Test

Although these valves are fabricated to be used for cryogenic applications, they have been tested at elevated temperatures up to 110˚C to examine their operating temperature range and to explore other possible applications. The experimental setup for the high temperature test was very similar to that of the cryogenic temperature, but instead of exposing the heat exchanger and the valve to liquid nitrogen, they were submerged in a heat bath at 110˚C. To compare the valve's room temperature behavior with that at high temperature, data was collected at both temperatures and plotted in Figure 2.25. At an un-actuated state, the flow rate was higher at an elevated temperature

and required a much larger actuation voltage (170 V) to completely close the valve. This result occurs because the thermal expansion of Macor is larger than that of PZT, resulting in a larger separation of the silicon valve plate from glass at zero actuation voltage. To fully close the valve, the PZT needs to travel further, requiring a larger actuation voltage at elevated temperatures compared to room temperature.

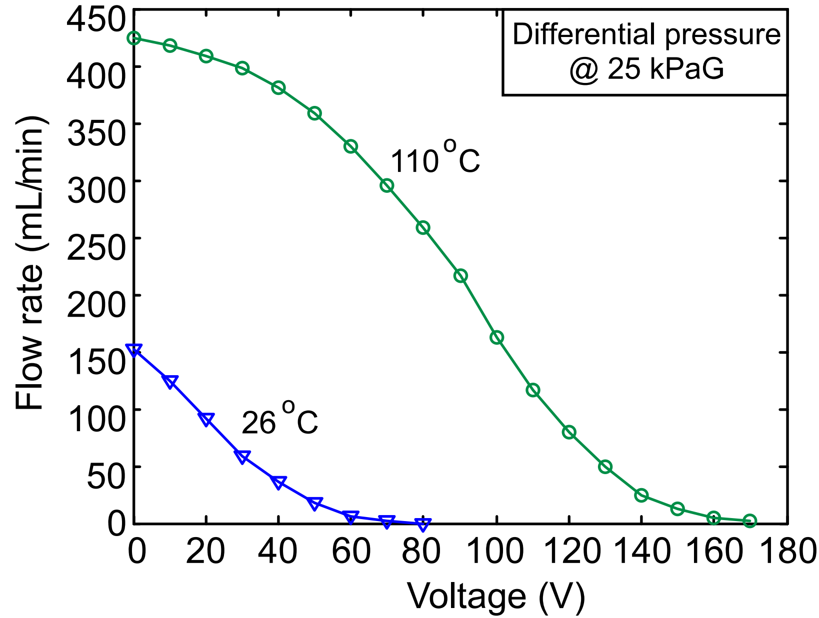

Figure 2.25: Measured flow rates as a function of voltage at 110˚C and 26˚C with inlet pressure of 25 kPa.

The high actuation voltage suggests a conservative upper limit of operating temperature of this particular valve is somewhat lower than 110˚C, because the PZT manufacturer recommends the upper limit of the actuation voltage to be 120 V. However, the manufacturer also states the PZT itself can be used up to 150˚C. Therefore, extending the operation of the valve up to 150˚C is possible in at least two ways. One method is to tailor the valve assembly process to use the valve for high-temperature application. Note that these valves are assembled at room temperature while actuating the PZT at 100 V to acquire a normally-open state. If we assemble a valve at lower voltage or even at 0 V, expansion of the Macor at high-temperature will result in a normally-open valve at high-

temperature, and the gap will be small enough to close without over-actuating the PZT. Another solution involves finding an alternative material to be used in place of the Macor. If a material with a lower thermal expansion coefficient is used for the valve, it could truly expand the valve's operating temperature range.

2.4.4 Dynamic Characteristics

A finite element analysis and PSPICE™ simulation were performed to model the transient behavior of the valve and also analyze its frequency response. Then the model was verified by vibrometer measurement. A Von-Mises stress analysis of silicon and glass die showed at room temperature stress is mainly present at the bonding interface. A maximum stress of about 21 MPa is calculated at the corners of the bonding rim, and the crab-leg flexures successfully relieve the stress and leave the valve plate and the flexures virtually stress free. Modal analysis evidenced the first resonant frequency of the valve plate is at 739 Hz and subsequent resonant frequency, which is the tilting motion of the valve plate, occurs at 1.3 kHz. An equivalent circuit model for the valve was constructed taking into account the electrical and mechanical property of the PZT actuator and the Si valve plate. However, electrical impedance of the PZT actuator was found to be a dominant factor in transient and frequency response of the microvalve. The actuator has a relatively large capacitance value (648 nF), which is a characteristic of a stacked PZT actuator. The actuator is modeled as a parallel RC circuit and the equivalent circuit parameters are measured using RLC meter. The PSPICE transient analysis showed an approximately 670 μs transition time with a 3 dB bandwidth at 710 Hz.

To accurately measure the dynamic behavior of the valve, a laser Doppler vibrometer (Polytec, Inc., PSV-400 sensor head with OFV-5000 controller) was used. A

step input from 0-100 V was applied to the actuator while the Si valve seat displacement was measured with a sampling rate of 1.28 MHz. The measured results are presented in Figure 2.26. The plot illustrates the response time of 700 μs, which is in good agreement with the PSPICE analysis result. The small oscillation is likely due to the mechanical properties of PZT, such as the stiffness and damping factors.

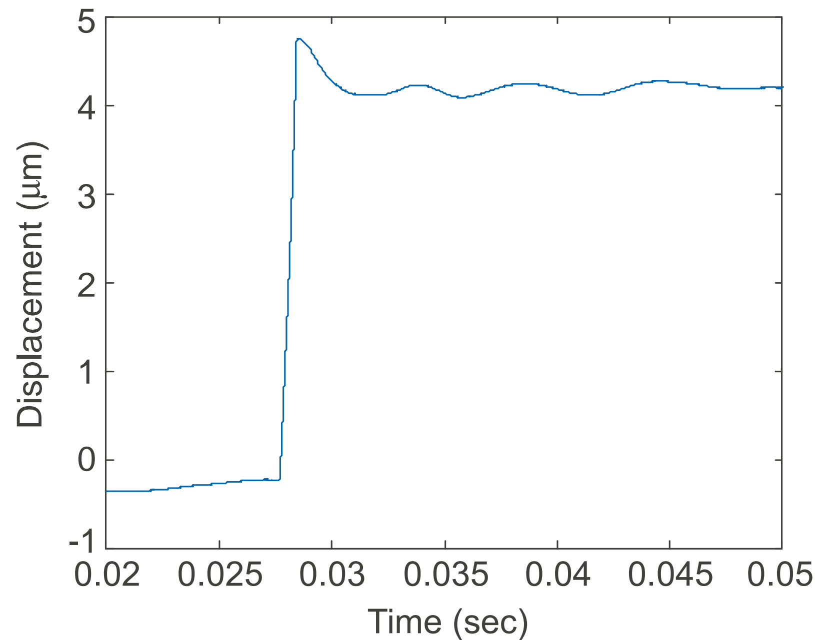

Figure 2.26: Transient response of the valve measured using a laser Doppler vibrometer with a sampling rate of 1.28 MHz. The response time for 0 to 100 V actuation is measured to be 700 μs. Some oscillations are evident due to the mechanical properties of PZT.

To find the operational bandwidth of the valve, the displacements were measured while a 0 to 100 V square wave was applied from 100 Hz to 4.5 kHz in 100 Hz increments. The amplitudes were normalized to the DC value and are plotted in Figure 2.27. The -3 dB mark occurs at around 820 Hz, which is comparable to the bandwidth found by equivalent circuit model using PSPICE. This confirms that the bandwidth is limited by the electrical capacitance of the PZT.

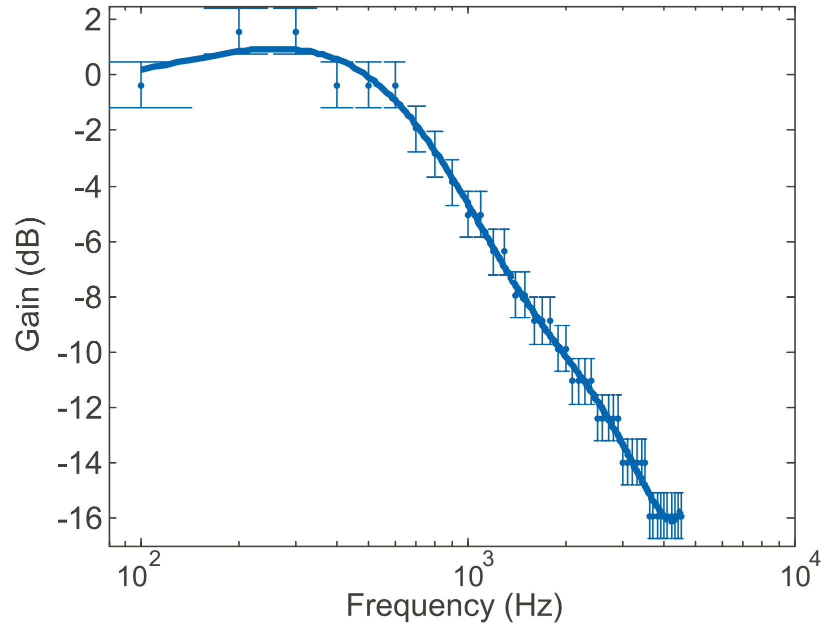

Figure 2.27: The bandwidth of the valve at room temperature is determined by 100 V square waves applied from 100 Hz to 4.5 kHz in 100 Hz increments. The displacements are measured and normalized to the DC valve. The dots represent data points with error bars. The best fit curve is also plotted. The 3 dB bandwidth occurs at around 820 Hz.

At 60 V steady state actuation, the leakage current through the actuator was measured to be only 2.7 nA, which means the valve only consumes 0.16 μW of power. Most power consumption occurs during open to close transition of the valve. In other words, more frequent transition results in higher power consumption. Using the measured impedances of the PZT actuator, PSPICE simulation showed the power consumption of 2.3 mJ per 0 to 60 V actuation cycle.

2.5 Discussion and Conclusions

This effort has resulted in the successful fabrication of a piezoelectrically actuated ceramic-Si-glass microvalve for distributed cooling applications. Piezoelectric actuation provides proportional flow control that generates enough force to withstand high inlet pressures with minimal power consumption. At steady state, the valve only consumes 0.16 μW of power. A perimeter augmentation scheme was used to overcome the limited displacement of PZT and provide large flow modulation. The valve was tested across a wide range of temperatures. At room temperature, a flow rate of 980 mL/min was measured with inlet pressure of 55 kPaG, which is orders of magnitude higher in flow modulation capability than previously reported piezoelectric microvalves [15, 47-48]. The operation of the valve was validated at inlet pressures up to 345 kPaG while maintaining a 34 kPa of pressure differential between inlet and outlet pressures, delivering a sufficient flow rate. The performance of the valve was evaluated at a wide range of temperatures. At cryogenic temperatures (80 K), higher voltages (≈120 V) were required to completely close the valve due to the degraded piezoelectric coefficient, and separation between the silicon valve seat and the glass plate was decreased as a result of thermal mismatch between the Macor and the PZT actuator. The valve successfully modulated gas flow from 350 mL/min down to 20 mL/min, at an inlet pressure of 104 kPa higher than the atmosphere, and it showed consistent modulation capability over different values of inlet pressures. The experimental results followed closely with predictions from the numerical model. The operation of the valves was also verified at elevated temperatures. The high actuation voltage required to close the valve at elevated temperatures suggests that a conservative upper limit of operating temperature is

somewhat lower than 110˚C. The transient analysis presented a 700 μs response time of the valve and the bandwidth of the device was measured to be 820 Hz.

CHAPTER 3

MICROVALVE WITH INTEGRATED SENSORS

This chapter addresses a piezoelectrically-actuated microvalve with integrated sensors that monitor inlet pressure and coolant temperature, and enable closed loop control of distributed cooling systems, in a compact form. Both sensors must work with a mixed-phase heterogeneous coolant, maintaining accuracy across a wide temperature range. In past efforts, microvalves were often integrated with flow sensors [81,82]. However, for our application, measurement of the inlet pressure and temperature of the coolant provides adequate information. The measured temperatures across the distributed network can be used by a controller to properly adjust cooling rates to various parts of the surface to provide a minimal thermal gradient. In addition, the results of the temperature sensor can be used to compensate for the temperature coefficients of the pressure sensor. This sensor integration is especially significant in space missions, as the launch cost increases exponentially with mass.

The two main pressure sensing techniques utilizing a membrane structure are piezoresistive sensing [83] and capacitive sensing [84]. The former, in a Wheatstone bridge configuration, was selected because it is more linear and has lower output impedance than capacitive readouts, allowing readout circuitry to be located remotely and sheltered from valve operating temperatures.

The most common methods of measuring temperature are thermocouples, diodes, and resistance temperature detectors (RTDs) [85]. As the entire device is exposed to the operating temperature of the valve, the requirement of temperature reference junction prevents the use of a thermocouple for the temperature sensor. Diode thermometry uses the temperature dependence of forward voltage drop in a p-n junction biased at constant current. However, this technique is very sensitive to the presence of radiation, due to the charging of oxide layers, and electromagnetic interference that might be present in open space can create magnetic field-induced voltage across the junction [86]. An RTD temperature sensor works by sensing change in resistance with changing temperature. The platinum RTD is known to have excellent linearity down to 70 K and measurement down to 14 K is routinely performed with appropriate calibration. A platinum RTD was selected as the temperature sensor for this work, because of its linear response in the range of our interest, industry-standard robustness, and ease of implementation.

The valves described have a normal state customizable during assembly to provide the necessary default flow rate for every distributed element. A default network can be designed with normally-open, normally-closed, and partially-open valves so the coolant network continues to maintain some functionality in the case of complete power failure.

A general description of the device design and its operation is described in section 3.1, the fabrication process is described in section 3.2, followed by experimental results and discussions.

3.1 Microvalve and Sensor Design

The device consists of three main components; a valve for flow modulation, a pressure sensor, and a temperature sensor for monitoring purposes. The basic valve structure and operation is kept similar to the one described in Chapter 2. The valve operates by pressing a suspended silicon plate against a glass plate using out-of-plane piezoelectric actuation. Piezoelectric actuation provides enough force to displace the silicon plate against large inlet pressure (above 1 atm) with negligible DC power consumption and acceptable cryogenic performance. A multi-layered PZT stack, having a 5×5 mm^2 footprint and a 6 mm height, is used as an actuator. The valve die and the piezoelectric actuator are housed inside a Macor structure (Figure 3.1). Macor is also used to create the fluidic header employed to connect the inlet and outlet of the valve to the rest of the flow path.

The perimeter augmentation scheme is utilized again to increase the flow area. Extended serpentine grooves (> 30 cm in length) are fabricated on the valve plate as shown schematically in Figure 3.1(a). Each groove measures 50 µm wide and 120 µm deep.

It is worth noting that the valve presented here has a membrane suspension. There are several advantages provided by this design compared to a valve with flexure type suspension described in Chapter 2. The membrane suspension prevents the fluid from entering the package cavity, and thereby greatly reduces the dead volume of the valve. The dead volume in the device is only 0.021 cubic centimeters, which is less than 1 % of the total valve volume. The membrane suspension is fabricated using a process easily integrated with a diaphragm pressure sensor. A channel is constructed to route the

inlet fluid pressure to the pressure sensing element. The thin silicon membrane between the flow path and strategically placed temperature sensor provides a path with a relatively small thermal resistance to the fluid, while preventing direct contact with it (Figure 3.2 and 3.3).

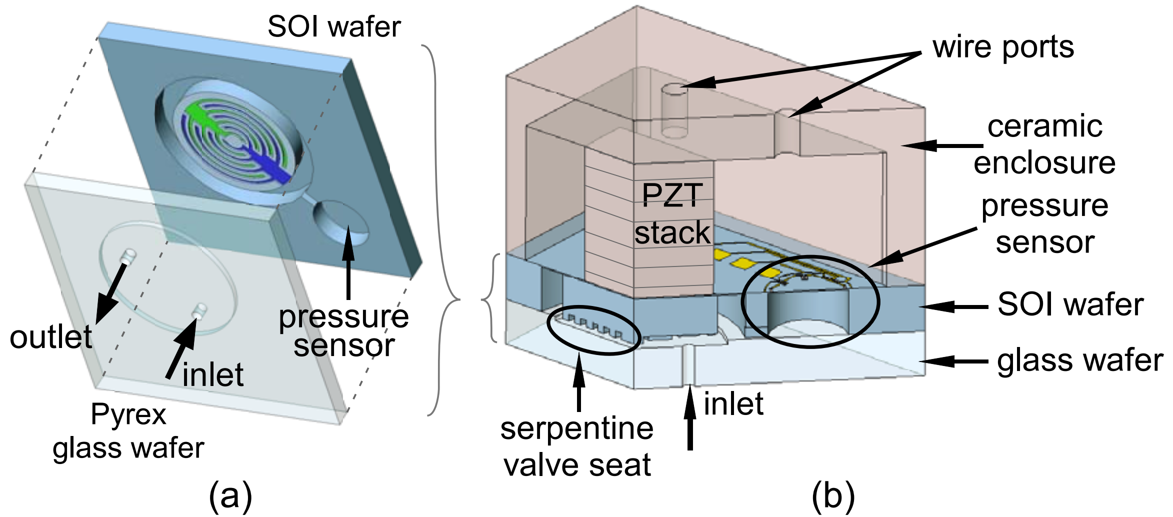

Figure 3.1: Microvalve concepts: (a) A valve plate suspended by a Si membrane with integrated sensors viewed from the bottom. The RTD sensor is located on the backside of the wafer and is not visible. (b) A cut away view of an assembled ceramic-PZT-Si-glass valve structure.

The membrane of the pressure sensor is designed to measure and withstand up to 3 atm of differential pressure. It has four boron doped piezoresistors on a silicon diaphragm, which occupy a surface area of 0.09 mm^2. The resistors have a target sheet resistance of about 2.97×10^3 Ω/□ and a resistance of 26.7 kΩ. As noted previously, the resistors are arranged in a Wheatstone bridge configuration.

A 100 nm thick platinum film is used for the temperature sensor. To achieve approximately 400 Ω of resistance, 20 μm width, 7 mm long thin film platinum is patterned in a serpentine shape on a valve membrane.

3.2 Device Fabrication

The fabrication process is a variant of the process previously used to create flexure suspended microvalves in Chapter 2. Steps have been added to the process to create the embedded sensors, and other steps have been altered to increase yield and decrease process complexity. The valve is fabricated from a silicon-on-insulator (SOI) wafer with layer thicknesses of 50 μm Si, 0.5 μm SiO_2, and 450 μm Si, and a 500 μm thick Pyrex glass wafer. The SOI and glass wafers are independently processed, bonded, and then cut into individual die prior to assembly with the PZT stack, and packaged within the ceramic capsule. The fabrication processes for SOI and glass wafers are illustrated in Figure 3.2.

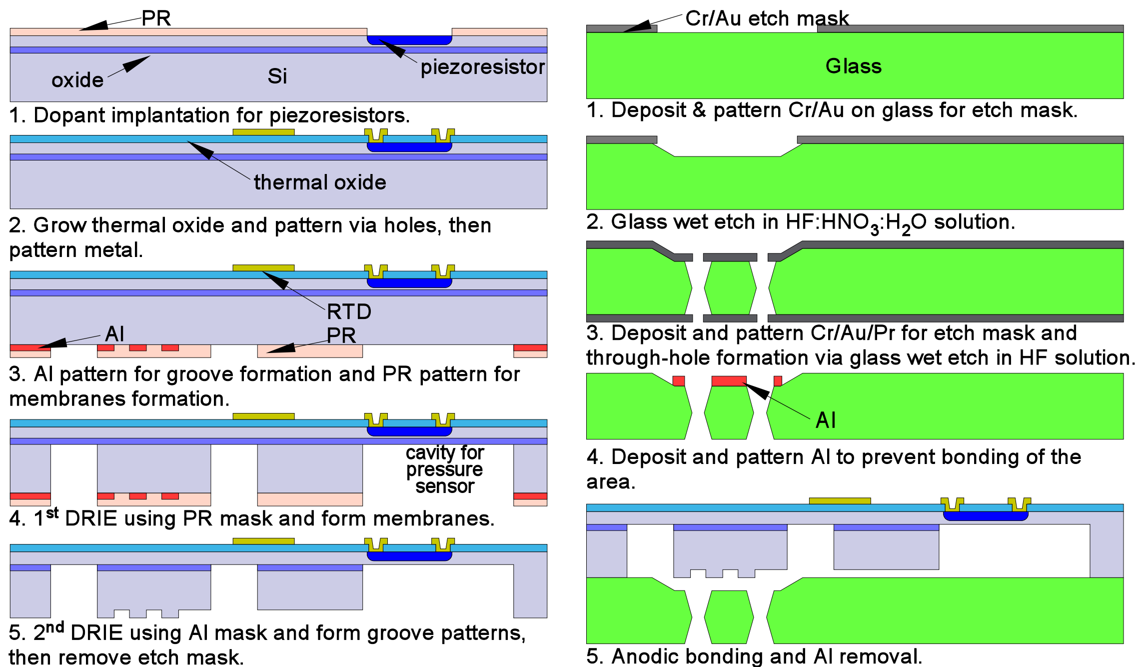

Figure 3.2: Si-glass micromachining process: sensors are formed on the device layer of the SOI wafer by various surface micromachining techniques. Then DRIE is performed to form membrane and groove patterns. A glass wafer undergoes two wet etch steps for a recess and through-hole formation. Next, the two wafers are anodically bonded and diced.

The SOI wafer is initially patterned with photoresist to create the pattern for the piezoresistors. The wafer is then sent to the Innovion Corporation (Chandler, AZ) for

dopant implantation. A boron implantation of 1×10^4 cm^{-2} dose at 10 keV is performed to form piezoresistors. The implantation dose and energy are selected to yield the correct carrier profile after implantation and annealing using the T-SUPREM 4 implantation simulator. A thermal oxide is grown to both provide the necessary isolation and act as the high temperature anneal needed to activate and diffuse the implanted boron. A 2000 Å oxide is grown at 1000 ºC for 50 minutes and the wafer is left at the temperature for an additional 20 minutes in nitrogen environment to allow for enough diffusion time for the implanted boron.

After the thermal oxidation and anneal, vias are etched in the oxide using buffered hydoflouric acid (BHF) to create contacts to the piezoresistors, and a Ti/Pt layer is deposited on the wafers to form the RTD. Lastly, gold is deposited on the contact pads for easier electrical contact with external wiring. Figure 3.3 shows the fabricated die with pressure and temperature sensors.

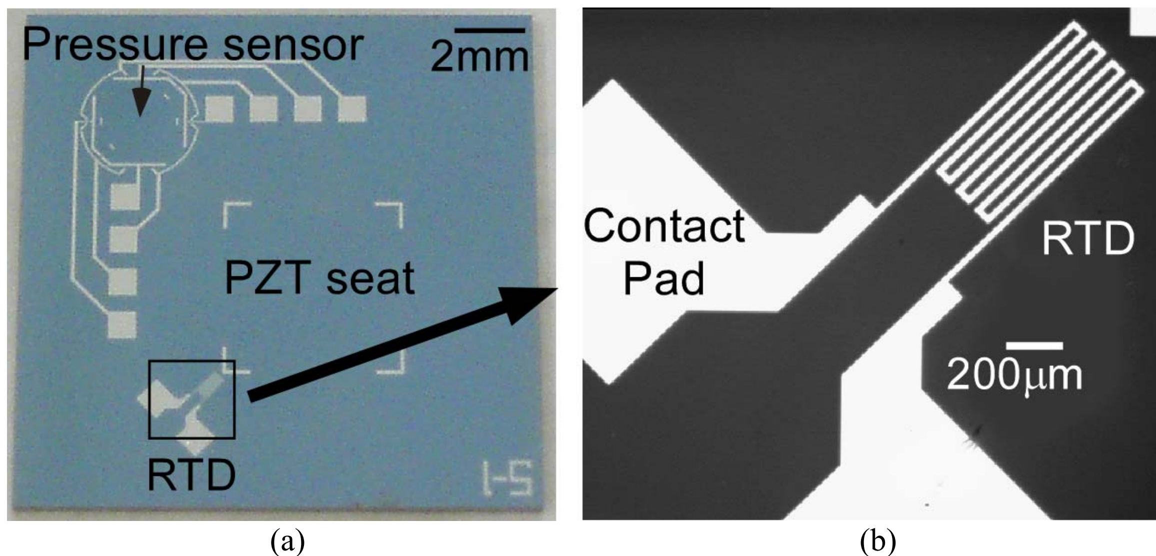

(a) (b)

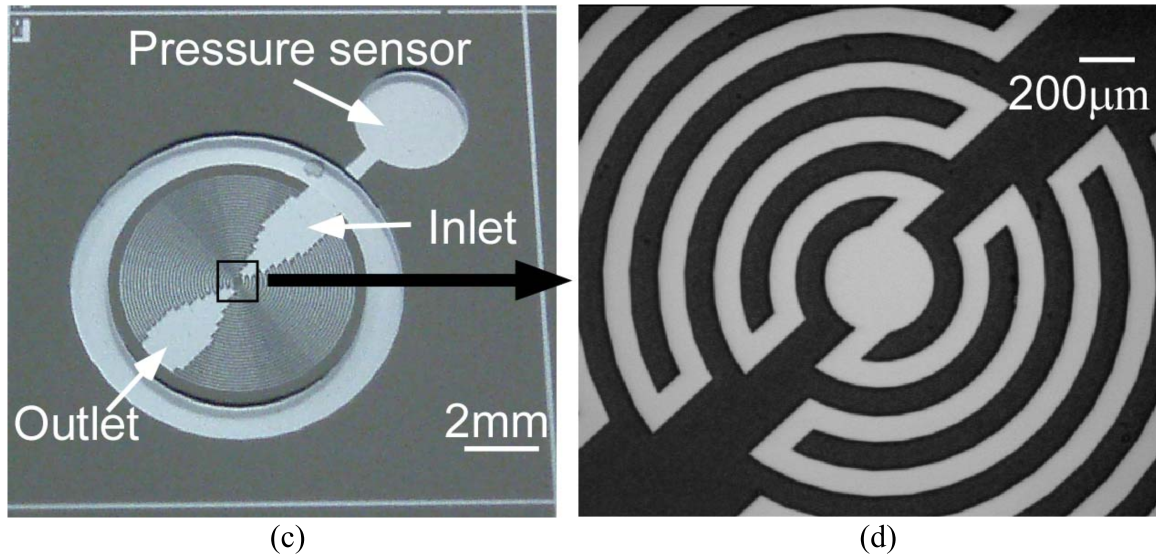

(c) (d)

Figure 3.3: (a) Photograph of the top of the SOI wafer showing the metal contact layer with (b) an expanded view of the platinum RTD. (c) Wide and (d) expanded views of the circular serpentine groove patterns for perimeter augmentation from the bottom of the SOI wafer. This side bonds to the glass wafer.

After the device side is processed, the back side of the wafer undergoes a two-step deep reactive ion etch (DRIE) process to create the pressure sensor diaphragm, the membrane suspension, and the serpentine grooves that increase the flow perimeter. An Al layer is patterned with a lift-off process and photoresist is subsequently patterned on top of the Al Pattern. The photoresist, which covers a region wider than the Al layer does, acts as an etch mask for the first DRIE step that is approximately 400 μm deep. This forms the valve membrane and pressure sensor cavity. Next, the photoresist is removed and Al is used as an etch mask for the final DRIE step, which engraves serpentine grooves for perimeter augmentation. Figure 3.3(c) and (d) show the bottom view of the silicon die after these processes. The resulting grooves are 120 μm in depth and provide seat perimeters longer than 30 cm in length to provide a larger flow area when the valve opens.

A Pyrex glass wafer is first patterned with 2 μm deep, wet-etched recesses, to accommodate the PZT displacement. A brief dip in buffered HF, prior to any process on the glass wafer, helped reduce excessive undercut. The first shallow etch is performed using a Cr/Au/PR mask in diluted HF (H_2O:HF:HNO_3=10:7:3), following which, the mask is stripped.

For the second-generation valves, a wet etching of glass in HF solution is performed, in place of ECDM, to form inlet and outlet holes. The motivation for this change is to enable batch fabrication. Although ECDM is fast in drilling a high-aspect ratio hole in glass, it is a serial process requiring a manual alignment for each hole. When the process wafer contains many holes to be drilled, it could take hours to process just one wafer. In addition, the manual alignment does not always produce consistent results. The wet etching of glass is batch-process and low-cost process, too. However, the wafer is exposed to concentrated HF solution for a long time, thus mask preparation for this step is important. Moreover, wet etching for a long duration causes considerable undercut, so the mask should be designed to accommodate such undercut.

To be used for the wet etching mask, the wafer is patterned again with Cr/Au/PR on both sides and subjected to a through-wafer etch. For a long-lasting mask layer, this time a sputter coater is used for the Cr/Au film to cover the sidewalls and for the thickest film possible. Then AZ 9260 photoresist (15 μm thick) is used for patterning. After using photoresist for patterning the Cr/Au layer, it is then hardbaked in an oven to promote adhesion. Following this procedure, the wafer is placed in 49 % HF to form the through holes for valve inlets and outlets. The SOI wafer and the glass wafer are anodically bonded at 400 ºC, and the wafers are diced to create the final valve die.

After the valve seats are fabricated, electrical connections are made to the sensors, and the devices are assembled with a piezoelectric (PZT) actuator stack and a ceramic Macor cap. The PZT stack is bonded inside the Macor cap using Stycast 2850 FT cryogenic epoxy. Next, the valve is bonded to the PZT stack and the Macor cap using epoxy. The epoxy not only bonds, but also creates a layer compensating for height differences between the actuator and ceramic housing.

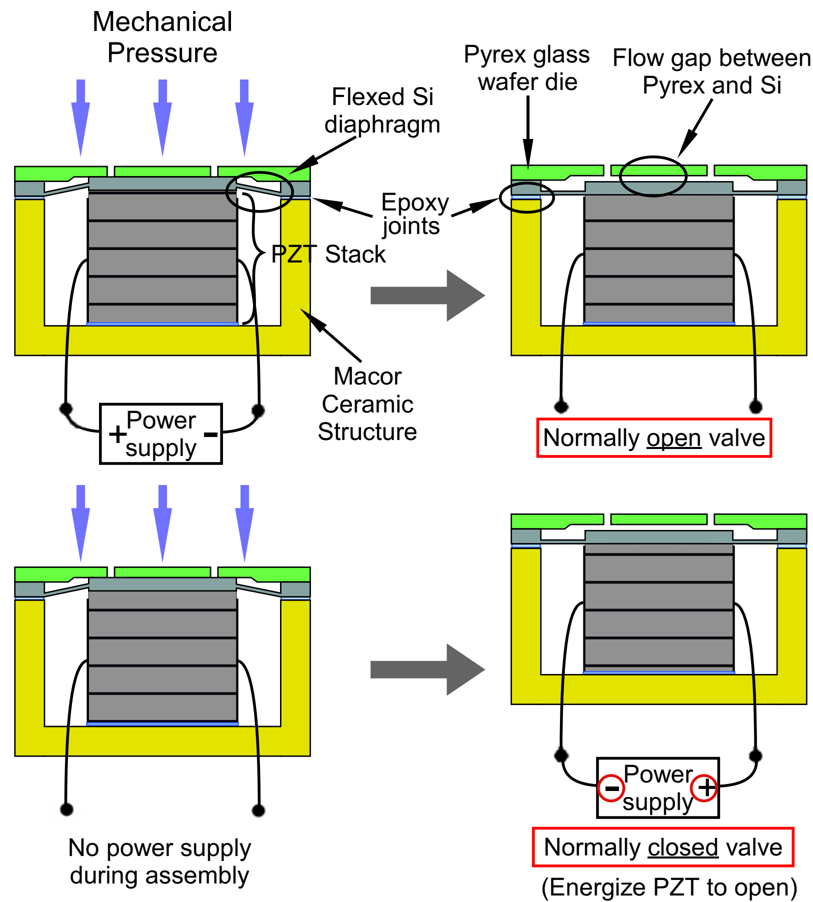

Figure 3.4: The assembly process can be slightly modified to result in either normally-closed or normally-open valves. Energizing the PZT actuator during assembly results in a normally-open configuration (top), while no PZT actuation during assembly yields a normally-closed valve (bottom).

At this stage, the assembly process can be varied to implement a normally-open, partially-open, or normally-closed valve. Figure 3.4 illustrates this process. The general approach is to activate the PZT actuator to the desired closing voltage and then press it

against the valve seat during the assembly process. In other words, to create a normally-open valve, the PZT stack is energized at 100 V during the last assembly step so that it retracts when de-energized after assembly. During operation, the actuation voltage polarity is such that the stack expands. To create a normally-closed valve, a stage is used to press down the valve seat until it comes into contact with the unactuated PZT stack. The voltage produced when the PZT stack is pressurized is a good indication that contact has been made. During operation, the polarity of the voltage is such that the PZT stack retracts. A partially open valve is assembled by using the stage to drive the valve into contact, and then moving the stage away from contact the desired initial gap distance. The final valve structure measures 1.5 x 1.5 x 1.1 cm^3 and is pictured in Figure 3.5.

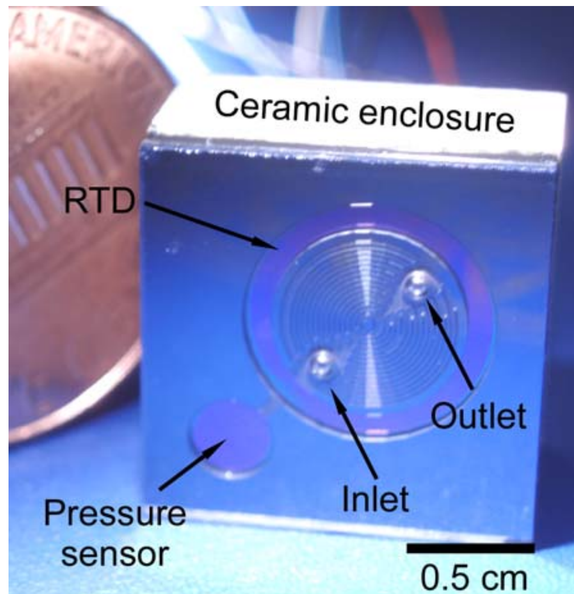

Figure 3.5: An assembled valve looking from the glass side with a US penny. The pressure sensor cavity is connected to the inlet through a passage. The RTD is positioned on the backside of the silicon die.

3.3 Experimental Results

Valve flow tests were conducted on normally-open and normally-closed valves at various pressures and temperatures down to 205 K. The pressure sensor was also tested across varying differential pressures at several temperatures. The embedded RTD was characterized from room temperature down to 50 K.

Normally-open and normally-closed valves were tested at room temperature with N_2 gas flow. The N_2 gas was introduced to the inlet of the valve at the gage pressure of 52 kPa, while the outlet was connected to a flow meter and vented to the atmosphere. The flow rate was measured as the valves were actuated from 0–40 V. In normally-open valves, as the actuation voltage increases, the PZT stack expands to close the gap between the valve seats, decreasing the flow rate (Figure 3.6a). The flow rate changed from 200 mL/min at the open state (0 V), down to below the measurement limit (< 1 mL/min) at the closed state (40 V). The normally-closed valve works by retraction of PZT when a reverse polarity voltage is applied. Therefore, the gap between the valve seats increases with the voltage, resulting in an increase in flow rate. However, the displacement is typically smaller than when the same voltage is applied in the expansion mode. This results in lower flow rates than the normally open valve. This is illustrated in Figure 3.6b with a curve in the opposite direction compared to that of Figure 3.6a, and presents maximum flow rate of 115 mL/min at 40 V actuation. The hysteresis due to the piezoelectric actuator can be seen in the flow rate variations for various set voltages.

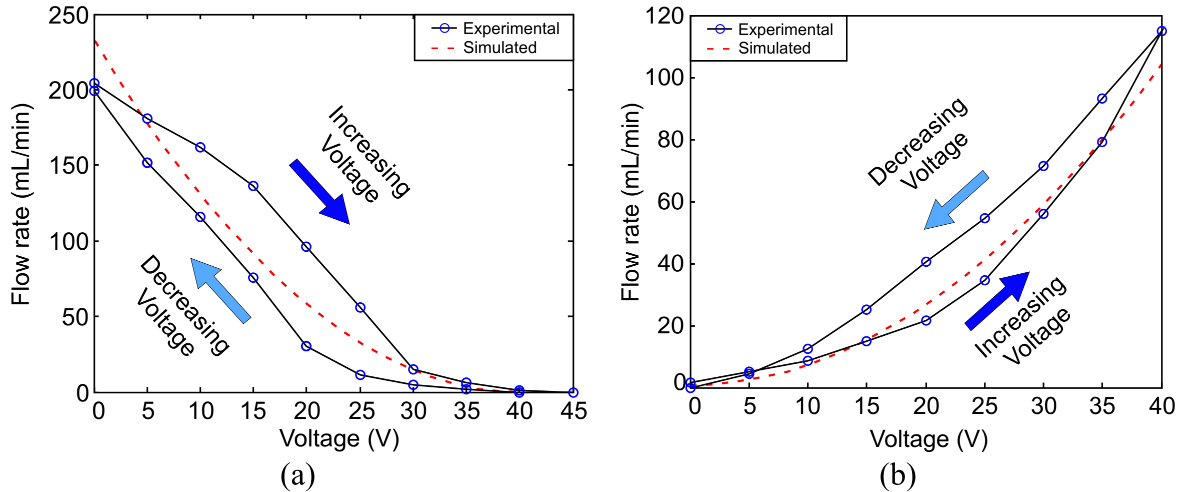

Figure 3.6: Flow rates as a function of actuation voltage measured at room temperature. Flow measurements of (a) normally-open valve, and (b) normally-closed valve measured at a differential inlet pressure of 52 kPa.

A numerical model is presented with experimental results in Figure 3.6, and shows good agreement. The model does not account for hysteretic behavior of PZT and assumes displacement is linearly proportional to the actuation voltage, and generally goes through the middle of the hysteresis curve. Uncertainties in actuator displacement and inlet and outlet hole size are responsible for discrepancies between the model and actual measurements.

The normally-open valves were tested over a range of temperatures. The tests were conducted using He gas, and both the gas and the valve were cooled with a Cryomech AL60 GM cryocooler while the differential pressure was regulated at 34 kPa with an inlet pressure of 160 kPa. Figure 3.7 represents the results by lines through the average value of hysteresis, while the hysteresis is represented as error bars. As temperature decreases, actuation of PZT has a lesser effect on flow modulation, resulting in a higher flow rate at a given actuation voltage. When the valve is open (0 V), the flow rate remains consistent at around 300 mL/min, but at 120 V actuation, the flow rate increases from 95 mL/min at 263 K to 255 mL/min at 205 K.

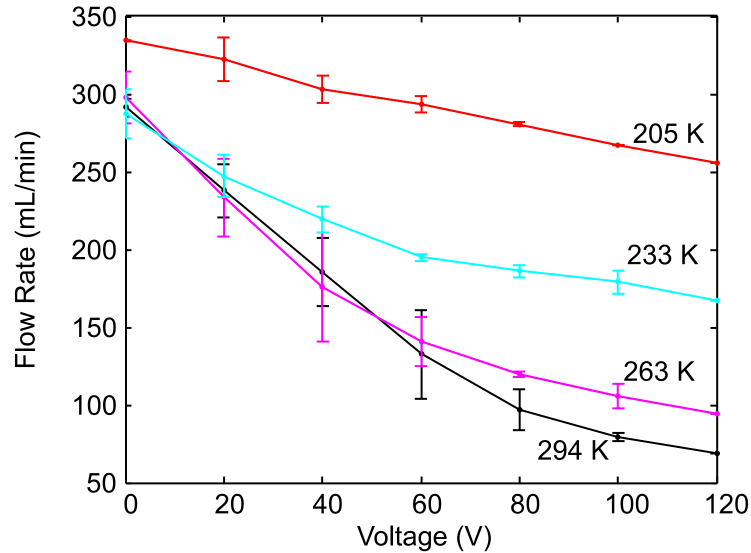

Figure 3.7: Flow characteristic of a normally-open valve at different temperatures. The measurement was made at 34 kPa differential pressure with 160 kPa absolute inlet pressure. As the temperature decreases, actuation of the PZT has a lesser effect on flow modulation, thus resulting in a higher flow rate at a given actuation voltage. This is mainly due to a degraded piezoelectric performance at lower temperatures. Hysteresis of the PZT actuation is represented as error bars here.

Embedded pressure sensors were tested at various temperatures as the differential pressure across the valve was varied from 0 kPa up to above 100 kPa (Figure 3.8). The pressure sensors were powered at 5 V as the differential output voltage was monitored. The linearity of the pressure sensor remains within ± 0.5% across the range of pressure and temperature (206 - 295 K) tested. The slope of the line, which represents sensitivity of the sensor, increases from 356 to 563 ppm/kPa, and the zero-pressure offset voltage decreases from 95 to −195 mV, as temperature decreases from 295 to 205 K.

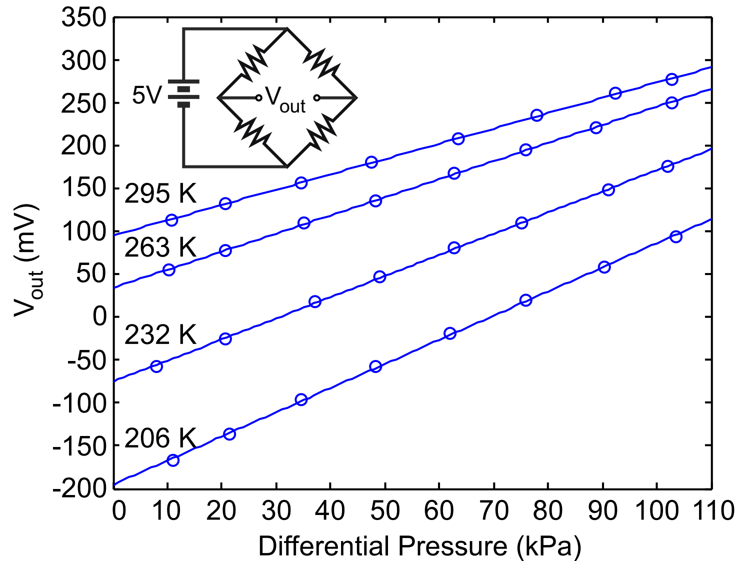

Figure 3.8: Output voltage from the piezoresistive pressure sensor at various differential pressures and temperature. The linearity of the pressure sensor was still good at low temperatures; however, the offset voltage and sensitivity of the sensor changes with varying temperatures.

For characterization of the temperature sensor, the Pt RTD resistance was measured using a 4-point method as the valve is cooled down to 50 K. A silicon diode cryogenic temperature sensor (Lake Shore Cryotronics, Inc.) was used as the temperature reference. Two different sets of measurements are plotted in Figure 3.9. Figure 3.9a represents the resistance measurements of RTD on bulk silicon, with no membrane structures and ceramic enclosure, while Figure 3.9b corresponds to the measurements of RTD integrated with a fully packaged device. In both cases, the RTD response is very linear in temperatures above 150 K with the linearity error within ±0.6 %. On bulk silicon the RTD showed sensitivity of 0.23 %/K and in the packaged device the sensitivity was 0.29 %/K. The two RTDs show different trends in the temperatures below 150 K.

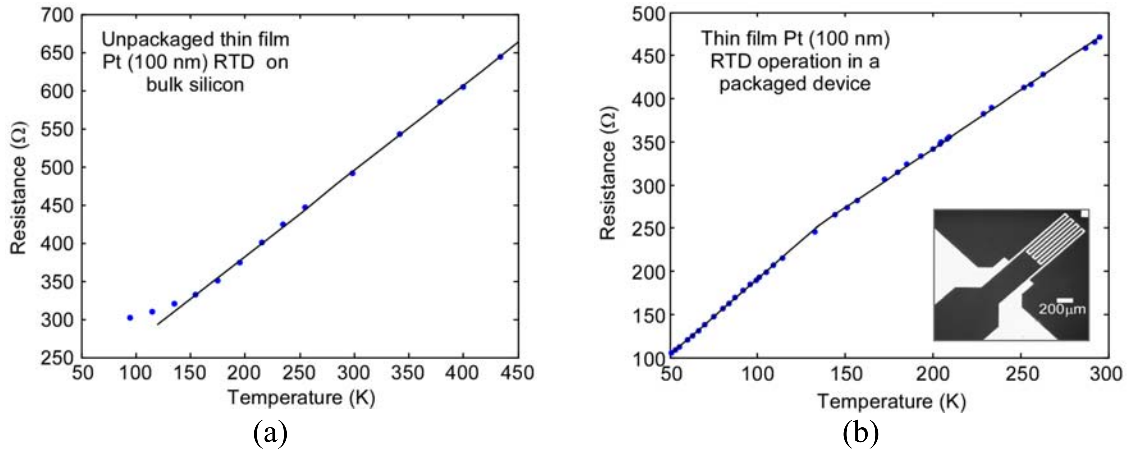

(a) (b)

Figure 3.9: Measured RTD resistance versus temperature change with best fit lines (a) on bulk silicon, and (b) in a packaged device. The RTD shows bilinear behavior, with a sensitivity of 0.29 %/K above 140k and 0.37 %/K below it.

3.4 Discussion

3.4.1 Flow Measurements

In the flow modulation test, as presented in Figure 3.7, as the temperature decreases, the PZT actuation has a decreased effect on flow rate modulation. This is mainly due to a degradation of the PZT stack that occurs because of the decreased piezoelectric constant at lower temperatures [72]. The piezoelectric constant is reduced by about 25 % over the range of temperature tested. The actuation is further diminished by the stiffness of the valve membrane (3.8×10^6 N/m), which requires significant force during assembly to achieve a good seal when the valve is closed, which in turn results in a reduced range of piezoelectric actuator displacement and range of flow modulation. A more compliant membrane structure, such as a corrugated membrane, may help improve the valve performance with added complexity in the fabrication process. Change in stress on the valve membrane, due to thermal expansion mismatch between PZT actuator and Macor housing, can also have an effect on flow modulation.

3.4.2 Pressure Sensor Measurements

The behavior of the piezoresistive pressure sensor at different operating temperatures exhibits interesting trends. The slope of the plot (sensitivity) and zero-pressure offset voltage changes with the temperature. The changes in sensitivity and offset voltage against temperature are plotted separately in Figure 3.10 to illustrate this behavior.

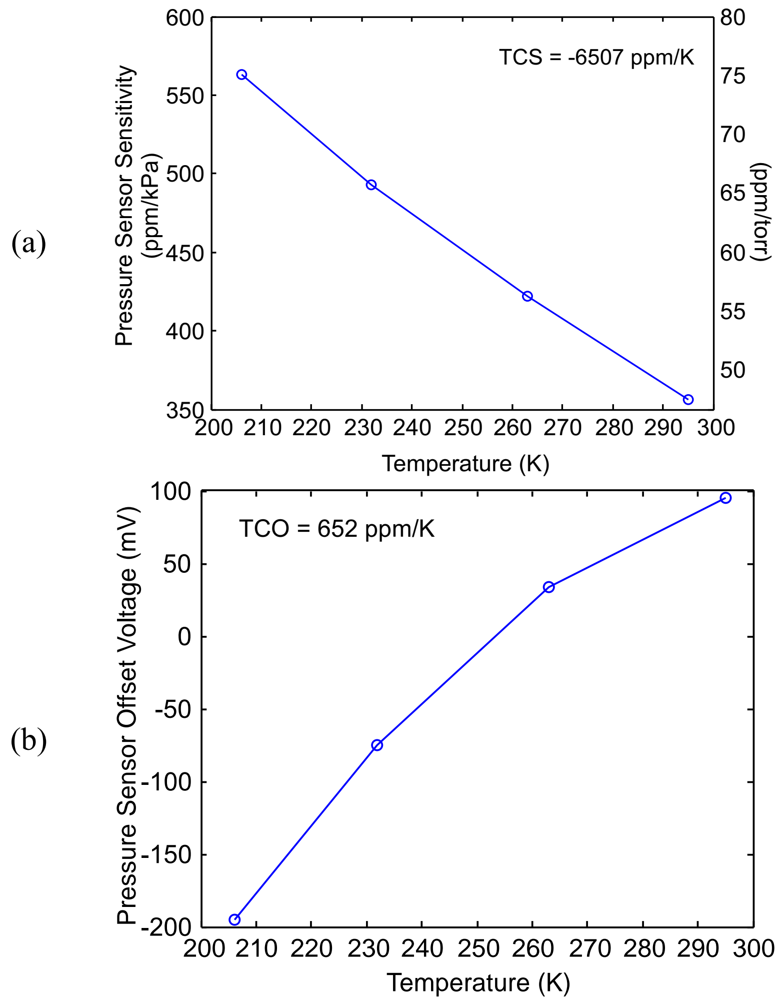

Figure 3.10: The effect of temperature on the piezoresistive pressure sensor. (a) The measured sensitivity of the pressure sensor decreases with increasing temperature with 356 ppm/kPa at room temperature. The sensitivity is plotted in both ppm/kPa and ppm/torr. The behavior is dominated by the temperature dependency of the piezoresistance factor. (b) Measured offset voltage also changes with temperature due to thermally induced stress on the membrane.

The sensitivity of the pressure sensor decreases with increasing temperature from 56 ppm/kPa at 206 K to 356 ppm/kPa at room temperature (Figure 3.10a). The Temperature Coefficient of the pressure Sensitivity (TCS) is defined as,

$$TCS = \frac{1}{S}\frac{\delta S}{\delta T} \tag{3.1}$$

where S is sensitivity and T is temperature, and measures how much sensitivity changes with temperature. In our case, the TCS is −6507 ppm/K over the range of temperature tested, referenced to the sensitivity at room temperature. This behavior is almost entirely dominated by the temperature coefficient of the piezoresistive coefficient [87]. As presented in Kanda [88], the piezoresistive coefficient is a function of impurity concentration and temperature, but for a given impurity concentration, the coefficient increases about 50 % while temperature decreases from 298 K (25 ºC) to 198 K (−75 ºC). This corresponds well with the data shown in Figure 3.10(a).

The offset voltage also changes as temperature reduces. An initial offset is introduced due to mismatched resistors. In our design of piezoresistors, the resistors transverse to the crystallographic axes are split into two segments and connected with metal lines to allow them to be placed close to the rim, while longitudinal resistors are a one-segment design. This geometric difference between transverse and longitudinal resistors can contribute to the mismatch in resistor values. The temperature effects on an individual resistor can be represented as

$$\Delta R = R_{T0}\alpha_R \Delta T + \Delta R\left(\pi(T), \sigma(T)\right) \tag{3.2}$$

where R_{T0} is resistance at the reference temperature, α_R is the temperature coefficient of resistance, and the last term describes the change of resistance due to temperature

induced stress on the membrane [89]. The Temperature Coefficient of Offset (TCO) is defined as

$$TCO = \frac{1}{V_{cc}} \frac{\delta V_o}{\delta T} \tag{3.3}$$

where V_{cc} is supply voltage and V_o is the output voltage when no pressure differential is applied [87]. The typical TCO is 652 ppm/K over the temperature range tested. The temperature sensitivity of a piezoresistive pressure sensor is well known and several compensation techniques exist [90-93]. However, in this particular application, since a temperature sensor is monolithically integrated with the valve and pressure sensor, it can be used to computationally correct the output.

3.4.3 RTD Measurements

The platinum RTDs show good linearity in temperatures above 150 K. However, two different trends are observed for an unpackaged RTD on bulk silicon and for the RTD integrated within a packaged device. For the former case, lead transfer is performed by wire bonding, and a bead of epoxy is applied on top of the wire bonds for increased structural integrity. However, it is suspected that the epoxy alters the resistivity of the wire due to the thermal stress caused by large temperature difference and results in a decrease in sensitivity at low temperatures. For the measurement in a packaged device, a thicker wire is soldered on the contact pad and a bead of epoxy is applied on top of it. This ensures a good contact down to 50 K. In this case the measurement shows an apparent bilinear behavior with a sensitivity of 0.29 %/K above 140K and 0.37 %/K below it.

3.4.4 Stress Effects

As devices are subjected to a very wide range of temperatures, thermal stress can be developed by different Coefficient of Thermal Expansion (CTE) of different materials and cause abnormalities in certain measurements. For example, thin film platinum is known to be strain-sensitive, and in the presence of strain, the temperature sensitivity of thin film platinum is different to that of bulk platinum [94]. Although the CTE of Pyrex is well matched to that of Si in the 300–675 K range, at which temperature anodic bonding takes place [95], the CTE of Si substantially decreases at low temperatures and turns to a negative value below 140 K [96], while Pyrex maintains a CTE of 1.1 ppm/K even at 100 K [97] (Figure 3.11). This imposes a compressive stress on the silicon membrane. A steep change in CTE of Pt at low temperature, and thermal mismatch between the Si substrate and the thin film Pt, may also play a role in the temperature sensitivity of the RTD. Addition of Macor housing material to these further complicates the problem. A more detailed study of stress-temperature relationship, while desirable, is beyond the scope of this research. Although our temperature sensor exhibits some variation compared with standard platinum RTDs, which provide linear response down to 70 K [85], the phenomenon is repeatable and once calibrated, it is expected that the device can provide accurate temperature readings.

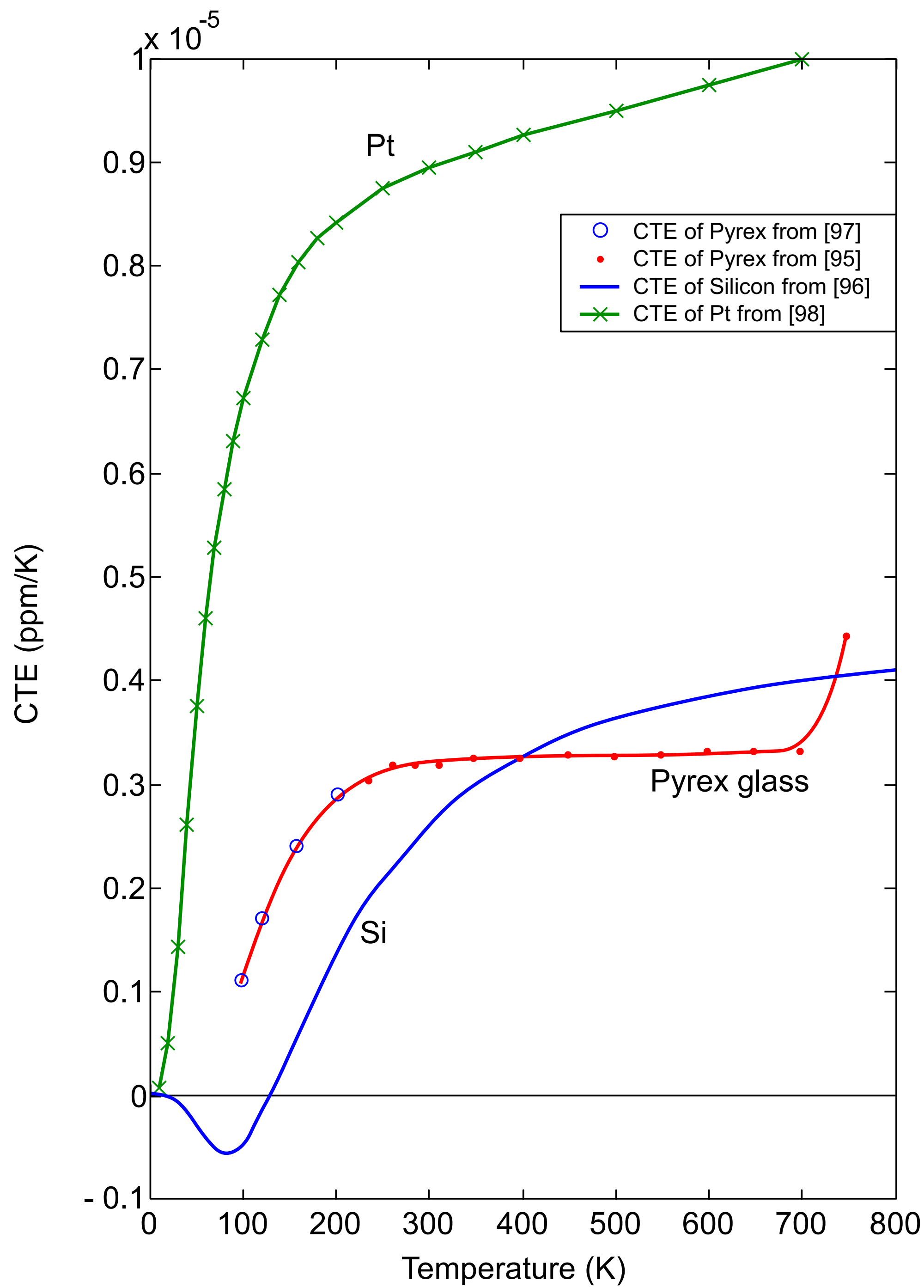

Figure 3.11: Comparison of the coefficient of thermal expansion of Pt, Pyrex glass, and silicon.

3.5 Conclusions

This effort has resulted in the successful fabrication of a suspended-membrane piezoelectrically-actuated ceramic-Si-glass microvalve with embedded sensors for use in distributed cooling applications. A perimeter augmentation scheme was used to overcome the limited displacement of PZT and provide large flow modulation. An assembly process was developed to allow for the creation of normally-open, partially-open, and normally-closed valves. Both a normally-open and normally-closed valve were tested at room temperature, and allowed flow rates of up to 200 mL/min and 100 mL/min of N_2 at a differential pressure of 52 kPa. A normally-open valve was tested at lower temperatures to below 200 K, and demonstrated the ability to modulate the flow over a wide range of temperatures. However, decreased flow modulation was observed due to the degraded actuation of the PZT stack. The stiff membrane suspension also contributes to the limited range of flow modulation.

Sensors were embedded with the valve to provide the necessary information for closed loop control of the valve. Piezoresistive pressure sensors were designed using implanted boron on a silicon diaphragm. The pressure sensor had a sensitivity of 356 ppm/kPa at room temperature, and the sensitivity increased with decreasing temperature, primarily due to change in the piezoresistive coefficient with temperature. The pressure sensor also exhibited temperature dependent offset voltage drift, primarily resulting from thermally induced stress on the membrane.

An RTD temperature sensor was fabricated using platinum on the backside of the fluidic channel. The temperature sensor exhibited the expected bilinear behavior of RTDs and had a sensitivity of 0.29 %/K above 140 K and 0.37 %/K below as it was

tested down to 50 K. The RTD functions robustly down to cryogenic temperatures and should provide valuable information for feedback control and accurate calibration of the pressure sensor.

It is worth noting, the valve can be scaled up or down according to the desired flow rate; this can be done by changing the valve plate area or PZT stack height to allow for lower or higher flow rates. Additionally, specific un-powered flow rates can be set by assembling the valve with a nominal gap, meeting application needs. Because the valve uses a membrane support structure with no electrical conduction across the flow path, it can be used for liquid flow modulation in various microfluidic applications [99,100]. In addition, the valve can be deployed to operate in harsh environments, due to the ability to work across a wide range of temperatures and ceramic encapsulation.

CHAPTER 4

VALVE APPLICATIONS

In the preceding chapters, the development and testing of the microvalve was described. In this chapter, the use of the valve in two different applications is evaluated and presented: a drug delivery system[1] and a Joule-Thomson cooling system[2]. Even though the valve was developed for distributed cooling systems to be used in space, the compact size, low power consumption, and compatibility with liquid flow, made it very attractive for its application in implantable drug delivery devices. An overview of the drug delivery system and liquid flow control results is presented in section 4.1. For the cooling test, a micromachined recuperative heat exchanger is used with the valve, while the valve acts as an expansion device. A brief description of the heat exchanger, experimental procedure, and cooling test results are described in section 4.2.

4.1 Liquid Flow Modulation

The bio-compatibility of silicon and glass with ceramic construction, and the low power consumption and compact design of the valve make it attractive for biomedical

[1] The work was done in close collaboration with Allan Evans [98,99]
[2] The experimental testing of the Joule Thomson system was primarily conducted by Weibin Zhu [100,101]

applications, especially because the valve can modulate liquid. This led us to develop a low-power, implantable drug delivery system using the microvalve.

4.1.1 System Overview

Many individuals require frequent drug treatment for pain management for medical conditions ranging from diabetes to cancer. Recent advances in implantable reservoirs, pumps, and drug delivery devices have greatly assisted in drug management from insulin for diabetics and pain-relieving drugs for terminal cancer patients. These drug delivery devices can be generally categorized into two main types: a passive device utilizing polymer implants or pressurized fluid reservoirs, which do not require any power, and an active device, requiring an active pump. The passive devices usually allow for a single delivery rate and are unable to respond to changes according to patients' needs. Active devices generally use pumps to deliver medications in a controlled manner with the ability to vary the rate, but at the expense of increased size and weight for the battery. Power consumption is critical for an implanted device as one can refill the aqueous medication but cannot recharge or replace the battery. Additionally, the power consumption increases with delivery rate, as the pumps need to work harder.

If an active power-efficient valve can modulate the delivery rate with the use of a pressurized reservoir, the delivery rate can be adjusted, and little battery power is required. Our active microvalve, utilizing a PZT actuator, provides a good solution for such application as it requires minimal power for DC or low frequency operation. The concept of the proposed system is shown schematically in Figure 4.1.

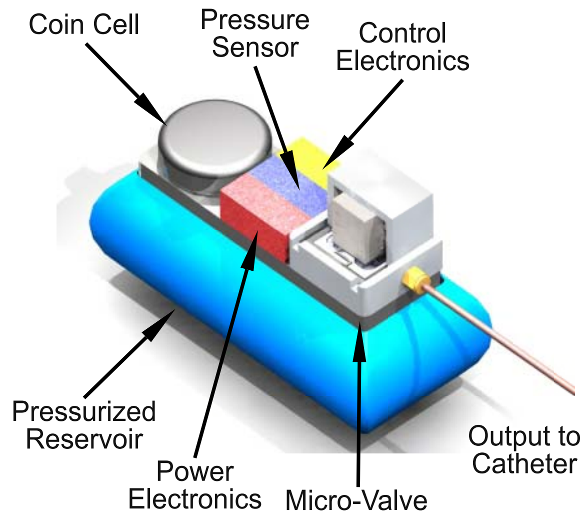

Figure 4.1: Proposed system schematic of the microvalve controlled portable drug delivery system.

4.1.2. Microvalve Liquid Flow Tests

A normally-open microvalve was used to modulate liquid from the pressurized source. To simulate a pressurized reservoir, a reservoir was filled with a liquid and connected to the inlet of the valve while the other end of the reservoir was connected to pressurized nitrogen. The outlet of the valve was left open to the atmosphere to create a pressure difference. Flow rates were determined from precisely measuring the mass changes measured over time. In the first test, the liquid flow rates were measured as the differential pressure was varied from 16-47 kPa through un-actuated valve (Figure 4.2).

The flow rate changed from 250 to 460 µl/min with the change of pressure. At low pressures, the flow rate changes almost linearly with pressure. The linearity of the slope suggests that the hydraulic resistance of the valve remains the same for the particular actuation voltage.

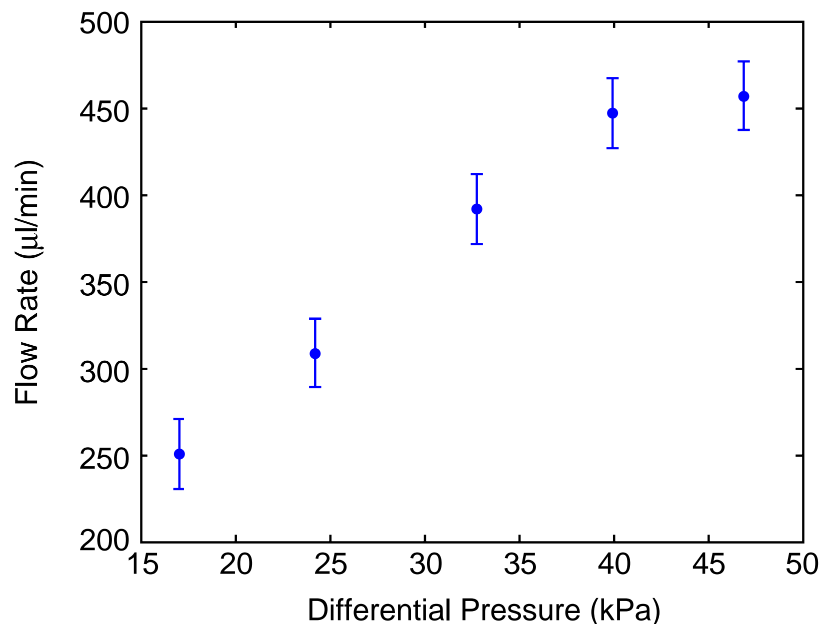

Figure 4.2: Flow rate through un-actuated valve (0 V) across various pressures. At low pressure the flow rate changes almost linearly with pressure (Allan Evans [99]).

Flow modulation was investigated by varying actuation voltage. An increasing voltage was applied while maintaining the inlet pressure. Results at 108 kPa and 142 kPa are shown in Figure 4.3. As voltage applied to the valve increases, the hydraulic resistance increases accordingly, decreasing the flow rate. Modulation in flow rate is more pronounced at a higher inlet pressure.

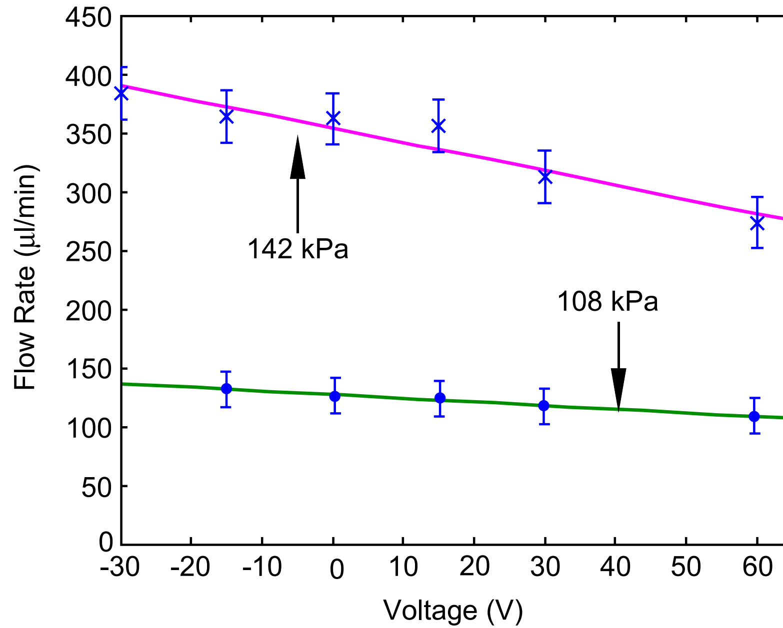

Figure 4.3: Flow rate changes as a function of actuation voltage shown at two different inlet pressure values (Allan Evans [99]).

Additional tests were conducted by observing diffusion. It is important to verify the active control over diffusion because medication enters the patient's system by diffusion into tissues. The results indicate the valve can be used to achieve active control over diffusion and the proposed system could provide a promising drug delivery device [99].

4.2 Joule-Thomson Cooling System Test

4.2.1 Joule-Thomson Effect

When a fluid passes through a restriction such as a valve or an orifice, without sufficient time and area for effective heat transfer, the pressure of the fluid drops while enthalpy remains unchanged (isenthalpic process). The change in temperature experienced by this process is called the Joule-Thomson effect. Joule-Thomson (JT) coolers have been widely used for cooling optoelectronic devices and for cryogenic applications due to simple construction and compact design. The basic components of a JT cooler operating in a closed cycle is shown in Figure 4.4 with a corresponding temperature-entropy diagram. Often a compressor is used to compress the working fluid to high pressure. The high-pressure gas enters the recuperative (counter-flow) heat exchanger (1) and is pre-cooled by the low-temperature, low-pressure gas (2). The high-pressure gas then expands through an expansion device (valve or orifice), which achieves further decrease in temperature (3). At this point, the working fluid absorbs the heat load (4) and also cools the incoming gas as it passes through the recuperative heat exchanger again (5). The low-pressure gas returns to the compressor and completes the cycle.

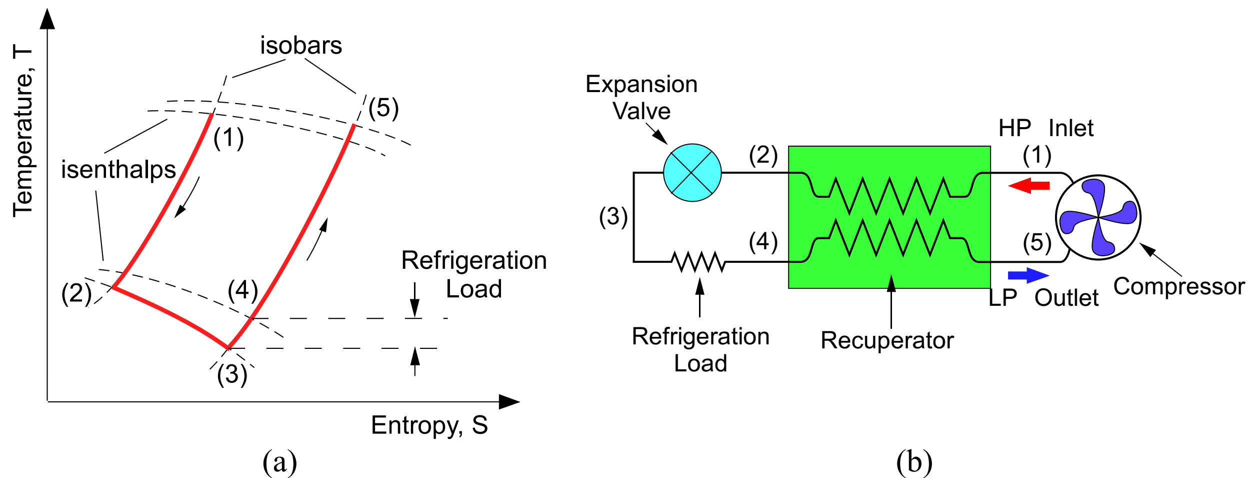

Figure 4.4: (a) Temperature-entropy diagram and (b) basic components of a JT cooler equipped with a recuperative heat exchanger.

A recuperative heat exchanger and expansion device are integral components in the cooling system. A MEMS heat exchanger developed for a cryosurgical probe and a microvalve are tested together to demonstrate their cooling performance. Conventional cryosurgical probes have a fixed orifice size. However, the use of an actively controlled microvalve would allow changes in effective orifice size to optimize the cycle in response to heat load requirements. For space applications, when multiple IR sensors are on board, the microvalves can route the coolant to specific devices, intended for use at the time. This can eliminate the need for loading multiple compressors on a spacecraft, resulting in tremendous savings on launch cost. In addition, the Joule-Thomson expansion through the valve can compensate for any parasitic heat gained as it travels through its path.

4.2.2 Microvalve Test

The microvalve is first tested separately to characterize its behavior using ethane as a working fluid. The valve is actuated from -30 V to 100 V while inlet (450 kPa) and outlet (221 kPa) pressures are held constant. The flow modulation behavior is shown in

Figure 4.5. At a 230 kPa pressure difference, the valve can modulate flow from 3750 mL/min to 2500 mL/min. The figure shows the usual hysteresis curve for piezoelectric actuation.

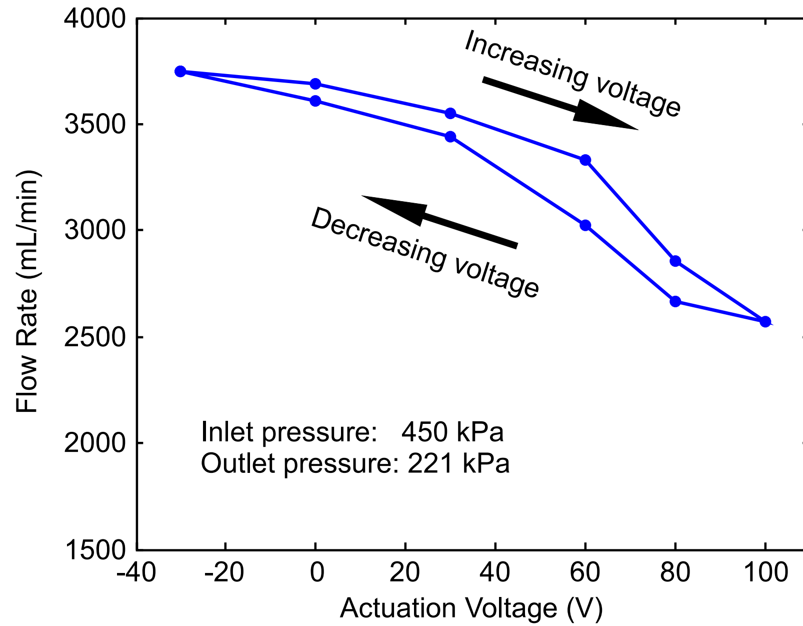

Figure 4.5: Plot of flow rate as a function of actuation voltage while inlet and outlet pressures are held constant.

To determine the effective orifice diameter of the microvalve, the flow rate through the valve is compared with calculated flow rates through fixed jewel orifices, and is plotted in Figure 4.6. According to the figure, the effective orifice diameter of the valve ranges approximately from 0.009" when it is actuated at 100 V and 0.011" when the voltage is at -30 V. A predicted flow modulation capability of this particular valve is shaded in yellow.

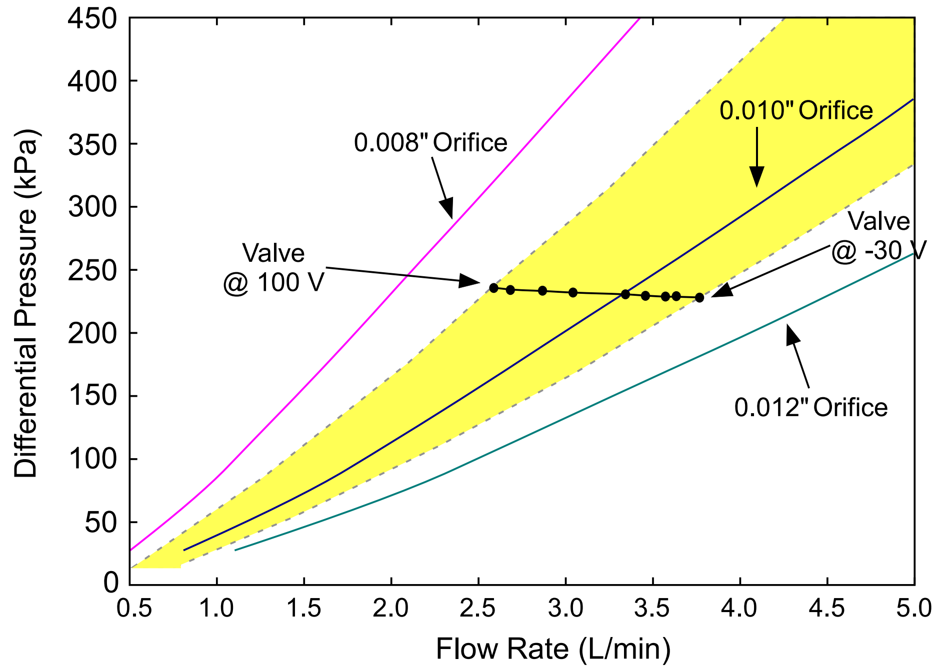

Figure 4.6: The data in Figure 4.5 is re-plotted with expected flow rates through a jewel orifice. The differential pressure is maintained at 229 kPa.

The valve is tested at a broader pressure range with different actuation voltages and the measured flow rates are plotted in Figure 4.7 along with measured flow rates from 0.015” and 0.010” orifices to compare the flow rates. It is worth noting that the valve can modulate the flow rate even at a larger than 450 kPa pressure difference. The yellow region represents the flow modulation capability of the valve. On the right side of the yellow region is the flow rate measured with -30 V and on the left side is the flow rate with100 V actuation. At the pressure difference of 450 kPa, the flow rate can be modulated from 5 L/min to 2.5 L/min.

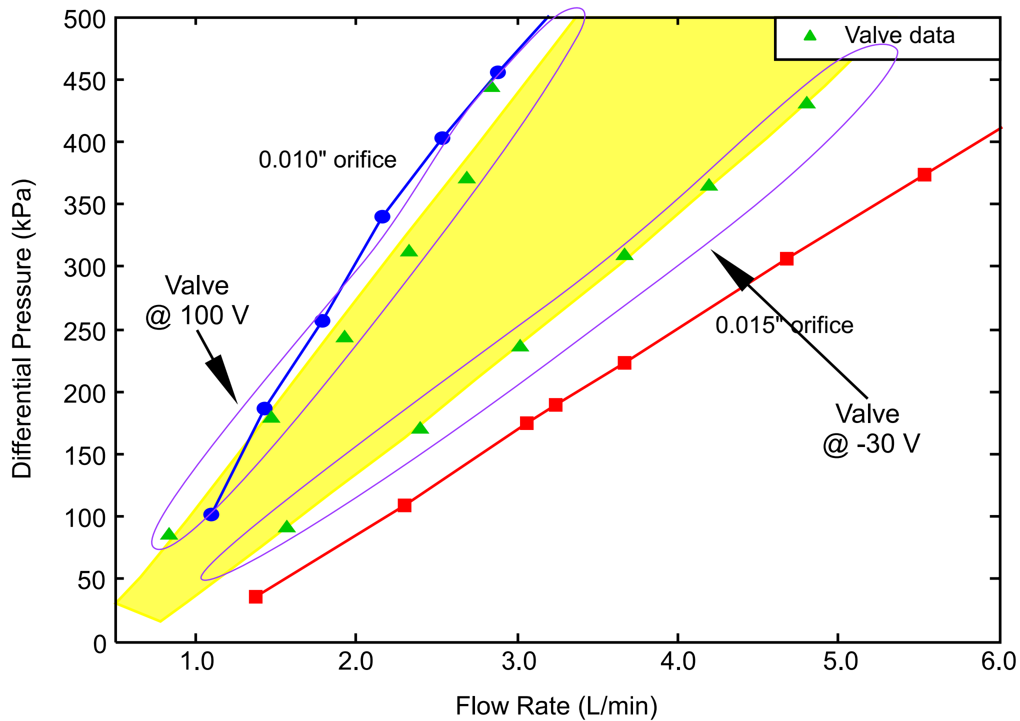

Figure 4.7: Flow rates of a microvalve at various differential pressures compared with measured flow rates using 0.015" and 0.010" orifices.

4.2.3 MEMS Heat Exchanger

For an effective cooling cycle, the heat exchanger must maintain good stream-to-stream heat conductance between the high and low-pressure channels while restricting stream-wise conduction. In a micro recuperating heat exchanger design, this is achieved by using silicon and borosilicate glass, which are materials differing vastly in thermal conductance (148 W/m·K and 1.00 W/m·K, respectively), yet compatible with micromachining. The structure consists of high-conductivity silicon plates alternating with low-conductivity glass spacers. A schematic of the perforated plate heat exchanger is shown in Figure 4.8.

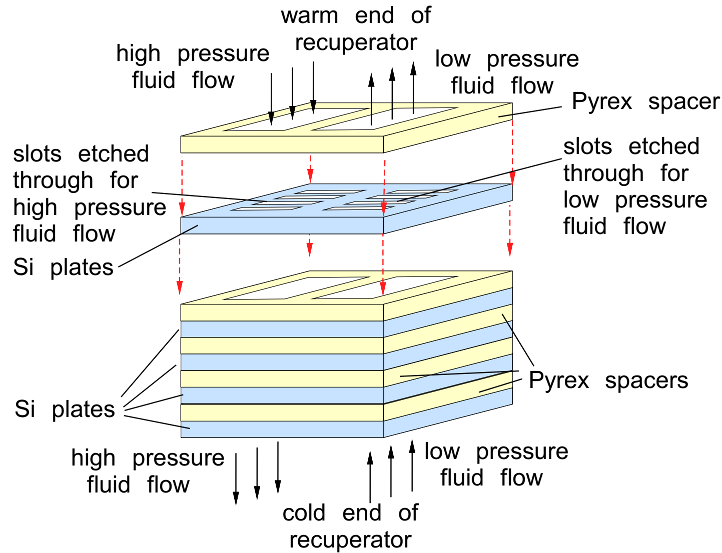

Figure 4.8: Schematic of a perforated plate recuperative micro heat exchanger (Weibin Zhu [102]).

A die consists of one silicon perforated plate bonded to one glass spacer. Narrow perforations are etched into the silicon plate to provide a large surface area for the heat exchanger and each plate is divided into two regions by a glass spacer. Each die has outer dimensions of 10 mm by 10 mm and has a thickness of 0.8 mm (0.5 mm silicon plate and 0.3 mm glass spacer). For each stream, there are 74 flow passages, each having a length of 1.4 mm and a width of 0.05 mm. The heat is transferred from the high-pressure fluid to the low-pressure fluid through the silicon plates, while glass spacers isolate stream-wise heat conduction. Heat exchangers are fabricated by bonding individual dies together to form a stack. Integrated platinum RTDs are utilized to monitor the internal temperature distribution of the heat exchanger.

First, the heat exchanger and microvalve are tested independently to characterize their performance, and then the microvalve is used to modulate the cooling provided by the heat exchanger.

4.2.4 Heat exchanger self cooling test

A forty-three die heat exchanger is assembled by the dies using epoxy. The heat exchanger is then mounted on stainless steel headers for testing purposes. For the self-cooling test of the heat exchanger, employing a JT cycle, an isenthalpic pressure drop is created by placing a precision jewel orifice or a microvalve between the high-pressure outlet and the low-pressure inlet as schematically illustrated in Figure 4.9. The test is conducted with ethane as the working fluid and cold end temperature is monitored while varying the inlet pressure. Three orifice diameter sizes, 0.010", 0.015", and 0.020", are used, and for each orifice size the temperature difference as a function of pressure difference is plotted in Figure 4.10.

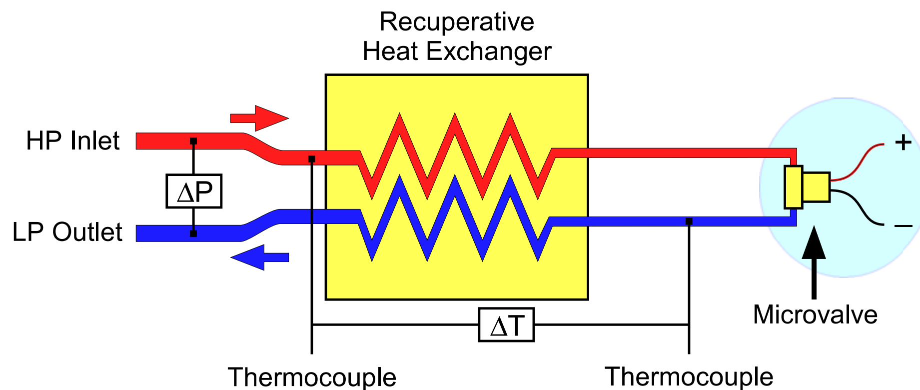

Figure 4.9: Schematic of the self-cooling test setup of the forty-three die heat exchanger. The test is conducted using ethane as a working fluid. Jewel orifices can be used in place of the microvalve. The pressure differential between the inlet and outlet of the heat exchanger and temperature difference between the inlet of the heat exchanger and outlet of the valve are measured.

As shown in the figure, the performance of the heat exchanger differs with different orifice sizes. For a 0.010" size orifice, the temperature difference of 41 K is achieved with a differential pressure of 455 kPa. With a 0.015" orifice, a larger temperature difference across all differential pressure ranges is achieved with the largest temperature difference of 43 K. When orifice size is further increased to 0.020", at lower pressure differences, a slightly lower temperature is reached at lower pressure differences,

while getting higher cold-end temperatures for larger pressure differences. This indicates the existence of an optimal orifice opening for certain conditions (heat exchanger geometry, pressure difference, etc), and employment of a microvalve can provide a way to fine-tune the expansion process.

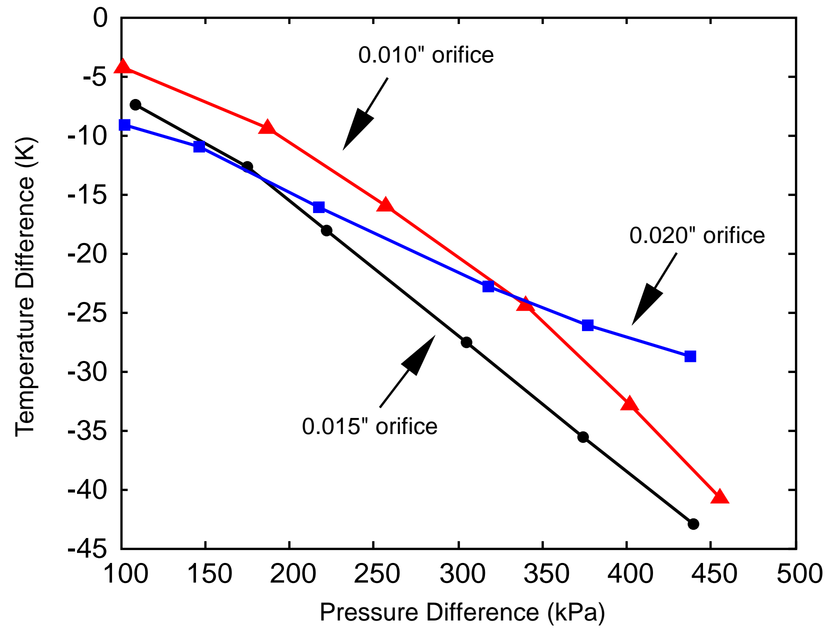

Figure 4.10: Temperature difference between the heat exchanger inlet streams as a function of pressure difference applied across the forty-three die heat exchanger assembly. The optimal orifice size is 0.015" (Weibin Zhu [103]).

4.2.5 Self Cooling Test with Heat Exchanger and Valve

Finally, the valve is connected with a forty-three die heat exchanger and a self-cooling test is conducted using ethane gas. The temperature difference as a function of pressure difference is shown in the following Figure 4.11.

When compared with self-cooling results presented using jewel orifices in Figure 4.10, the -30 V actuation provides very similar performance as the 0.015" orifice, achieving a 42 K temperature difference at 430 kPa, and the 100 V actuation provides

approximately the same performance as the 0.010” orifice, providing a 38 K difference at a 443 kPa pressure difference.

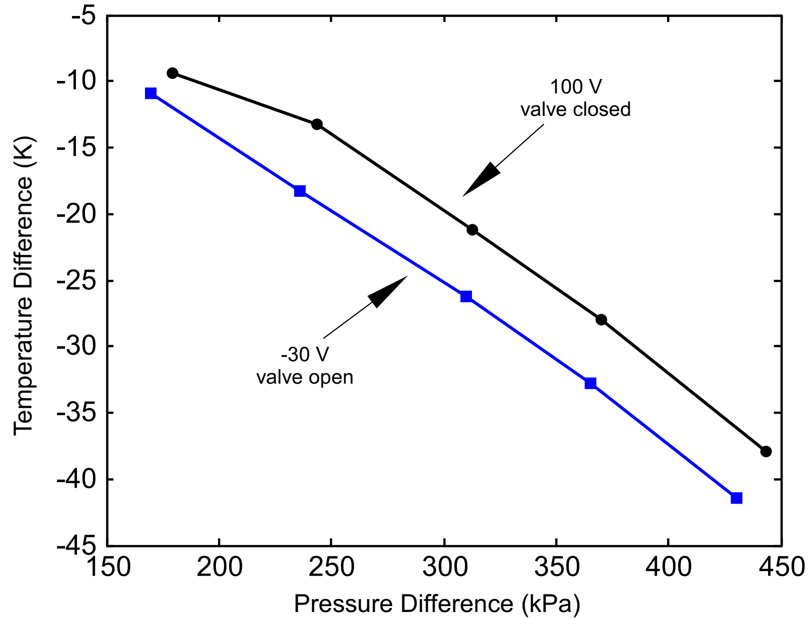

Figure 4.11: Temperature difference as a function of pressure difference while the valve is actuated at -30 V and 100 V [103].

In conclusion, the microvalve is tested as a component in a cooling system with a micromachined heat exchanger. As much as a 42 K temperature difference is achieved at a 430 kPa pressure difference using ethane gas. This test confirms that the microvalve can be used as an expansion device in the Joule-Thomson cooling system, and can provide the ability to fine tune the expansion process or vary the cooling by adjusting the actuation voltage of the valve.

CHAPTER 5

CONCLUSION AND FUTURE WORK

5.1 Summary of the Work

This research has demonstrated piezoelectrically-actuated microvalves for low temperature application. An out-of-plane PZT actuator is used to develop a microvalve that has low power consumption, but generates large force and capable of low temperature operation. A limited PZT actuator displacement is overcome by implementing perimeter augmentation to provide a sufficient flow rate. Finally, a microvalve with integrated sensors for monitoring pressure and temperature of the coolant is demonstrated.

The specific contributions of this research are listed below.

1. Demonstration of PZT actuator and piezoelectrically actuated microvalve at cryogenic temperature: Quantitative data on the PZT actuator was acquired. Experimental results revealed that PZT displacement is significantly reduced at cryogenic temperatures. However, the microvalve developed in this research, using the PZT actuator, successfully modulated gas flow down to liquid nitrogen temperature (80 K).
2. Implementation of perimeter augmentation to increase flow rate: The fundamental problem initially identified for piezoelectric actuation was a

relatively small flow area per unit of actuator displacement. The flow area is the product of the valve perimeter and actuator stoke. A simple structure design can augment the valve perimeter through the micromachining of serpentine grooves. The model simulation showed up to a five-fold increase in flow rate. Moreover, by implementing this perimeter augmentation, it is demonstrated that the microvalve is capable of achieving a high flow rate (> 1000 mL/min) even with a few microns of PZT displacement.

3. Study of valve performance over a wide range of temperatures: The developed microvalve is exposed to temperatures between 80 K and 380 K and its modulation capability is studied. The study has revealed that the valve gap spacing variation due to thermal expansion mismatch affects flow rate at given actuation voltage throughout the temperature range. The response of pressure and temperature sensors, with respect to varying temperature, is also presented.

4. Demonstration of integrated sensors on valves: Piezoresistive pressure sensor and platinum resistance temperature detector are embedded in the valve die to provide the necessary information for closed loop control of the valve. This gave added functionality to the valve in a compact manner.

5. Demonstration of liquid modulation and self-cooling: It is demonstrated that the valve is also compatible with liquid and modulation through voltage and duty cycle actuation is presented. Finally, the valve with a heat exchanger are tested together to evaluate their performance and a 42 K difference in temperature in the self-cooling test is achieved.

5.2 Recommendations for Future Work

Much work remains to be done with respect to many topics explored in this research. The design of the microvalve can be improved in numerous ways. One of the intentions of the microvalve design is to provide a large range of flow modulation with a relatively limited stroke. Although experimental data showed the existing prototype successfully modulates flow, it is likely that significant improvement in the valve performance can be achieved through optimization of land and groove width, depth, spacing, and adjustment of inlet and outlet holes. The already-developed flow model using EES software will be helpful in achieving this task.

As the valve is expected to be exposed to a wide range of temperatures, a careful consideration in material selection of the valve structure is vital. The Macor housing is chosen for this particular purpose but as shown in Chapter 2, the thermal expansion mismatch between the Macor and the PZT actuator caused a significant difference in flow rate from 80 K to 380 K. In addition, as discussed in Chapter 3, the thermal mismatch between Si and glass also imposed unwanted stress on the valve membrane. It is important to note that the coefficient of thermal expansion is not a constant but a function of temperature, and would be difficult to match the CTE of two different materials over a wide range of temperatures. This difference in thermal mismatch introduces many undesirable and unknown variables, such as stress on the housing or micromachined die or the gap spacing between valve seats. The best way to resolve this problem is to reduce the number of materials employed by using the same material whenever possible. In our case, the glass wafer can be replaced by a silicon wafer. Silicon to silicon bonding is often trickier than silicon to glass anodic bonding; however,

bonding can be accomplished through eutectic, glass frit, or fusion methods. If silicon is used in place of a glass wafer, there is also added advantage in fabrication. A DRIE step can easily form high aspect ratio inlet and outlet holes with good repeatability, eliminating ECDM, which is a serial process, or HF wet etch process, which results in significant undercut.

The housing material can also be a bulk PZT instead of a Macor ceramic to match the actuator material. Then the gap between valve seats will remain constant for a wide range of temperatures for a given actuation voltage. One can search for a more suitable structure material than Macor by measuring the thermal expansion of various materials.

The stiffer valve membrane demonstrated in Chapter 3 resulted in smaller actuator displacement due to applied force during assembly. A more compliant membrane is desirable and this can be achieved by fabricating a corrugated membrane or by varying the membrane geometry (thickness, diameter, etc).

The performance of the pressure sensor was characterized and presented here down to around 200 K but needs to be tested and verified to lower temperatures. The piezoresistive pressure sensor is expected to degrade in performance below a certain temperature due to carrier freeze-out. Antimony doped piezoresistors are expected to freeze-out at lower temperatures than boron doped piezoresistors and the mask sets are designed to accommodate the use of either boron or antimony doped piezoresistors. However, due to time and resource constraints, the antimony option has not been explored. More research concerning this topic will be helpful in the design of a piezoresistive pressure sensor for low-temperature application.

As the valve is designed for a space application, reliability is of great importance. A long term test for reliability and a study of its failure mode should be followed. So far, we have observed a couple cases of solder connection breaking lose leading to an electrical open. Developing a more reliable electrical contact is advised. In addition, observations showed, sometimes the epoxy joint would come apart and develop a leak. Thorough cleaning of the bond surfaces with proper preparation of the epoxy mixture is recommended. One may look to sandblasting the surface to increase epoxy adhesion.

On a larger scope, demonstration of an array of working valves in a distributed cooling network to meet the cooling requirements of NASA's next generation spacecraft is desirable. A working cooling component composed of a single valve with a heat exchanger is demonstrated in Chapter 4. However, realization of the distributed cooling network will involve development of many components other than the valve, and require significant resources and manpower.

REFERENCES

[1] M. J. Amato, D. J. Benford, H. S. Moseley, and J. Roman, "An engineering concept and enabling technologies for a Large Single Aperture Far-Infrared Observatory (SAFIR)," *SPIE-Int. Soc. Opt. Eng*, vol. 4850, pp. 1120-31, 2003.

[2] P. F. Goldsmith, "SAFIR – Single Aperture Far-Infrared Observatory," Jet Propulsion Laboratory and Goddard Space Flight Center, <http://safir.jpl.nasa.gov>

[3] D. J. Benford, M. J. Amato, J. C. Mather, S. H. Moseley, Jr., and D. T. Leisawitz, "Mission concept for the Single Aperture Far-Infrared (SAFIR) Observatory," *Astrophysics and Space Science*, vol. 294, n. 3-4, pp. 177-212, 2004.

[4] H. W. Yorke, C. G. Paine, C. M. Bradford, M. Dragovan, A. E. Nash, J. A. Dooley, and C. R. Lawrence, "Thermal design trades for SAFIR architecture concepts," SPIE-Int. Soc. Opt. Eng, 2004.

[5] L. J. Salerno and P. Kittel, "Cryogenics and human exploration of Mars," Cryogenics, vol. 39, no. 4, pp. 381-8, 1999

[6] J. Dino, "NASA – Cryogenic Fluid Management," 29 Mar. 2008. NASA Ames Research Center. <http://www.nasa.gov/centers/ames/research/technology-onepagers/cryogenic-fluid-management.html>

[7] L. J. Hastings, D. W. Plachta, L. Salerno, and P. Kittel, "An overview of NASA efforts on zero boiloff storage of cryogenic propellants," Noordwijk, Netherlands, 2001.

[8] P. Shirron, D. Wegel, M. DiPirro, and S. Sheldon, "An adiabatic demagnetization refrigerator capable of continuous cooling at 10 mK and below," *Nuclear Instruments and Methods in Physics Research A*, vol. 559, no. 2, pp. 651-3, 2006

[9] M. Prina, J. Borders, P. Bhandari, G. Morgante, D. Pearson, and C. Paine, "Low-heat input cryogenic temperature control with recuperative heat-exchanger in a Joule Thomson cryocooler," *Cryogenics*, vol. 44, no. 6-8, pp. 595-601, 2004

[10] T. Nast, J. Olson, P. Champagn, B. Evtimov, D. Frank, E. Roth, and T. Renna, "Overview of Lockheed Martin cryocoolers," *Cryogenics*, vol. 46, no. 2-3, pp. 164-8, 2006

[11] J.E. Zimmerman and D.B. Sullivan, "A milliwatt Stirling cryocooler for temperatures below 4 K," Cryogenics, vol. 19, no. 3, pp. 170-1, 1979

[12] M. M. Teymoori and E. Abbaspour-Sani, "Design and simulation of a novel electrostatic peristaltic micromachined pump for drug delivery applications," *Sensors and Actuators, A: Physical*, vol. 117, n. 2, pp. 222-9, 2004.

[13] H. Zhao, K. Stanley, Q. M. J. Wu, and E. Czyzewska, "Structure and characterization of a planar normally closed bulk-micromachined piezoelectric valve for fuel cell applications," *Sensors and Actuators, A: Physical*, vol. 120, n. 1, pp. 134-41, 2005.

[14] A. Manz, N. Graber, and H. M. Widmer, "Miniaturized total chemical analysis systems: a novel concept for chemical sensing," *Sensors and Actuators, B: Chemical*, vol. B1, n. 1-6, pp. 244-8, 1990.

[15] I. Chakraborty, W. C. Tang, D. P. Bame, and T. K. Tang, "MEMS Micro-valve for Space Application," *Sensors and Actuators*, vol. 83, pp. 188-193, 2000.

[16] X. Q. Wang and Y. C. Tai, "A normally closed in-channel micro check valve," *Thirteenth Annual International Conference on Micro Electro Mechanical Systems*, pp. 68-73, 2000.

[17] J. Xie, X. Yang, X. Q. Wang, and Y. C. Tai, "Surface micromachined leakage proof Parylene check valve," *14th IEEE International Conference on Micro Electro Mechanical Systems*, pp. 539-42, 2001.

[18] L. Smith and B. Hok, "A silicon self-aligned non-reverse valve," *TRANSDUCERS '91. 1991 International Conference on Solid-State Sensors and Actuators. Digest of Technical Papers*, pp. 1049-51, 1991.

[19] E. Meng, X. Q. Wang, H. Mak, and Y. C. Tai, "A check-valved silicone diaphragm pump," *IEEE Thirteenth Annual International Conference on Micro Electro Mechanical Systems*, pp. 62-7, 2000.

[20] R. L. Smith, R. W. Bower, and S. D. Collins, "The design and fabrication of a magnetically actuated micromachined flow valve," *Sensors and Actuators A: Physical*, vol. 24, n. 1, pp. 47-53, 1990.

[21] S. C. Terry, J. H. Jerman, and J. B. Angell, "A Gas Chromatographic Air Analyzer Fabricated on a Silicon Wafer," *IEEE Transactions on Electron Devices*, vol. ED-26, n. 12, pp. 1880-6, 1979.

[22] T. Ikehara, H. Yamagishi, and K. Ikeda, "Electromagnetically driven silicon microvalve for large-flow pneumatic controls," *Proceedings of the SPIE - The International Society for Optical Engineering*, vol. 3242, pp. 136-44, 1997.

[23] Y. Shinozawa, T. Abe, and T. Kondo, "A proportional microvalve using a bi-stable magnetic actuator," *Proceedings IEEE. The Tenth Annual International Workshop on Micro Electro Mechanical Systems. An Investigation of Micro Structures, Sensors, Actuators, Machines and Robots*, pp. 233-7, 1997.

[24] M. Hirano, K. Yanagisawa, H. Kuwano, and S. Nakano, "Microvalve with Ultra-Low Leakage," *Proceedings IEEE. The Tenth Annual International Workshop on Micro Electro Mechanical Systems. An Investigation of Micro Structures, Sensors, Actuators, Machines and Robots*, pp. 323-6, 1997.

[25] K. Yanagisawa, H. Kuwano, and A. Tago, "Electromagetically driven microvalve," *Microsystem Technologies*, vol. 2, n. 1, pp. 22-5, 1995.

[26] J. S. Bintoro, P. J. Hesketh, and Y. H. Berthelot, "CMOS compatible bistable electromagnetic microvalve on a single wafer," *Microelectronics Journal*, vol. 36, n. 7, pp. 667-72, 2005.

[27] J. Sutanto, P. J. Hesketh, and Y. H. Berthelot, "Design, microfabrication and testing of a CMOS compatible bistable electromagnetic microvalve with

latching/unlatching mechanism on a single wafer," *Journal of Micromechanics and Microengineering*, vol. 16, n. 2, pp. 266-75, 2006.

[28] D. J. Sadler, T. M. Liakopoulos, J. Cropp, C. H. Ahn, and H. T. Henderson, "Prototype microvalve using a new magnetic microactuator," *Proceedings of the SPIE - The International Society for Optical Engineering*, vol. 3515, pp. 46-52, 1998.

[29] C. Fu, Z. Rummler, and W. Schomburg, "Magnetically driven micro ball valves fabricated by multilayer adhesive film bonding," *Journal of Micromechanics and Microengineering*, vol. 13, n. 4, pp. S96-102, 2003.

[30] B. Bae, N. Kim, H. Kee, S. Kim, Y. Lee, S. Lee, and K. Park, "Feasibility test of an electromagnetically driven valve actuator for glaucoma treatment," *Journal of Microelectromechanical Systems*, vol. 11, n. 4, pp. 344-54, 2002.

[31] R. Luharuka and P.J. Hesketh, “A bistable electromagnetically actuated rotary gate microvalve,” *Journal of Micromechanics and Microengineering,* vol. 18, no. 3, p 035015-1-14, 2008

[32] T. Ohnstein, T. Fukinura, J. Ridley, and U. Bonne, "Micromachined silicon microvalve," *IEEE Micro Electro Mechanical Systems-An Investigation of Micro Structures, Sensors, Actuators, Machines*, pp. 95-8, 1990.

[33] K. Sato and M. Shikida, "An electrostatically actuated gas valve with an S-shaped film element," *Journal of Micromechanics and Microengineering*, vol. 4, n. 4, pp. 205-9, 1994.

[34] M. Shikida, K. Sato, S. Tanaka, Y. Kawamura, and Y. Fujisaki, "Electrostatically driven gas valve with high conductance," *Journal of Microelectromechanical Systems*, vol. 3, n. 2, pp. 76-80, 1994.

[35] M. A. Huff, M. S. Mettner, T. A. Lober, and M. A. Schmidt, "A pressure-balanced electrostatically-actuated microvalve," *IEEE Solid-State Sensor and Actuator Workshop*, pp. 123-7, 1990.

[36] M. A. Huff, J. R. Gilbert, and M. A. Schmidt, "Flow characteristics of a pressure-balanced microvalve," *The 7th International Conference on Solid-State Sensors and Actuators (Transducers '93)*, pp. 98-101, 1993.

[37] C. Goll, W. Bacher, B. Bustgens, D. Maas, R. Ruprecht, and W. K. Schomburg, "An electrostatically actuated polymer microvalve equipped with a movable membrane electrode," *Journal of Micromechanics and Microengineering*, vol. 7, n. 3, pp. 224-6, 1997.

[38] W.v.d. Wijngaart, H. Ask, P. Enoksson, and G. Stemme, "A high-stroke, high-pressure electrostatic actuator for valve applications," *Sensors and Actuators, A: Physical*, vol. 100, n. 2-3, pp. 264-71, 2002.

[39] P. Dubois, B. Guldimann, M. A. Gretillat, and N. F. d. Rooij, "Electrostatically actuated gas microvalve based on a Ta-Si-N membrane," *14th IEEE International Conference on Micro Electro Mechanical Systems*, pp. 535-8, 2001.

[40] P. Dubois, B. Guldimann, and N. F. d. Rooij, "High-speed electrostatic gas microvalve switching behavior," *Proceedings of the SPIE - The International Society for Optical Engineering*, vol. 4560, pp. 217-26, 2001.

[41] L. Yobas, D. M. Durand, G. G. Skebe, F. J. Lisy, and M. A. Huff, "A novel integrable microvalve for refreshable Braille display system," *Journal of Microelectromechanical Systems*, vol. 12, n. 3, pp. 252-63, 2003.

[42] L. Yobas, M. A. Huff, F. J. Lisy, and D. M. Durand, "A novel bulk micromachined electrostatic microvalve with a curved-compliant structure applicable for a pneumatic tactile display," *Journal of Microelectromechanical Systems*, vol. 10, n. 2, pp. 187-96, 2001.

[43] X. Yang, A. Holke, S. A. Jacobson, J. H. Lang, M. A. Schmidt, and S. D. Umans, "An electrostatic, on/off microvalve designed for gas fuel delivery for the MIT microengine," *Journal of Microelectromechanical Systems*, vol. 13, n. 4, pp. 660-8, 2004.

[44] J. K. Robertson and K. D. Wise, "A Low Pressure Micromachined Flow Modulator," *Sensors and Actuators A*, vol. 71, n. 1-2, pp. 98-106, 1998.

[45] J. K. Robertson and K. D. Wise, "A nested electrostatically-actuated microvalve for an integrated microflow controller," *Micro Electro Mechanical Systems. An Investigation of Micro Structures, Sensors, Actuators, Machines and Robotic Systems*, pp. 7-12, 1994.

[46] J. Collier, D. Wroblewski, and T. Bifano, “Development of a rapid-response flow-control system using MEMS microvalve arrays,” *Journal of Microelectromechanical Systems*, vol. 3, no. 6, pp. 912-22, 2004

[47] B. Bae, J. Han. R.I. Masel, M.A. Shannon, “A bidirectional electrostatic microvalve with microsecond switching performance,” *Journal of Microelectromechanical Systems*, vol.16, no. 6, pp. 1461-71, 2007

[48] S. Shoji, B. Schoot, N. Rooij, and M. Esashi, "Smallest Dead Volume Microvalves for Integrated Chemical Analyzing Systems," *Transducers '91*, pp. 1052-5, 1991.

[49] M. Esashi, S. Shoji, and A. Nakano, "Normally Closed Microvalve and Micropump Fabricated on a Silicon Wafer," *Sensors and Actuators*, vol. 20, pp. 163-9, 1989.

[50] M. Esashi, "Integrated Micro Flow Control Systems," *Sensors and Actuators, A: Physical*, vol. A21, n. 1-3, pp. 161-7, 1990.

[51] D. C. Roberts, L. Hanqing, J. L. Steyn, O. Yaglioglu, S. M. Spearing, M. A. Schmidt, and N. W. Hagood, "A piezoelectric microvalve for compact high-frequency, high-differential pressure hydraulic micropumping systems," *Journal of Microelectromechanical Systems*, vol. 12, n. 1, pp. 81-92, 2003.

[52] H. Q. Li, D. C. R. J. L. Steyn, K. T. Turner, O. Yaglioglu, N. W. Hagood, S. M. Spearing, and M. A. Schmidt, "Fabrication of a high frequency piezoelectric microvalve," *Sensors and Actuators, A: Physical*, vol. A111, n. 1, pp. 51-6, 2004.

[53] T. Rogge, Z. Rummler, and W. K. Schomburg, "Polymer micro valve with a hydraulic piezo-drive fabricated by the AMANDA process," *Sensors and Actuators, A: Physical*, vol. A110, n. 1-3, pp. 206-12, 2004.

[54] P. Shao, Z. Rummler, and W. K. Schomburg, "Polymer micro piezo valve with a small dead volume," *Journal of Micromechanics and Microengineering*, vol. 14, n. 12, pp. 305-9, 2004.

[55] C. Lee and E. H. Yang, "A Piezoelectric Liquid-Compatible Microvalve for Integrated Micropropulsion," in *Technical Digest of the 2004 Solid-State Sensor and Actuator Workshop*. Hilton Head Isl., SC, 2004, pp. 160-3.

[56] E. H. Yang, C. Lee, J. Mueller, and T. George, "Leak-tight piezoelectric microvalve for high-pressure gas micropropulsion," *Journal of Microelectromechanical Systems*, vol. 13, n. 5, pp. 799-807, 2004.

[57] C. Lee, E. H. Yang, S. M. Saeidi, and J. M. Khodadadi, "Fabrication, characterization, and computational modeling of a piezoelectrically actuated microvalve for liquid flow control," *Journal of Microelectromechanical Systems*, vol. 15, n. 3, pp. 686-96, 2006.

[58] T. Watanabe and H. Kuwano, "A microvalve matrix using piezoelectric actuators," *Microsystem Technologies*, vol. 3, n. 3, pp. 107-11, 1997.

[59] H. Jerman, "Electrically activated normally closed diaphragm valves," *Journal of Micromechanics and Microengineering*, vol. 4, n. 4, pp. 210-16, 1994.

[60] P. W. Barth, C. C. Beatty, L. A. Field, J. W. Baker, and G. B. Gordon, "A robust normally-closed silicon microvalve," *Solid-State Sensor and Actuator Workshop*, pp. 248-50, 1994.

[61] S. Messner, M. Muller, V. Burger, J. Schaible, H. Sandmaier, and R. Zengerle, "A normally-closed, bimetallically actuated 3-way microvalve for pneumatic applications," *Eleventh Annual International Workshop on Micro Electro Mechanical Systems. An Investigation of Micro Structures, Sensors, Actuators, Machines and Systems*, pp. 40-4, 1998.

[62] M. Kohl, D. Dittmann, E. Quandt, and B. Winzek, "Thin film shape memory microvalves with adjustable operation temperature," *Sensors and Actuators, A: Physical*, vol. A83, n. 1-3, pp. 214-19, 2000.

[63] M. Kohl, D. Dittmann, E. Quandt, B. Winzek, S. Miyazaki, and D. M. Allen, "Shape memory microvalves based on thin films or rolled sheets," *Materials Science & Engineering A (Structural Materials: Properties, Microstructure and Processing)*, vol. A273-275, pp. 784-8, 1999.

[64] M. Kohl, K. D. Skrobanek, and S. Miyazaki, "Development of stress-optimised shape memory microvalves," *Sensors and Actuators, A: Physical*, vol. A72, n. 3, pp. 243-50, 1999.

[65] K. D. Skrobanek, M. Kohl, and S. Miyazaki, "Stress-optimized shape memory microvalves," *Proceedings of the IEEE Micro Electro Mechanical Systems (MEMS)*, pp. 256-61, 1997.

[66] M. J. Zdeblick and J. B. Angell, "A microminiature electric-to-fluidic valve," *The 4th International Conference on Solid-State Sensors and Actuators (Transducers '87)*, pp. 437-39, 1987.

[67] H. Takao, K. Miyamura, H. Ebi, M. Ashiki, K. Sawada, and M. Ishida, "A MEMS microvalve with PDMS diaphragm and two-chamber configuration of thermo-pneumatic actuator for integrated blood test system on silicon," vol. 119, n. 2, pp. 468-75, 2005.

[68] C. A. Rich and K. D. Wise, "A high-flow thermopneumatic microvalve with improved efficiency and integrated state sensing," *Journal of Microelectromechanical Systems*, vol. 12, n. 2, pp. 201-8, 2003.

[69] J. A. Potkay and K. D. Wise, "An electrostatically latching thermopneumatic microvalve with closed-loop position sensing," *18th IEEE International Conference on Micro Electro Mechanical Systems*, pp. 415-18, 2005.

[70] N. Maluf, *An Introduction to Microelectromechanical Systems Engineering*: Artech House, Inc., 2000.

[71] H. Jaffe and D. A. Berlincourt, "Piezoelectric Transducer Materials," *Proceedings of the IEEE*, vol. 53, n. 10, pp. 1372-86, 1965.

[72] R. P. Taylor, G. F. Nellis, S. A. Klein, D. W. Hoch, J. Feller, P. Roach, J. M. Park, and Y. Gianchandani, "Measurements of the Material Properties of a Laminated Piezoelectric Stack at Cryogenic Temperatures," *Conference Proceedings of the 2005 International Cryogenic Materials Conference*, vol. 824, pp. 200-7, 2006.

[73] R. Gerson, "Piezoelectric and dielectric properties of lead titanate zirconate ceramics at low temperatures," *Journal of Applied Physics*, vol. 33, no. 3, p 830-2, 1962

[74] Hooker, M.W., "Properties of PZT-Based Piezoelectric Ceramics Between -150 and 250˚C", *Lockheed Martin Engineering & Sciences Company*, NASA Center for Aerospace Information, NASA/CR-1998-208708, 1998.

[75] T. R. Brosten, "Model and Test of an Actively Controlled Cryogenic Micro Valve," University of Wisconsin - Madison, 2006

[76] E.B. Arkilic, M.A. Schmidt, and K.S. Breuer, "Gaseous slip flow in long microchannels," *Journal of Microelectromechanical Systems*, vol.6, no.2, pp.167-78, 1997

[77] S.A. Klein, "Engineering Equation Solver," The University of Wisconsin - Madison, 2002, http://sel.me.wisc.edu/ees/new_ees.html

[78] B.A.M. Andersen, O. Hansen, and M. Kristensen, "Spatial Variation of the Etch Rate for Deep Etching of Silicon by Reactive Ion Etching," *Journal of Vacuum Science & Technology B (Microelectronics and Nanometer Structures)*, vol. 15, no. 4, pp. 993-9, 1997

[79] H.K. Taylor, H. Sun, T.F. Hill, A. Farahanchi, and D.S. Boning, "Characterizing and Predicting Spatial Nonuniformity in the Deep Reactive Ion Etching of Silicon," *Journal of the Electrochemical Society*, vol. 153, no. 8, pp. C575-85, 2006

[80] V. Fascio, R. Wuthrich, D. Viquerat, and H. Langen, "3D Microstructuring of Glass Using Electrochemical Discharge Machining (ECDM)," *International Symposium on Micromechatronics and Human Science*, Nagoya, Japan, Nov. '99, pp.179-83

[81] J. Frnz, H. Baumann, and H.-P. Trah, "A Silicon Microvalve with Integrated Flow Sensor," *8th International Conference on Solid-State Sensors and Actuators (TRANSDUCERS '95)*, Stockholm, Sweden, June 1995, vol.2, pp.313-16

[82] M.E. Piccini and C.B. Towe, "A Shape Memory Alloy Microvalve with Flow Sensing," *Sensors and Actuators, A: Physical*, vol.128, no.2, pp.344-49, 2006

[83] S.K. Clark and K.D. Wise, "Pressure Sensitivity in Anisotropically Etched Thin-Diaphragm Pressure Sensors," *IEEE Transaction on Electron Devices*, vol.ED-26, no.12, pp.1887-96, 1979

[84] S.T. Cho, K. Najafi, and K.D. Wise, "Internal Stress Compensation and Scaling in Ultrasensitive Silicon Pressure Sensors," *IEEE Transaction on Electron Devices*, vol.39, no.4, pp.836-42, 1992

[85] C.J. Yeager, "A Review of Cryogenic Thermometry and Common Temperature Sensors," *IEEE Sensors Journal*, vol.1, no.4, pp.352-60, 2001

[86] S.S. Courts, P.R. Swinehart, and C.J. Yeager, "A new cryogenic diode thermometer," *AIP Conference Proceedings*, no. 613B, pp. 1620-7, 2002

[87] S.-C. Kim and K.D. Wise, "Temperature Sensitivity in Silicon Piezoresistive Pressure Transducers," *IEEE Transactions on Electron Devices*, vol.ED-30, no.7, pp.802-10, 1983

[88] Y. Kanda, "Graphical Represenstation of the Piezoresistance Coefficients in Silicon," *IEEE Transactions on Electron Devices*, vol.ED-29, no.1, pp.64-70, 1982

[89] U. Aljancic, D. Resnik, D. Vrtacnik, M. Mozek, and S. Amon, "Temperature Effects Modeling in Silicon Piezoresistive Pressure Sensor," *IEEE Mediterranean Electrotechnical Conference*, Cairo, Egypt, May 2002, pp. 36-40

[90] G. Kowalski, "Miniature Pressure Sensors and Their Temperature Compensation," *Sensors and Actuators*, vol.11, no.4, pp.367-76, 1987

[91] P. Kopsytynski and E. Obermeier, "An Interchangeable Silicon Pressure Sensor with On-Chip Compensation Circuitry," *Sensors and Actuators*, vol.18, no.3-4, pp.239-45, 1989

[92] J. Bryzek, R. Mayer, and P. Barth, "New Generation of Disposable Blood Pressure Sensors with Digital On-Chip Laser Trimming," *IEEE Solid State Sensor and Actuator Workshop*, Hilton Head Island, SC, June 1988, pp.121-122

[93] T. Ishigara, K. Suzuki, S. Suwazono, M. Hirata, and H. Tanigawa, "CMOS Integrated Silicon Pressure Sensor," *IEEE Journal of Solid-State Circuits*, vol.SC-22, no.2, pp.151-6, 1987

[94] S. Fricke, A. Friedberger, G. Mueller, H. Seidel, and U. Schmid, "Strain Gauge Factor and TCR of sputter deposited Pt thin films up to 850ºC," *IEEE Sensors Conference*, Lecce, Italy, 2008, pp.1532-1535

[95] W.H. Ko, J.T. Suminto, and G..J. Yeh, "Bonding Techniques for Microsensors," *Micromachining and Micropackaging of Transducers*, vol.20, pp. 41-61, 1985

[96] A.P. Zhernov, "Lattice Constant and Coefficient of Linear Thermal Expansion of the Silicon Crystal. Influence of Isotopic Composition," *Low Temperature Physics*, vol.26, no.12, pp.908-15, 2000

[97] R.M. Buffington and W.M. Latimer, "Coefficients of Expansion at Low Temperatures and Thermodynamic Applications of Expansion Data," *Journal of the American Chemical Society*, vol.48, pp.2305-19, 1926

[98] R.K. Kirby, "Platinum – A Thermal Expansion Reference Material," International *Journal of Thermophysics*, vol.12, no.4, pp.679-685, 1991

[99] A.T. Evans, J.M. Park, G.F. Nellis, S.A. Klein, J.R. Feller, L. Salerno, Y.B. Gianchandani, "A Low Power, Micro Valve-Regulated Drug Delivery System Using a Si Micro-Spring Pressurized Balloon Reservoir," *14th International Conference on Solid-State Sensors, Actuators and Microsystems (TRANDUCERS '07)*, Tucson, AZ, 2007, pp.359-62

[100] A.T. Evans, J.M. Park, S. Chiravuri, Y.B. Gianchandani, "Dual Drug Delivery Device for Chronic Pain Management Using Micromachined Elastic Metal Structures and Silicon Microvalves," *21st IEEE International Conference on MicroElectro Mechanical Systems (MEMS '08)*, 2008, pp.252-5

[101] W. Zhu, M. J. White, D. W. Hoch, G. F. Nellis, S. A. Klein, and Y. B. Gianchandani, "Two approaches to micromachining Si heat exchanger for Joule-Thomson cryosurgical probes," *20th IEEE International Conference on Micro Electro Mechanical Systems*, pp. 317-20, 2007.

[102] W. Zhu, M. J. White, G. F. Nellis, S. A. Klein, and Y. B. Gianchandani, "A perforated plate stacked Si/glass heat exchanger with in-situ temperature sensing for Joule-Thomson coolers," *21th IEEE International Conference on Micro Electro Mechanical Systems*, pp. 844-7, 2008.

[103] W. Zhu, "Lithographically Micromachined Si/Glass Heat Exchangers for Joule-Thomson Cryocoolers," Ph.D. Dissertation – University of Michigan, 2008 (in preparation)